IN THE NAME OF ALLAH

THE MOST MERCIFUL AND THE MOST COMPASSIONATE

Numerical Modelling in some Non-linear Flow problems

By

Muhammad Awais

Department of Mathematics
Quaid-I-Azam University
Islamabad, Pakistan
2021

Numerical Modelling in some Non-linear Flow problems

By

Muhammad Awais

Supervised By

Prof. Dr. Muhammad Yousaf Malik

Department of Mathematics
Quaid-I-Azam University
Islamabad, Pakistan
2021

Numerical Modelling in some Non-linear Flow problems

By

Muhammad Awais

A THESIS SUBMITTED IN THE PARTIAL FULFILLMENT OF THE
REQUIREMENT FOR THE DEGREE OF
DOCTOR OF PHILOSOPHY
IN
MATHEMATICS

Supervised By

Prof. Dr. Muhammad Yousaf Malik

Department of Mathematics
Quaid-I-Azam University
Islamabad, Pakistan
2021

Author's Declaration

I **Mr. Muhammad Awais** hereby state that my PhD thesis entitled **"Numerical Modelling in some Non-linear Flow Problems"** is my own work and has not been submitted previously by me for tacking any degree from this University **(Quaid-I-Azam University)** or anywhere else in the country/world.

At any time if any statement is found to be incorrect even after completion, the university has right to withdraw my PhD degree.

Name of Student: Muhammad Awais

Date: 21/06/2021

Plagiarism Undertaking

I solemnly declare that research work presented in thesis entitled "Numerical Modelling in some Non-linear Flow Problems" is solely my research work with no significant contribution from any other person. Small contribution/help wherever taken has been duly acknowledge and that complete thesis has been written by me.

I understand the zero tolerance policy of the HEC and Quaid-I-Azam University, Islamabad towards plagiarism. Therefor I as an author of the above titled thesis declare that no portion of my thesis has been plagiarized and any material used as reference is properly referred/cited.

I undertake that if I am found guilty of any formal plagiarism in the above titled thesis even afterward of PhD degree, the University reserved the rights to withdraw/revoke my PhD degree and that HEC and University has the right to publish my name on the HEC/university website on which names of student are placed who submitted plagiarized thesis.

Name: Muhammad Awais

Author Signature:

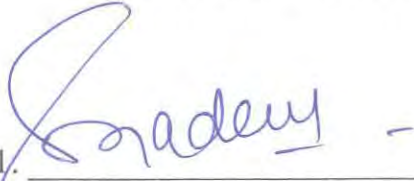# Numerical Modelling in some Non-linear Flow Problems

By

Muhammad Awais

CERTIFICATE

A DISSERTATION SUBMITTED IN THE PARTIAL FULFILLMENT OF THE REQUIREMENTS FOR THE DEGREE OF THE DOCTOR OF

PHILOSOPHY

We accept this dissertation as conforming to the required standard

1. _____

Prof. Dr. Sohail Nadeem
(Chairman)

2. _____

Prof. Dr. Muhammad Yousaf Malik
(Supervisor)

3. _____

Dr. Muhammad Mushtaq

Department of Mathematics COMSATS University, Park Road Chak Shahzad, Islamabad.

4. _____

Dr. Iffat Zehra

Department of Mathematics, Air University Islamabad.

Department of Mathematics
Quaid-I-Azam University
Islamabad, Pakistan
2021

Certificate of Approval

This is to certify that the research work presented in this thesis entitled **Numerical Modelling in some Non-linear Flow Problems** was conducted by **Ms. Muhammad Awais** under the kind supervision of **Prof. Dr. Muhammad Yousaf Malik**. No part of this thesis has been submitted anywhere else for any other degree. This thesis is submitted to the Department of Mathematics, Quaid-i-Azam University, Islamabad in partial fulfillment of the requirements for the degree of Doctor of Philosophy in field of Mathematics from Department of Mathematics, Quaid-i-Azam University Islamabad, Pakistan.

Student Name: **Muhammad Awais**   Signature:

External committee:

a) **External Examiner 1**:   Signature:
   Name: **Dr. Muhammad Mushtaq**
   Designation: Assistant Professor
   Office Address: Department of Mathematics COMSATS University, Park Road Chak Shahzad, Islamabad.

b) **External Examiner 2**:   Signature:
   Name: **Dr. Iffat Zehra**
   Designation: Assistant Professor
   Office Address: Department of Mathematics, Air University Islamabad.

c) **Internal Examiner**   Signature:
   Name: **Dr. Muhammad Yousaf Malik**
   Designation: Professor
   Office Address: Department of Mathematics, QAU Islamabad.
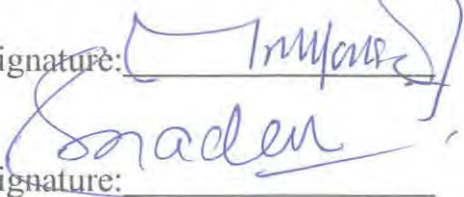
Supervisor Name: Signature:
Prof. Dr. Muhammad Yousaf Malik

Name of Dean/ HOD   Signature:

Prof. Dr. Sohail Nadeem

Dedicated to

Hazrat <u>MUHAMMAD</u> (PBUH)

and His Beloved Family

for sake of them **Earth** and the **Heavens**
were created

To my "Hazrat G Molana Qasim
Mansoor (D.B) "

And my Beautiful

"Wife"

Acknowledgment

In the name of Allah, the most Gracious and the most merciful

Alhamdulillah, all praises to **Allah** for the strengths and His blessing in completing this thesis. I reward and appreciate Him, consult Him for His aid and Forgiveness. After Almighty **Allah Subhanhu Wa Ta'ala**, I say thanks to the **Hazrat Muhammad ﷺ**, the last messenger of **Allah Subhanhu Wa Ta'ala** who has guided me from the darkness to the brightness, and from stupidity to the cleverness. who emphasized the importance of knowledge by saying "**learn the knowledge form cradle to grave**". The prophet **Muhammad ﷺ** commanded knowledge upon all Muslims and urged them to seek knowledge as far they could reach, and to seek it all times.

Foremost, special prayers for my beloved **Father** (**Abdul Salam**), may Allah's mercy upon him(ameen). Although I didn't see him, but I want to carry on in my father's footsteps. I want to tell him that "missing you is my hobby, and you are always with us in our hearts.

There aren't enough words to express my gratitude to you (**Mother**). I know I don't express my gratitude enough, but I truly am. You've taught me a lot. And it was because of your affection that I realized how much you mean to me.

Although there is no official Brother's Day, you can tell your brother (**Tahoor-ul-Isalm**) how much he means to you at any time. Even though we don't talk much, don't hang out together, and don't spend a lot of time together. But I know that whenever I yell, my brother will always be there for me.

I am by using this chance to convey my appreciation to **My wife**, and I just want to say thank you for being the most beautiful person, inside and out. Thank you for making the world a better place, just by being in it. Thank you for making colors a little brighter and sunshine a little warmer. Thank you for the laughs, for the cries, and for everything in between. I do not have words to tell how much you are special to me. Thank you for giving me these reasons and a million more, to be thankful for.

I say thanks from core of my heart to my kind supervisor **Prof. Muhammad Yousaf Malik**. His expert gaudiness, constructive criticism and continuous encouragement helped me in all time during my research and writing this thesis. I am grateful to Chairman of mathematics department,

Prof. Dr. Sohail Nadeem and all faculty members for providing facilities and proper atmosphere to complete this thesis.

I would not imagine complete my acknowledgement without saying thanks to my colleagues and friend. I have no words to express my emotions and respect to my dearest friends and colleague **Dr. Arif Hussain, Dr. Khalil-Ur-Rehman, Dr. Mair Khan, Dr. Sardar Bilal, Dr. Imad Khan, Dr. Arif Ullah Khan** and last but not the least **Dr. Usman**, for their friendship, continuous encouragement, and love during this thesis. I am very please to acknowledge my senior and mentor **Dr. Taimoor Salahuddin** for his help during my research work. I would also say thanks to my precious and loving childhood friends **Mr. Zubair, Mr. Mansoor, Mr. Ismail, and Maj. Waheeda Khattak**.

Finally, I would like to thank the personalities without whom my life is incomplete and colorless, my **Sisters**, **Brothers-in-law**, **Bhabi and Nieces.** I could not achieve my life goal without their support, love, and prayers. Especially thanks to **Bashir Ullah Bhai** and my younger **Sister,** who encourage me at every moment when I was struggling. I found myself is the luckiest person on the planet having such loving and caring family.

Muhammad Awais

Preface

Academic curiosity and latest technology application has generated considerable interest in researchers towards non-Newtonian rheological problems. In recent years, numerous examinations have been reported on non-Newtonian fluids due to their generous and treasured utility in industrial mechanism, power engineering, petroleum production and in broad spectrum chemical processes. Nanofluids are modern type of fluids, which are combination of base fluid and nano-sized metal particles. The basic principle of including these particles is to efficiently manage the heat transfer process and reduce to drag them. Because it is observed that mostly fluids (water, oil, ethylene glycol, engine oil etc.) which are traditionally utilized in thermal processes having low thermal conductivity. Recently, nanofluids are found very useful in bio-medicine and bio-engineering. Thus due to substantial importance, this phenomenon has motivated to explore these important features of fluid flows in current work. Since Sisko fluid, Prandlt and Prandlt_Eyring fluid models have great importance in industry. However, the models of such type that involve stretching in cylinder/sheet has not been discussed so far. Thus, major focus of present work is on these models. Numerical solutions are obtained through robust numerical technique i.e. Shooting method. This thesis comprises on seven chapters. The layout of this thesis is as follows:

Literature review of present work is presented in chapter 0.

Boundary layer flow of MHD Sisko fluid model over a stretching cylinder, under the effect of viscous dissipation is investigated in chapter 1. The cylindrical polar coordinates are used to model this physical problem. The modeling yields a nonlinear set of partial differential equations. Modelled equations are transferred to non-dimensional form after application of appropriate similarity transformations. The obtained equations are solved numerically with the aid of shooting technique in conjunction with Runge-Kutta fifth order scheme. The expressions for velocity and temperature are computed under different conditions and deliberated in graphical manner. The local Nusselt number and wall friction coefficient are calculated and described in quantitative sense through graphs and tables. The contents of this chapter are published in **AIP Advances 6, 035009 (2016), Doi:10.1063/1.4944347**

The physical aspects of mixed convection, axisymmetric stagnation point and Joule heating on boundary layer flow of MHD Sisko fluid towards a stretching cylinder are analysed in chapter 2. The modelled partial differential equations are transfigured into ordinary differential equations with the aid of scaling group of transformations. Computed numerical solutions depicts impact of flow controlling parameters on velocity, temperature, coefficient of wall friction and wall heat flux is delineated via graphical and tabular manners. A comparison is made to ensure the validity of computed results. The contents of this chapter are published in **Results in Physics 7(2017) 49-56.**

Chapter 3 focuses on including work presented in chapter 2 by factoring nonlinear-thermal radiation, heat generation/absorption, variable thermal conductivity and convective boundary conditions effects into account. Here, silent features of mixed convection and non-linear thermal radiation for non-Newtonian Sisko fluid over a linearly stretching inclined cylindrical surface are anticipated. The effect of pertinent flow parameters on these quantities are displayed with the help of graphs. Physical phenomenon in vicinity of stretching surface are explained with the help of skin friction coefficient and local Nusselt number. Also, effect of physical parameters are depicted with the assistance of graphs and tables. The comparison of present and previous results exhibits good agreement which leads to validate the presented model. The contents of this chapter are published in **European Physical Journal Plus 132(9) (2017), DOI:10.1140/epjp/i2017-11645-y.**

Computational study has been established to explore the combined physical aspects of melting heat transfer and chemical reaction on electrically conducting Prandtl fluid flow towards an inclined stretching cylinder in chapter 4. The effect of relevant physical parameters on velocity, temperature and concentration profiles are taken into account. The contents are accepted in **Canadian Journal of Physics (cjp-2018-0582.R1).**

Chapter 5 focuses on MHD boundary layer flow of Prandtl nanofluid over a linearly stretching cylinder. The effect of chemical reaction is also accounted in this case. The governing boundary layer equations regarding the flow are converted into a system of ordinary differential equations after using similarity transformation, which has been solved numerically by applying shooting method. The contents of this chapter are published in **Journal Mathematical Problems in Engineering**. **doi.org/10.1155/2021/5162423**

Chapter 6 spotlight the effect of Navier slip and convective boundary conditions on MHD Prandtl-Eyring nanofluid over stretching sheet under the influence of chemical reaction. The modelled problem comprises highly nonlinear partial differential equations under prescribed boundary conditions. To facilitate the computation process, an appropriate group of similar variables is utilized to transfigured governing flow equations into dimensionless form. Numerical results obtained through shooting technique are accomplished. The interesting aspects of velocity, temperature and concentration profiles are visualized via graphs by varying values of physical parameters. The contents of this chapter are published in **Mathematical Methods in the Applied Sciences (2018) Doi.org/10.1002/mma.5319.**

Contents

List Of Figures

List of Tables

Nomenclature

x, r	Space variable
u, v	velocity component in x and $r(y)$ direction
ρ	density of fluid
μ	dynamic viscosity
v	kinematics viscosity
k	Thermal conductivity of fluid
σ	Electric conductivity
U_w	stretching velocity
λ	Mixed convection parameter
γ	Curvature parameter
$\dfrac{d}{dt}$	Material time derivative
B_i	Biot number
J	Current density
Ec	Eckert number
T	Fluid temperature
h_w	Coefficient of heat transfer
T_w	Wall temperature
T_∞	Ambient temperature of fluid
T_m	Melting temperature
C	Fluid concentration
λ_L	Latent heat of the fluid
C_w	Wall concentration
C_∞	Ambient concentration
S	Stress tensor of Prandtl fluid
C_p	Specific heat at constant pressure
I	Identity matrix
p	Pressure

A_1	First Rivlin-Eiricksen Tensor
$T_\circ$	Cauchy stress tensor
τ	Ratio of the nanoparticles heat capacity to the base fluid heat capacity
D_B	Brownian diffusion coefficient
D_T	Thermophoretic diffusion coefficient
A	Sisko Fluid parameter
a, b	Concentration of chemical species of a and b
ε	Variable thermal conductivity
δ_H	Heat source/sink parameter
θ_t	Temperature ratio parameter
R_d	Thermal radiation parameter
ψ	Stream function
g	Gravity
η	Similarity variable
B_c	Solutal expansions coefficient
B_T	Thermal expansion coefficient
β_c	Concentration expansion coefficient
$k_\circ$	Chemical reaction coefficient
kr	Chemical reaction parameter
M	Magnetic field parameter
Ψ	Stream function
b	Dimensionless constant
n	Velocity power index
$\dot{\alpha}$	Thermal diffusivity
σ^*	Stefan-Boltzmann constant
k_1	Absorption coefficient
H_1, H_2, H_3	Unknown initial conditions
M_L	Dimensionless melting parameter
c_s	Heat capacity of solid surface

C_w	Volumetric fraction of nano fluid
j_w	Wall mass flux
Le	Lewis number
λ_s	Velocity slip parameter
b	Power-law viscosity
n	Flow behavior index
Q_o	Heat source/sink coefficient
q_r	Nonlinear radiative heat flux
R	Thermal radiation parameter
Ec	Eckert number
Nt	Thermophoresis parameter
Nb	Brownian motion parameter
$\Pr$	Prandtl number
Le	Lewis number
Gr	Local thermal Grashof number
Gc	Local solutal Grashof number
τ_w	Wall stress
q_w	Wall flux heat
q_m	Mass flux
Re_x	Local Reynolds number
C_f	Skin friction coefficient
Nu_x	Nusselt number
Sh_x	Sherwood number

Chapter 0

Introduction

In recent of world substantial number of complex fluids are under examination and have totally dissimilar attributes than viscous fluids. However, they are very useful in daily life and industry, for example, suspensions, emulsions, pharmaceutics, geographical streams, personal care products, ink-jet printing, toothpaste, paints, oil, lubricating greases, polymer handling, honey, biological fluids etc. These are called non-Newtonian fluids. For example, for a common person blood flow in our arteries and veins is a prime example of such fluids. Because of their importance in daily life, many studies have been reported to explore the characteristics of non-Newtonian fluids in last few years. It is verified through experiments that; flow properties of these fluids have lots of variations. Consequently, various fluid models are recommended to explore their flow properties, such as, Cross model, Ellis Model, Sutterby model, tangent hyperbolic, and Williamson fluid model etc. For the analysis of steady fluids flow, Sisko fluid model is rated very helpful. This fluid model is good for portraying shear thinning and shear thickening behaviour. Many fluids found in nature obey this model especially the flow of greases, waterborne coatings, and metallic car basecoat, greasing up oils are some of its modern applications. Sisko [1] the founder of this model investigated the lubricating greases. Nadeem et al. [2] analyzed the biofluid flow in a uniform inclined tube with the help of Sisko fluid model and found the analytical expressions of interested quantities with HAM. They discussed the peristaltic flow of both viscous and non-Newtonian fluids. Nadeem et al. [3] also analyzed the biofluid flow of a Sisko fluid in an endoscope and found both analytical as well as

computational solution of the governing D.Es. The biofluid flow of the Sisko in an asymmetric channel and in the presence of nanoparticle was investigated by Akber [4]. She found numerical solution of governing equations by shooting method. She established that the Sisko parameter increases the pressure in the region of peristaltic pumping, whereas pressure decreases in the augmented pumping region. Khan et al. [5] described the MHD flow of Sisko fluid in annular pipe and determined that velocity profile of the Sisko fluid is far less than viscous fluid. Malik et al. [6] explored the flow of Sisko fluid with convective heat transfer. They calculated analytical as well as numerical solution of the problem. Malik et al. [7] discussed also the hydromagnetic flow of Sisko fluid past a stretching cylinder and solved the flow equations by shooting method. They found that the Sisko parameter enhances velocity profile and boundary layer thickness. Moallemi et al. [8] investigated the thermo-flow of Sisko fluid over a pipe and find the solution with HPM. Munir et al. [9] characterized the properties of time independent flow of Sisko fluid with buoyancy assisting and opposing effect over an isothermal surface. They perceived that with an increase in material parameter of Sisko fluid, skin friction coefficient increases. The non-Newtonian Sisko fluid was also analyzed by Ref. [10-11]. Fluid models exhibit a range of rheological complexities including time-dependent, time-independent, viscoelasticity, pseudo plasticity and viscoinelasticity behaviour. Among these family of non-Newtonian, the fluids paramount subclass which possesses only viscous properties is known as viscoinelastic fluids. Dunn [12], initially investigated the properties of viscoinelastic fluids and developed an experimental relationship among shear and stress rate. Nadeem et al. [13] applied the regular perturbation technique to analyzed the peristalsis motion of Prandtl fluid. They concluded that both pressures rise, and frictional

forces have opposite influences for different increasing values of Prandtl fluid parameters. Akbar [14] offered approximate solution of Prandtl fluid flow in tapered arteries. She used homotopy perturbation technique to analyze the results of governing differential equations. Her findings tell that Prandtl fluid parameters have great influence on stenosis shape and its height, i.e., appreciable amount of reduction is observed for both stenosis shape and height towards positive values of Prandtl fluid parameters. Jothi et al. [15] examined the magnetenohydrodynamic flow of visco-inelastic fluid in a uniform channel. They emphasize on both low Reynolds number and long wavelength approximation and reconfirmed the suppress attitude of Prandtl fluid parameter towards axial velocity and pressure gradient with the aid of homotopy perturbation technique.

Nanofluid is a recently developed fluid which comprises a base fluid along with nanoparticles of metals. The major concern of suspending nanoparticles into base fluid is to enlarge the capability of heat conductance, because traditionally utilized fluids for heat transfer has less ability of heat conductance. Before the invention of nanofluid, lot of experiments were performed i.e., metallic particles of milli or micro size are inserted, but the desired results were not achieved. Then Choi [16-17] performed the successful experiment by adding nanoparticles in base fluid and surprisingly found that the nanofluids have multi-times large capability of heat then their corresponding base fluids. This is considered one of the significant advancements of present-day research which drives the next major industrial revolution of this century. Over the last two decades, the nanofluid flow analysis experiences great enlargement and subject of differentiation due to extensive uses in almost every aspect of life e.g., nanofluids are utilized as a coolant in many processes like vehicle engines, walls of nuclear reactors, heat exchangers, superpower

computers and solid-state lighting etc. Recently, nanotechnology has great deal with biomedicine such as cancer therapy, drug delivery, detecting genomic-length DNA and HIV virus in micro channels etc. Kang et al. [18] performed experiments to estimate the thermal conductivity of nanofluids by suspending nanoparticles of Ultra-Dispersed Diamond (UDD), silver and silica. They found that the best nanofluid is 1% UDD in Ethylene glycol whose thermal conductivity enhancement was up to 70%. Yoo et al. [19] prepared the nanofluids consisting of TiO_2, Al_2O_3, Fe, and WO_3. They suggested that nanofluids produce great enlargement in thermal conductivity, but more experimental studies should be performed with advanced methods to predict thermal conductivity. Wang and Mujumdar [20] presented the comprehensive review of work done on different aspects of nanofluids. They compared the results of different proposed models and advised that it is quite difficult to estimate thermal conductivity of nanofluids theoretically. Despite their instructions, theoretical investigations are also important. Current work focuses on the Buongiorno model, in this model a continuum assumption is considered for base fluid and nanoparticles. This model was proposed by Buongiorno [21] in his valuable work, where he discussed the nano fluid under different effect and found that noticeable influences of Brownian motion and thermophoresis. As this model is simple in computational point of view, thus recently this model is consistently utilized by researchers to explore the properties of nanofluids. Khan and Pop [22] initially explored the boundary layer flow of viscous fluid over stretching sheet in the presence of nanosized particle. They found that Brownian motion and thermophoresis strongly influenced temperature of the fluid. Rana and Bhargava [23] and Mabood et al. [24] investigated the applications of Buongiorno model to delineate the thermophysical features of fluids on nonlinear stretching surfaces.

Malik et al. [25] studied the effect of MHD flow of Eyring-Powell fluid past over a stretching sheet in the presence of free and force convection. Recently, Hussain et al. [26] develop a computational algorithm of MHD flow of Sisko nanofluid past a stretching cylinder.

The investigation of mutual interaction between moving fluids and magnetic field is commonly known as magnetohydrodynamics (MHD). Alfven [27] was the first who described the class of MHD waves also known as Alfven waves. In the recent world of technology, MHD waves being encountered in all subdivisions of science, thus these are gaining the interest of researchers for qualitative analysis over them. The fundamental application of MHD fluid lies in the field of mechanical engineering, aerospace engineering, astrophysics, and geophysics etc. For instance, some devices/processes utilizing MHD phenomenon are cooling reactors, MHD accelerators, purification of crude oil, electrostatic filters, geothermal energy extraction, and fluid droplets. In fluid dynamics, MHD flow of non-Newtonian fluid was initially examined by Sarpkaya [28] and then this work was further extended by many investigators. Liao [29] acquired HAM solution for hydromagnetic non-Newtonian fluid flow past a surface which is linearly stretched. He suggested that MHD parameter amplifies the wall shear stress coefficient. He also witnessed that the magnetic field impacts are more dominant in the shear-thinning region than shear-thickening region. MHD stagnant flow with the impact of first order chemical reaction towards porous surface was discussed by Mebood et al. [30]. This problem was solved analytically by using HAM. They noted that for all values of suction/injection parameter and Hartmann number, local skin-friction coefficient increases monotonically. Malik et al. [31] configured the physical problem on a non-Newtonian fluid flow over

cylinder under MHD effect and concluded that the fluid velocity decreases by increasing MHD parameter. Akbar et al. [32] discussed the flow of non-Newtonian Eyring-Powell fluid under magnetic field effect past a stretching sheet. They utilized computational algorithm to tackle flow problem and found that Hartmann number offers resistance towards fluid movement. Hydromagnetic flow of Casson fluid model over an exponentially shrinking sheet was examined by Nadeem et al. [33]. The governing equations of this problem were solved with Adomian decomposition method. Nadeem et al. [34] numerically explored the 3D hydromagnetic flow of Casson fluid past a porous surface. They recommended that the fluid velocity decays when influence of MHD improves. Ismail et al. [35] considered the MHD steady flow of viscous fluid between two parallel plates. Abo-Eldhab and Saleem [36] discussed the flow of power law fluid model past a moving cylinder under the impact of applied magnetic field.

Mixed convection (combination of free and force convection which occurs due to the buoyancy force) is one of the principal figure which influences the molecule decay. Additionally, it is the main mode of mass moving in fluids and is regarded as a direct strategy for heat transfer. The main cause of such convection is due to temperature difference. The qualitative investigations have noteworthy bearing on several applications regarding mixed convection such as in atmospheric boundary layer, nuclear reactors, solar collectors, heat exchangers in electronic equipment, etc. Over the past few decades many attempts of buoyancy force flow of incompressible fluid towards different physical geometries have been taken. For example, Gorla [37] discussed the stagnant mixed convection (both for added and opposed buoyancy force) flow past over a heated stretching cylinder. He noted that in buoyancy-assisted flow region friction factor as well as fluid

temperature rises as the numeric value of mixed convection parameter grows, while inverse conduct is noted in the event of buoyancy-opposed flow region. The influence of the mixed convection flow about porous vertical cylinder was discussed by Bachok and Ishak [38]. Lok et al. [39] develop the computational algorithm of the buoyancy assistive/opposed stagnant flow towards stretching/shrinking surface. It was seen that for all values of stretching/shrinking ratio parameter buoyancy added flow solutions are possible, but there are limitations for buoyancy opposed flow solutions. Rehman et al. [40] studied the buoyancy assisting flow past over a stretching surface in the presence of double stratified medium. However, investigators are still engaged to explore hidden qualities regarding free convection, force convection or mixed convection flow of Newtonian and non-Newtonian flows namely [41-45].

Energy transfer is key element in various engineering and metallurgical processes for example in aerodynamic, polymer extrusion, crystal growth, artificial fibres, and drawing plastic films, etc. Gupta and Gupta [46] were the first who study the transfer of heat problem past a surface. It is understood fact that, thermal conductivity of the fluid changes appreciably when temperature increases. Particularly, in greases the internal friction produces increase in temperature, due to which thermal conductivity of fluid increases. Thus, for more practical approach, in recent literature temperature dependent conductivity is assumed. Chaim [47] studied the effect of temperature dependent conductivity in energy equation and found that energy of the fluid increases due to temperature dependent conductivity. Abel et al. [48] reported the impact of temperature dependent conductivity on power law fluid flow past a sheet. Ahmad et al. [49] did prodigious work by considering temperature dependent conductivity in a flow of viscous fluid past over a stretching plate.

16

Mishra et al. [50] inspected the time dependent thermo-physical properties of Newtonian fluid past a plate in changing conductivity of fluid. Recently, Rangi and Ahmed [51], Miao et al. [52], Manjunatha and Gireesha. [53], Si et al. [54] and Malik et al. [55] highlighted the fluid flows with the assumption of temperature dependent thermal conductivity in heat equation.

Impact of chemical reaction on mass and heat transfer have drawn much attention of researchers. Because it is encountered in different aspects of practical sciences e.g., agriculture, weather forecasting, thermal engineering, and chemical engineering. For instance, flow in a desert cooler evaporation, manufacturing of ceramics or glassware, and energy transfer in a cooling tower etc. Chemical reactions are of two kinds i.e., homogeneous, and heterogeneous. First kind of reaction happens uniformly through a given phase while later kind of reaction takes place in a confined region or within the boundary of a phase. But if the rate of reaction relates linearly with concentration, it is called of first order. Thus, due to extensive uses of chemical reactions, now-a-days analysis of chemical reaction experienced a period of great expansion and diversity. Chamka [56] reported the influence of 1st order chemical reaction on MHD fluid flow via permeable stretched surface. They suggested that chemical reaction reduces the concentration very significantly. Raptis and Perdikis [57] inspected the first order chemical reactions in a flow of MHD Newtonian fluid over non-linear stretched surface. They presented numerical solution and interpreted that chemical reaction cause's reduction in concentration. Bhattacharyya and Layek [58] explained influences of MHD and 1st order chemical reaction and on Newtonian fluid flow over a porous surface. The modelled boundary value problem is tackled through quasi-linearization method. Mabood et al. [59] presented

detailed analysis on first order chemical reactions in stagnant flow of hydromagnetic fluid through permeable stretching sheet and obtained numerical solution for feasible values of involving parameters. They predicted that chemical reactions have opposite influences on concentration and local Sherwood number. Recently, first order chemical reaction in boundary layer fluid flow was studied by Satya Narayana and Harish Babu [60], Abbas et al. [61], Zhang et al. [62] and Rehman et al. [63]. Even though, many researchers elaborate the thermal and solutal aspects of first order chemical reactions but in various practical situations higher order chemical reactions are to be found quite beneficial. Thus, many researchers considered the second or higher order chemical reactions in boundary layer flows. Afifi [64] explored the consequences of nth order chemical reactions on free convection flow of hydromagnetic viscous fluid over a stretched surface numerically and proved that the strength of chemical reactions decays the concentration profile while order of chemical reactions is found to be supportive for it. A theoretical analysis on this topic has been presented by Joneidi et al. [65] which addressed the influence of higher chemical reactions on boundary layer flow of hydromagnetic Newtonian fluid. They noticed that chemical reactions enlarge the fluid momentum, thermal energy, and concentration profiles. Rehman and Al-Lawatia [66] discussed the impact of higher order chemical reaction on hydromagnetic micropolar fluid flow past a permeable nonlinear stretching sheet. Ferdows and Al-Mdallal [67] studied the boundary layer fluid flow past a nonlinear stretching surface with higher order chemical reactions. Palani et al. [68] illustrated the higher order chemical reactions in boundary layer flow of non-Newtonian fluid past a stretched surface. They noticed that higher order of chemical reactions causes enhancement

in concentration profile. Malik and Rehman [69] also described the second order chemical reactions in hydromagnetic fluid flow over porous inclined stretching surface.

Chapter 1

Effects of viscous dissipation on MHD boundary layer flow of Sisko fluid over a stretching cylinder

Present chapter concentrates to observe the effects of magnetohydrodynamics flow of Sisko fluid past a stretching cylinder. The loss of energy in term of viscous dissipation effects are incorporated in energy equation. Application of boundary layer approximation plays an important role to formulate the governing PDEs. Appropriate symmetry transformations are used which converts these modified governing PDEs into a system of ODEs. Since this system of ODEs was highly non-linear and its analytical solution was not an easy task to handle the complexities appearing in the model. Therefore, shooting method in combination with R-K-Fehlberg technique is used to find the numerical solution of this system. The effects due to variation in physical parameters on momentum and energy equation are shown through graphs. Also, surface drag force and surface heat flux are displayed via figures and tables after varying involved physical parameters.

1.1 Mathematical formulation

Consider a time independent, 2-D, axisymmetric flow of Sisko fluid along the continuously stretching cylinder. The suface is stretched with velocity $U(x) = cx$. The magnetic field orthogonal to x-direction with strength B_0 is imposed. The influence of induced magnetic field and electric field is neglected. Also, the impact of viscous dissipation is assumed in heat equation. Physical regime of the current study is presented in **Fig.** 1.1. With these assumptions, the continuity, momentum, and heat equations are.

$$\frac{\partial(ru)}{\partial x} + \frac{\partial(rv)}{\partial r} = 0, \tag{1.1}$$

$$u\frac{\partial u}{\partial x} + v\frac{\partial u}{\partial r} = \frac{a}{\rho}\left(\frac{1}{r}\frac{\partial}{\partial r}\left(r\frac{\partial u}{\partial r}\right)\right) + \frac{b}{\rho}\left(\frac{1}{r}\frac{\partial}{\partial r}\left(r\frac{\partial u}{\partial r}\left|\frac{\partial u}{\partial r}\right|^{n-1}\right)\right) - \frac{\sigma B_0^2}{\rho}u, \tag{1.2}$$

$$u\frac{\partial T}{\partial x} + v\frac{\partial T}{\partial r} = \alpha\frac{\partial}{\partial r}\left(r\frac{\partial T}{\partial r}\right) + \frac{a}{\rho C_p}\left(\frac{\partial u}{\partial r}\right)^2 + \frac{b}{\rho C_p}\left(-\frac{\partial u}{\partial r}\right)^{n+1}. \tag{1.3}$$

Corresponding boundary conditions are.

$$u = U(x), v = 0, T = T_w \text{ at } r = R, \tag{1.4}$$
$$u \to 0, T \to T_\infty \text{ at } r \to \infty.$$
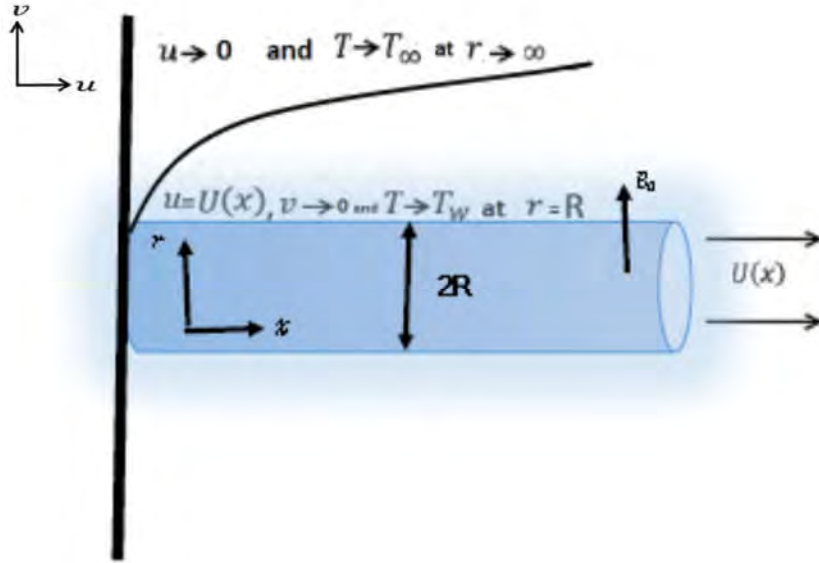
Fig. 1.1: Geometry of the problem.

Here u is the fluid velocity component along $x-$axis while v is along r – direction. σ is the electrical conductivity of the fluid, n (flow behaviour index), a and b are the material constants, ρ is the density, T is fluid the temperature, c_p is the specific heat, α is the thermal diffusivity, T_w is the surface temperature and T_∞ is ambient temperature.

The stream function Ψ is defined such that,

$$u = \frac{1}{r}\frac{\partial \Psi}{\partial r}, v = -\frac{1}{r}\frac{\partial \Psi}{\partial x}. \tag{1.5}$$

Suitable transformation which converts the governing PDEs into ODEs are defined as,

$$\eta = \frac{r^2 - R^2}{2Rx} Re_b^{\frac{1}{n+1}}, \ \Psi = RxU Re_b^{-\frac{1}{n+1}} f(\eta), \theta(\eta) = \frac{T - T_\infty}{T_w - T_\infty}, \tag{1.6}$$

where Re_b is defined as $Re_b = \frac{\rho U^{2-n} x^n}{b}$.

Using above similarity transformations, the $Eq.\,(1.1)$ is identically satisfied, while the $Eqs.\,(1.2) - (1.3)$ are transformed to,

$$A(1 + 2\gamma\eta)f''' + n\,(1 + 2\gamma\eta)^{\frac{n+1}{2}}(-f'')^{n-1}f''' + 2A\gamma f'' - f'^2 + \frac{2n}{n+1} ff''$$
$$- (n+1)\gamma(1 + 2\gamma\eta)^{\frac{n-1}{2}}(-f'')^n - Mf' = 0 \tag{1.7}$$

$$(1 + 2\gamma\eta)\theta'' + 2\gamma\theta' + \frac{2n}{n+1} Pr f\theta'$$
$$+ EcPrA(1 + 2\gamma\eta)f''^2 + EcPr(1 + 2\gamma\eta)^{\frac{n+1}{2}}(-f'')^{n+1} = 0. \tag{1.8}$$

Corresponding endpoint conditions

$$f(0) = 0, \ f'(0) = 1, \ \theta(0) = 1, f'(\infty) \to 0, \ \theta(\infty) \to 0. \tag{1.9}$$

Where dimensionless quantities mathematically defined as

$$M = \frac{\sigma x B_0^2}{\rho U}, A = \frac{Re_b^{\frac{2}{n+1}}}{Re_a}, E = \frac{U^2}{c_p(T_w - T_\infty)},$$
$$Pr = \frac{xU}{\alpha Re_b^{\frac{2}{n+1}}}, \gamma = \frac{x}{R Re_b^{\frac{1}{n+1}}}, Re_a = \frac{\rho Ux}{a}. \tag{1.10}$$

The quantities of practical concentration like surface drag force coefficient and surface heat flux are computed from following relations,

$$C_{fx} = \frac{\tau_w}{(1/2)\rho U^2}, \ Nu_x = \frac{xq_w}{k(T_w - T_\infty)}, \tag{1.11}$$

here,

$$\tau_w = \left[a\left(\frac{\partial u}{\partial r}\right) - b\left(-\frac{\partial u}{\partial r}\right)^n \right]_{r=R}, \ q_w = -k\left(\frac{\partial T}{\partial r}\right)_{r=R}, \tag{1.12}$$

Using Eq. (1.6) in Eqs. (1.11) − (1.12), the non-dimensional form of surface drag coefficient and surface heat flux defined as

$$\frac{1}{2}C_{fx}Re_b^{\frac{1}{n+1}} = Af''(0) - \left(-f'''(0)\right)^n, \quad Nu_xRe_b^{\frac{-1}{n+1}} = -\theta'(0). \qquad (1.13)$$

1.2 Computational Algorithm

The resulting equations i.e., Eqs. $(1.7) - (1.8)$ are highly nonlinear ODE's. The NS of governing equations is calculated with shooting method in conjunction with R-K-Fehlberg technique. As R-K-Fehlberg method solves only first order ODE's. Thus, system of higher order ODE's is transformed into a system of first order ODE's. For this purpose, governing equations are re-arranged as

$$f''' = \frac{f'^2 - 2\gamma Af'' + \gamma(n+1)(1+2\gamma\eta)^{\frac{n-1}{2}}(-f'')^n - \frac{2n}{n+1}ff'' + Mf'}{A(1+2\gamma\eta) + n(1+2\gamma\eta)^{\frac{n+1}{2}}(-f'')^{n-1}}, \qquad (1.14)$$

$$\theta'' = \frac{-\left(2\gamma\theta' + \Pr\left(\frac{2n}{n+1}\right)f\theta' + A(1+2\gamma\eta)Ec\Pr(f'')^2 + Ec\Pr(1+2\gamma\eta)^{\frac{n+1}{2}}(-f'')^{n+1}\right)}{(1+2\gamma\eta)}. \qquad (1.15)$$

Above equations i.e., Eqs. $(1.14) - (1.15)$ are of order three in f and order two in θ. Now five new variables are introduced to reduce Eqs. $(1.14) - (1.15)$ into a system of first order ODEs, which are defined in $Eq.\,(1.16)$.

$$f = y_1, f' = y_2, f'' = y_3, f''' = y'_3, \theta = y_4, \ \theta' = y_5, \ \theta'' = y'_5. \qquad (1.16)$$

After imposing Eq.(1.16) in Eqs. $(1.14) - (1.15)$ these are converted to system of ODE's i.e., Eqs. $(1.17) - (1.21)$ which are defined below,

$$y'_1 = y_2 \qquad (1.17)$$

$$y'_2 = y_3 \qquad (1.18)$$

$$y'_3 = \frac{\left(y_2^2 - 2\gamma Ay_3 + \gamma(n+1)(1+2\gamma\eta)^{\frac{n-1}{2}}(-y_3)^n - \frac{2n}{n+1}y_1y_3 + My_2\right)}{\left(A(1+2\gamma\eta) + n(1+2\gamma\eta)^{\frac{n+1}{2}}(-y_3)^{n-1}\right)}, \qquad (1.19)$$

$$y'_4 = y_5, \qquad (1.20)$$

y'_5

$$= \frac{-\left(2\gamma y_5 + \Pr\left(\frac{2n}{n+1}\right) y_1 y_5 + A(1 + 2\gamma\eta)Ec\Pr(y_3)^2 + Ec\Pr(1 + 2\gamma\eta)^{\frac{n+1}{2}}(-y_3)^{n+1}\right)}{(1 + 2\gamma\eta)}, \quad (1.21)$$

The subjected boundary conditions in new variables are,

$$y_1(0) = 0, y_2(0) = 1, y_2(\infty) = 0, y_4(0) = 1 \text{ and } y_4(\infty) = 0, \quad (1.22)$$

Now from *Eq.* (1.22) number of given conditions on initial point (i.e., $\eta = 0$) are three while the number of ODE's is five. Thus, to solve this system two fictious conditions for $y_2(\infty)$ and $y_4(\infty)$ are required. With these chosen fictious values for $y_2(0)$ and $y_4(0)$ the error tolerance criteria must be satisfied on boundary.

1.3 Physical and graphical outcomes

In present section variations in momentum and energy profiles are computed and presented for different values of relevant parameters. Also, precision of computed numerical solution is validated by equating it with existing literature.
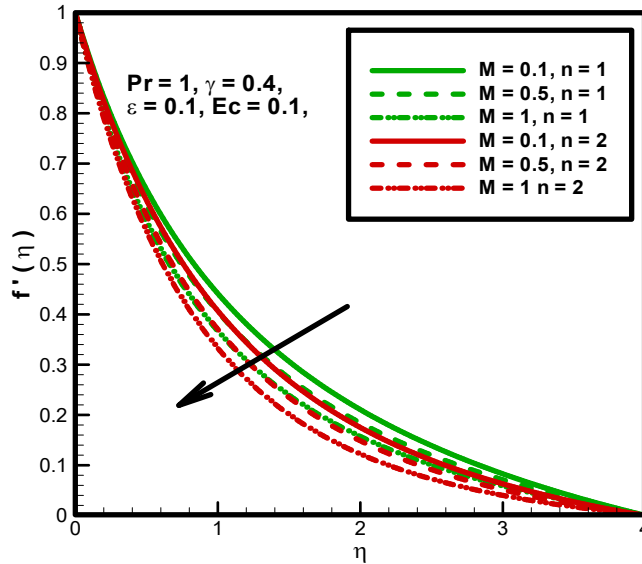
Fig. 1.2: Impact of M on $f'(\eta)$ for $n = 1,2$.
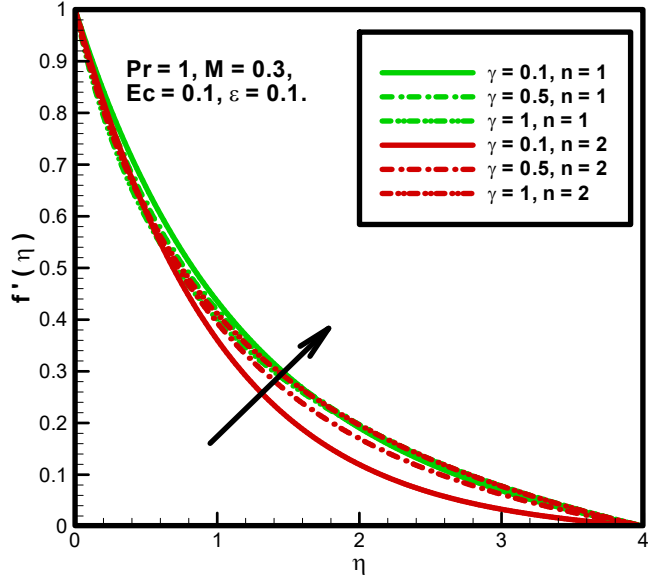
Fig. 1.3: Impact of γ on $f'(\eta)$ for $n = 1, 2$.
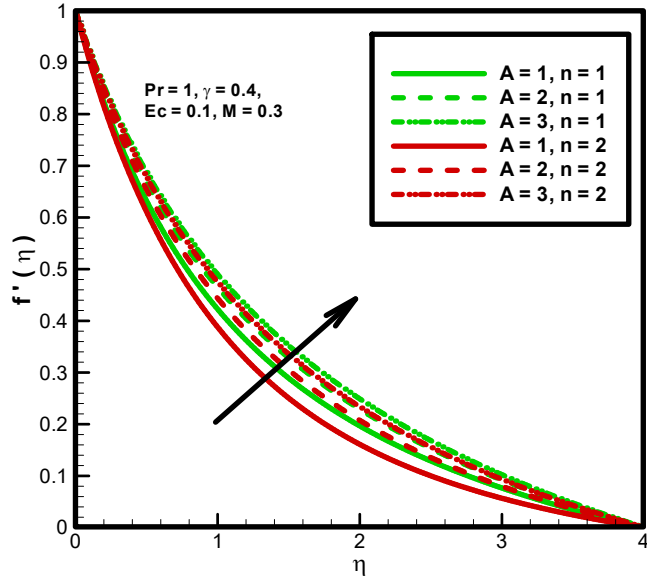
Fig. 1.4: Impact of A on $f'(\eta)$ for $n = 1, 2$.
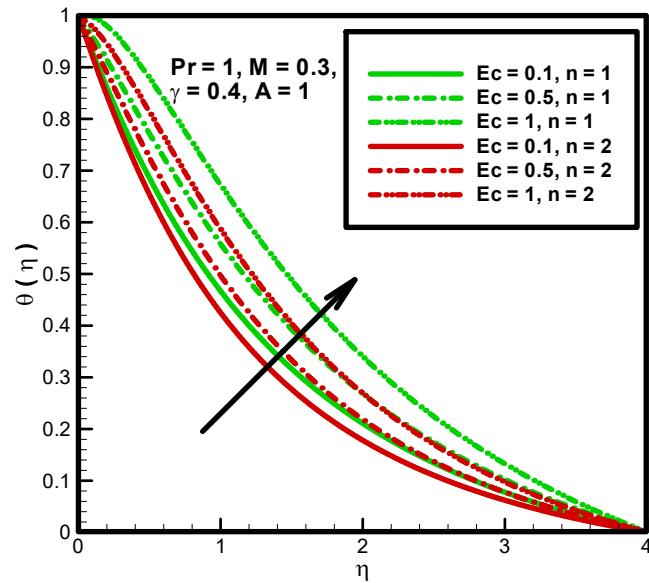
Fig. 1.5: Impact of Ec on $\theta(\eta)$ for $n = 1,2$.
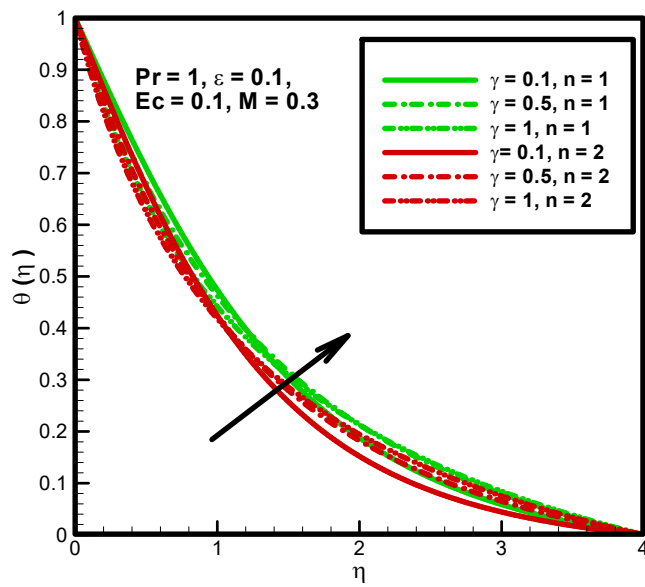
Fig. 1.6: Impact of γ on $\theta(\eta)$ for $n = 1,2$.
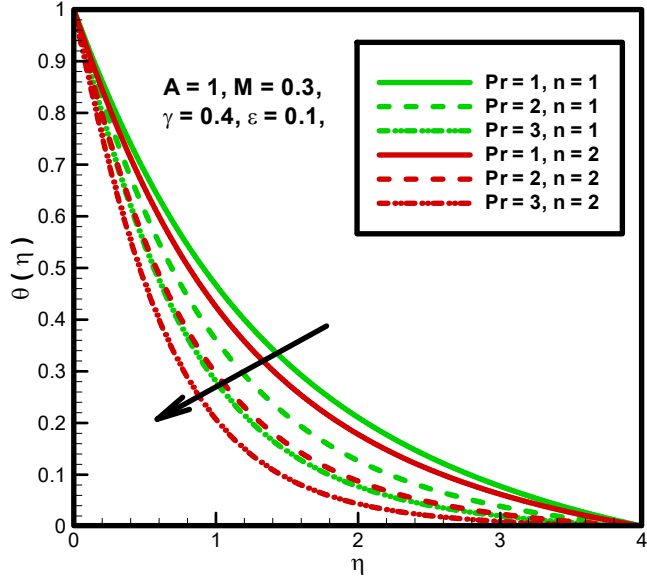
Fig. 1.7: Impact of Pr on $\theta(\eta)$ for $n = 1,2$.
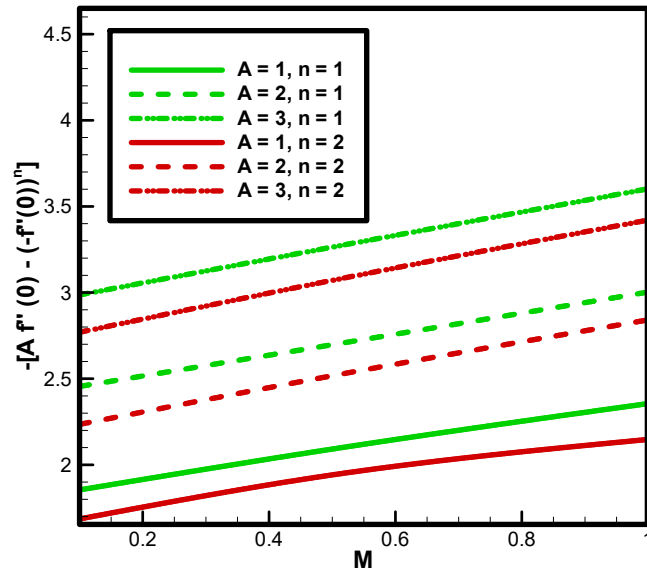
Fig. 1.8: Impacts of A and M on the skin friction coefficient.
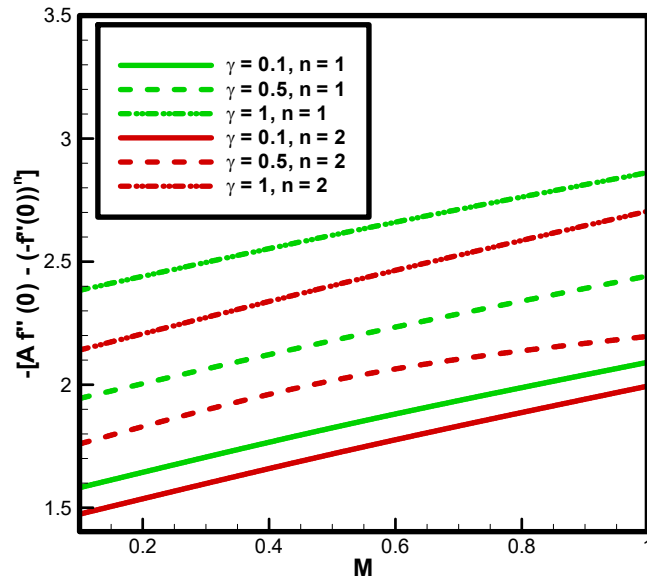
Fig. 1.9: Impacts of γ and M on the skin friction coefficient.

Fig. 1.10: Impacts of γ and Ec on the local Nusselt number.

28
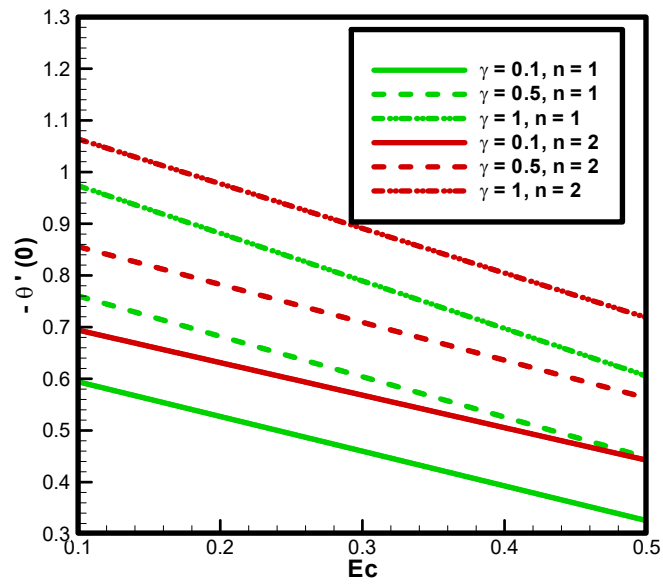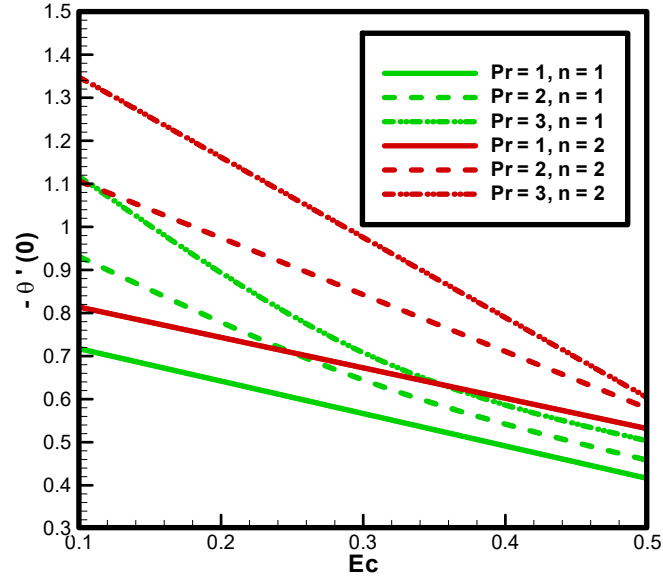
Fig. 1.11: Impacts of Pr and Ec on the local Nusselt number.

Fig. 1.2 illustrates the influence of M on the $f'(\eta)$ for different values of parameter n. As enhancement in M strength produces Lorentz force i.e., opponent force, which causes decrease in the velocity field. **Fig.** 1.3 expresses the impact of γ on the $f'(\eta)$ for $n = 1$ and 2. As radius of the cylinder diminishes when γ increases, it causes reduction in surface area. Hence it provides less opposition to fluid flow, consequently motion of the fluid accelerates. **Fig.** 1.4 shows the impact of the A on the $f'(\eta)$ for $n = 1$ and 2. The viscous forces become weaker when A increases, so less resistance is offered, which causes rise in the velocity of the fluid. Temperature distribution demonstrated in **Fig.** 1.5 for distinct values of Ec and n. As Ec is the relation between flow K.E to heat enthalpy. So, growth in Ec causes enrichment in the K.E. As temperature of the fluid is average K.E of the fluid particles. Thus, temperature of the fluid rises. It could be analysed from this graph that fluid temperature increases when Ec increases. **Fig.** 1.6 is created to discuss the behaviour of γ on $\theta(\eta)$ for $n = 1$ and 2. Since temperature is average K.E and increase in γ enhances the velocity as well as K.E, hence it increases the temperature. **Fig.** 1.7 describes the impact of Pr on $\theta(\eta)$. The thermal conductivity of the fluid declines by enhancing the Pr. (i.e. heat transfer slows down which reduces the temperature of flow

distribution). **Fig.** 1.8 displays the combined impacts of M, A and n on surface drag force coefficient. Effects of Ec and γ on wall heat flux are depicted via **Fig.** 1.9 by considering $n = 1,2$. Since Ec varies reciprocally with boundary layer enthalpy. As A Result, for $Ec > 0$ temperature difference decreases. Eventually, it decreases the amount of heat transfer from the surface. Conversely for $\gamma > 0$ heat transfer increases. Results of Ec and γ on surface heat flux are depicted via **Fig.** 1.10 by considering $n = 1,2$. Since Ec has reciprocal trend as of boundary layer enthalpy. Thus, when Eckert number inclines it declines difference between surface and ambient temperatures. Ultimately, it decreases the surface heat transfer rate. Also rate of heat transfer enlarges when curvature parameter and power law index increases. **Fig.** 1.11 expresses the variations in surface heat flux by varying Ec, Pr and n. The convective mode of heat transfer accelerates when high Pr is assumed, since Nusselt number is directly proportional to convective heat transfer, thus alternatively it increases. The fact can be verified from this figure.

Table 1.1: Comparison table of wall shear stress for different values of γ while $A = 0, M = 0, n = 1$.

γ	Rangi et al. [51]	Present Result
0	-1	-1.0007
0.25	-1.0944	-1.0950
0.50	-1.1887	-1.1899
0.75	-1.2818	-1.2835
1	-1.4593	-1.4585

Table 1.2: Variation in surface drag force coefficient for different values of parameter γ, M and A for $n = 1$ and 2.

γ	A	M	$(A+1)f''(0)$	$Af''(0) - f''^2(0)$
0	1	0.3	-1.8363	-1.6169
0.25			-2.0036	-1.8423
0.50			-2.1736	-2.0648
0.75			-2.3460	-2.2834
0.4	1		-2.1736	-1.9763
	2		-2.5645	-2.7025
	3		-3.1192	-3.2565
	4		-3.6562	-3.8168
	1	0	-1.7908	-1.9188
		0.25	-1.9465	-2.1321
		0.50	-2.0916	-2.3350
		0.75	-2.2278	-2.5286

Table 1.3: surface heat flux for different values of parameter $\gamma, Ec, \Pr$ and $n = 1,2$.

γ	$\Pr$	Ec	$(n=1)$ $-\theta'(0)$	$(n=2)$ $-\theta'(0)$
0	1	0.1	0.5592	0.6415
0.25			0.6467	0.7376
0.5			0.7475	0.8408
0.75			0.8499	0.9407
0.4	1		0.7067	0.7761
	2		0.9114	0.9906
	3		1.0891	1.1743
	4		1.2402	1.3284
	1	0	0.7927	0.8429
		0.25	0.5777	0.6897
		0.5	0.3626	0.5064

		0.75	0.1476	0.3232

In **Table** 1.1 the comparison between present and previously computed literature, (Rangi et al. [51]) numerical values of surface drag force coefficient for different values of γ is displayed. Both values are agreed up to 4 significant digits. **Table** 1.2 is created to examine the influence of n, γ, M and A on wall shear stress. It can be noted from table that for positive values of n, γ, M and A surface drag force coefficient also increases. **Table** 1.3 investigates the influence of γ, Ec and Pr on wall heat flux for $n = 1,2$. It can be noted from table that surface heat flux rises by rising γ and Pr, while it diminishes by increasing the Eckert number Ec.

1.4 Conclusion

A theoretical study is done to examine the numerical solution of BL flow of Sisko fluid over a stretching cylinder with the shared effects of applied magnetic field and viscous dissipation. The following results are acquired:

- The fluid velocity increases by increasing both A and γ, Whereas, M decelerates the velocity.
- Energy in the fluid increases when γ and Ec are increases while the impact of Pr on fluid temperature is opposite.
- Wall shear stress increases for large values of A, M and γ while it decays when power law index varies from $n = 1$ to $n = 2$.
- Numerical values of wall heat flux enhances by enhancing γ, Pr and n while it declines for larger values of Ec.

Chapter 2

Magnetohydrodynamic (MHD) flow of Sisko fluid near the axisymmetric stagnation point towards a stretching cylinder

This chapter explores the momentum and energy transfer of hydromagnetic mixed convection stagnant flow of Sisko fluid over a stretching cylinder. Appropriate suitable transformations are carefully chosen to convert the PDEs system into ODEs system. High tolerance error and large mesh size is considered for the convergence analysis of the numerical scheme. Graphical assessment is exhibited to examine the behaviour of involved parameters on concerning profiles. For better explanation of fluid flow surface drag force coefficient and surface heat flux is scrutinized via graphs and tables.

2.1 Mathematical formulation

Let us consider a time independent, 2D, hydromagnetic mixed convection stagnant flow of Sisko fluid past over a stretching cylinder under polar cylindrical coordinates (r, θ, x) with velocity components (u, v, w). The coordinate system is chosen such that the x $-$axis is along the cylinder and r $-$axis is normal to the cylinder and stretched along x $-$axis with velocity $U_w(x) = cx$, where $c > 0$ is the parameter of constant acceleration. The magnetic field of strength B_0 is applied normal to the $x -$ axis. Cylinder is continuously stretched along axial direction from both sides with velocity U_w as shown in **Fig**. 2.1. With these suppositions and boundary layer approach the governing continuity, momentum and energy equations are

$$\frac{\partial(ru)}{\partial x} + \frac{\partial(rv)}{\partial r} = 0, \tag{2.1}$$

$$u\frac{\partial u}{\partial x} + v\frac{\partial u}{\partial r} = \frac{a}{r\rho}\frac{\partial}{\partial r}\left(\frac{r\partial u}{\partial r}\right) - \frac{b}{r\rho}\frac{\partial}{\partial r}\left(r\left(-\frac{\partial u}{\partial r}\right)^n\right) + g\beta(T_w - T_\infty) - \sigma\frac{B_0^2}{\rho}(u - U_\infty), \tag{2.2}$$

subject to the momentum endpoint conditions,

$$u = U_w(x) = cx, \ v = 0, \ \text{at} \ r = R$$
$$u = U_\infty(x) = dx, \ \text{as} \ r \to \infty. \tag{2.3}$$
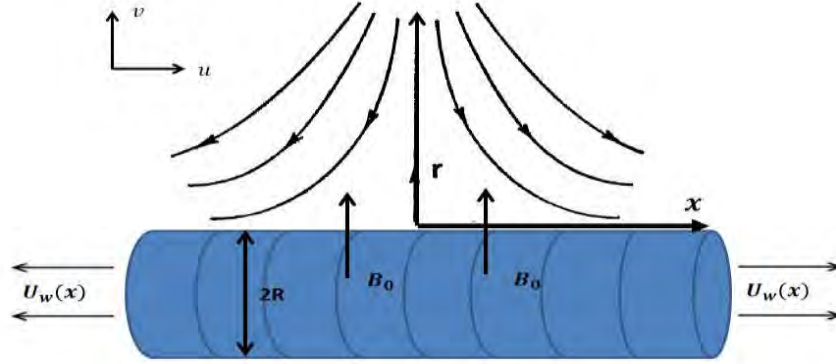
Fig. 2.1: Geometry of the problem.

The outer wall of the cylinder is kept at uniform temperature T_w. The energy equation after applying boundary layer approximations is as follows,

$$u\frac{\partial T}{\partial x} + v\frac{\partial T}{\partial y} = \frac{\alpha}{r}\frac{\partial}{\partial r}\left(r\frac{\partial T}{\partial r}\right) + \frac{\sigma B_0^2}{\rho c_p}u^2. \tag{2.4}$$

The corresponding boundary conditions are as follows,

$$T = T_w(x) \ \text{at} \ r = R,$$
$$T \to T_\infty(x) \ \text{as} \ r \to \infty. \tag{2.5}$$

By choosing a stream function Ψ defined as

$$u = \frac{1}{r}\frac{\partial \Psi}{\partial r}, \ v = \frac{-1}{r}\frac{\partial \Psi}{\partial x}.$$

(2.6)

The continuity Eq. (2.1) is identically satisfied. The following local similarity transformations

$$\eta = \frac{r^2 - R^2}{2Rx} Re_b^{\frac{1}{n+1}}, \ \Psi = RxU Re_b^{-\frac{1}{n+1}} f(\eta),$$

$$\theta(\eta) = \frac{T - T_\infty}{T_w - T_\infty}, \ Re_b = \frac{\rho U^{2-n} x^n}{b},$$

(2.7)

The non-dimensional form of Eqs. (2.2) − (2.4), after using Eq. (2.7) is defined as,

$$A(1 + 2\gamma\eta)f''' + n(1 + 2\gamma\eta)^{\frac{n+1}{2}}(-f'')^{n-1}f''' + 2\gamma Af''\frac{2n}{n+1}ff'' - f'^2 + \lambda\theta + B^2$$

$$-(n+1)\gamma(1 + 2\gamma\eta)^{\frac{n-1}{2}}(-f'')^n + -M(f' - B) = 0,$$

(2.8)

$$(1 + 2\gamma\eta)\theta'' + +2\gamma\theta' + \frac{2n}{n+1}\text{Pr}f\theta' + MEc\text{Pr}f'^2 = 0,$$

(2.9)

the transformed boundary conditions are,

$$f(\eta) = 0, \ f'(\eta) = 1, \ \theta(\eta) = 1 \text{ at } \eta = 0,$$

$$\lim_{\eta\to\infty} f'(\eta) = B, \ \lim_{\eta\to\infty} \theta(\eta) = 0.$$

(2.10)

The dimensionless parameters in Eqs. (2.8) and (2.9) are defined as,

$$\text{Pr} = \frac{xU}{\alpha Re_b^{\frac{2}{n+1}}}, \ A = \frac{Re_b^{\frac{2}{n+1}}}{Re_a}, \lambda = \frac{g\beta x(T_w - T_\infty)}{U^2}, \ \gamma = \frac{x}{RRe_b^{\frac{1}{n+1}}},$$

$$Re_b = \frac{\rho U^{2-n} x^n}{b}, \ B = \frac{d}{c}, M = \frac{\sigma x B_0^2}{U\rho}, \ Re_a = \frac{\rho Ux}{a}.$$

(2.11)

Surface drag force coefficient and surface heat flux for present analysis are defined as

$$C_{fx} = \frac{\tau_w}{(1/2)\rho U^2}, \ Nu_x = \frac{xq_w}{k(T_w - T_\infty)},$$

(2.12)

where τ_w and q_w are surface shear stress and surface heat flux described as

$$\tau_w = \left[a\left(\frac{\partial u}{\partial r}\right) - b\left(-\frac{\partial u}{\partial r}\right)^n\right]_{r=R}, \ q_w = -k\left(\frac{\partial T}{\partial r}\right)_{r=R},$$

using Eq. (2.7) in Eq. $(2.12) - (2.13)$, the non-dimensional forms are defined as

$$\frac{1}{2}C_{fx}Re_b^{\frac{1}{n+1}} = Af''(0) - \left(-f'''(0)\right)^n, \quad Nu_x Re_b^{\frac{-1}{n+1}} = -\theta'(0),$$

(2.14)

2.2 Computational algorithm

The analytical solution of ordinary differential Eqs. $(2.8) - (2.9)$ are intractable because these equations are highly nonlinear. To solve this system of equations numerically, shooting method with R-K Fehlberg technique is used. For this, initially Eqs. $(2.8) - (2.9)$ are modified to the following form:

$$f''' = \frac{f'^2 - 2\gamma Af'' + \gamma(n+1)(1+2\gamma\eta)^{\frac{n-1}{2}}(-f'')^n - \frac{2n}{n+1}ff'' - \lambda\theta - B^2 + M(f'-B)}{A(1+2\gamma\eta) + n(1+2\gamma\eta)^{\frac{n+1}{2}}(-f'')^{n-1}},$$

(2.15)

$$\theta'' = \frac{-\left(2\gamma\theta' + \Pr\left(\frac{2n}{n+1}\right)f\theta' + MEc\Pr f'^2\right)}{(1+2\gamma\eta)}.$$

(2.16)

Introducing the new set of dependent variables given below

$$f' = y'_1 = y_2,$$

(2.17)

$$f'' = y'_2 = y_3,$$

(2.18)

$$f''' = y'_3 = \frac{1}{(A(1+2\gamma\eta) + n(1+2\gamma\eta)^{\frac{n+1}{2}}(-y_3)^{n-1})}(y_2^2 - 2\gamma Ay_3 +$$

(2.19)

$$\gamma(n+1)(1+2\gamma\eta)^{\frac{n-1}{2}}(-y_3)^n - \frac{2n}{n+1}y_1y_3 - \lambda y_4 - B^2 + M(y_2 - B))$$

$$\theta' = y'_4 = y_5,$$

(2.20)

$$\theta'' = y'_5 = \frac{-\left(2\gamma\theta' + \Pr\left(\frac{2n}{n+1}\right)y_1y_5 + MEc\Pr y_2^2\right)}{(1+2\gamma\eta)}.$$

(2.21)

The boundary conditions take the form as:

To solve system of Eqs. $(2.17) - (2.21)$, five initial conditions are required, but the initial

$$y_1 = 0, \; y_2 = 1, \; y_4 = 1, \; \text{at } \eta = 0,$$

(2.22)

$$y_2 \to B, \; y_4 \to 0, \; \text{as } \eta \to \infty.$$

Express two unknown initial conditions with H_1 and H_2. i.e.

$$y_1 = 0, \; y_2 = 1, \; y_3 = H_1,$$

36

$$y_4 = 1, \ y_5 = H_2. \tag{2.23}$$

To exploit these two unknowns, a suitable finite value must be given to η_∞. Thus to estimate the values of similarity variable η_∞, start with some initial approxiamtions and solve the boundary value problem consisting of Eqs. $(2.17) - (2.21)$ to approximate H_1 and H_2. The solution process is repeated for different values of η_∞ until two successive values of H_1 and H_2 satisfies the boundary residual given below.

$$\varphi_1(H_1, H_2) = 0.1, \ \varphi_2(H_1, H_2) = 0. \tag{2.24}$$

2.3 Physical and graphical outcomes

This section is fascinated to a comprehensive study of numerically calculated results and impacts of all relevant parameters on temperature and velocity. Moreover, surface drag force coefficient and surface heat flux are presented in graphical and tabular form. The shows the effects of the dimensionless parameters namely Sisko parameter A, Hartmann number M, mixed convection parameter λ, velocity ratio parameter B, curvature parameter γ and Prandtl number Pr.
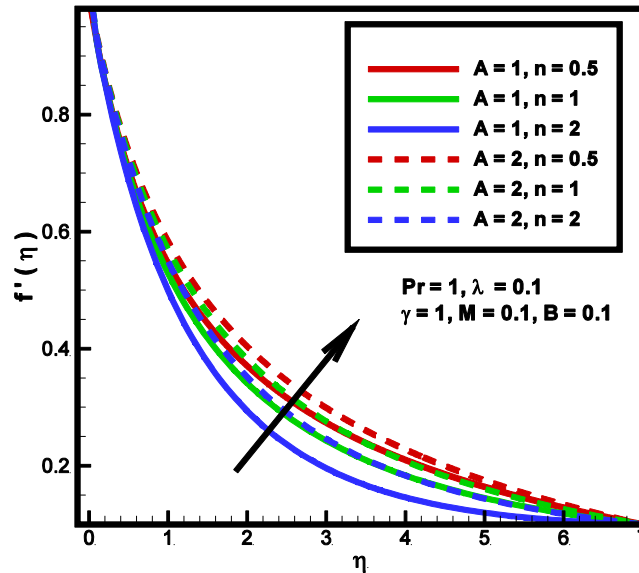
Fig. 2.2: Variation of A on $f'(\eta)$.
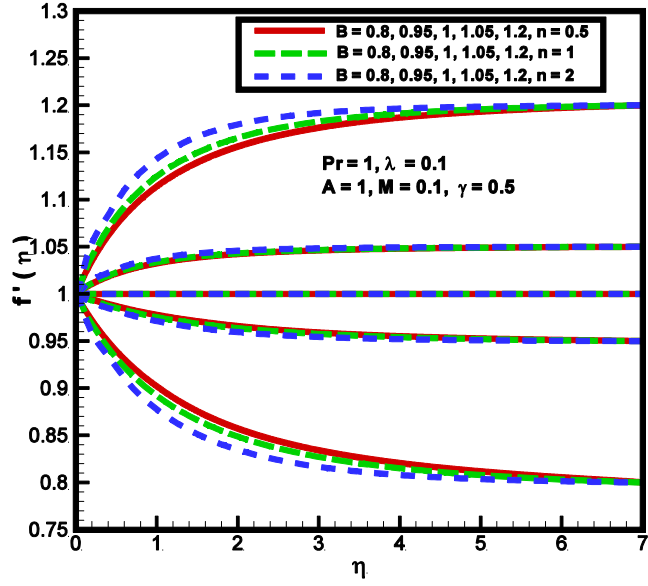
Fig. 2.3: Variation of B on $f'(\eta)$.
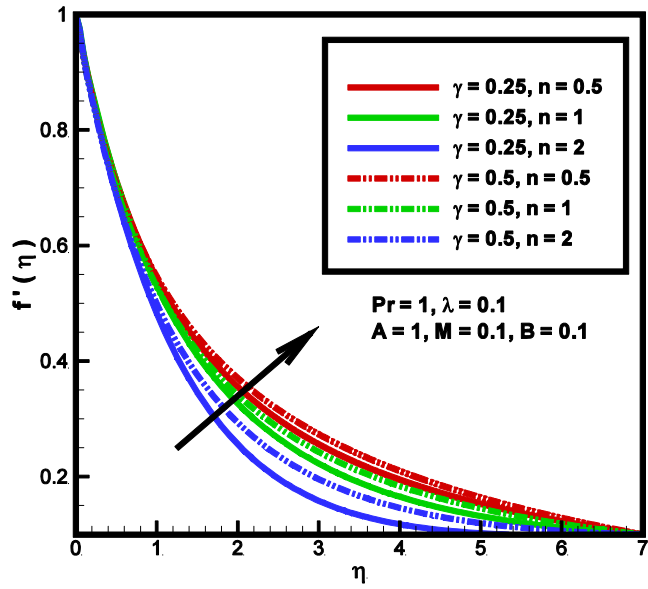
Fig. 2.4: Variation of γ on $f'(\eta)$.
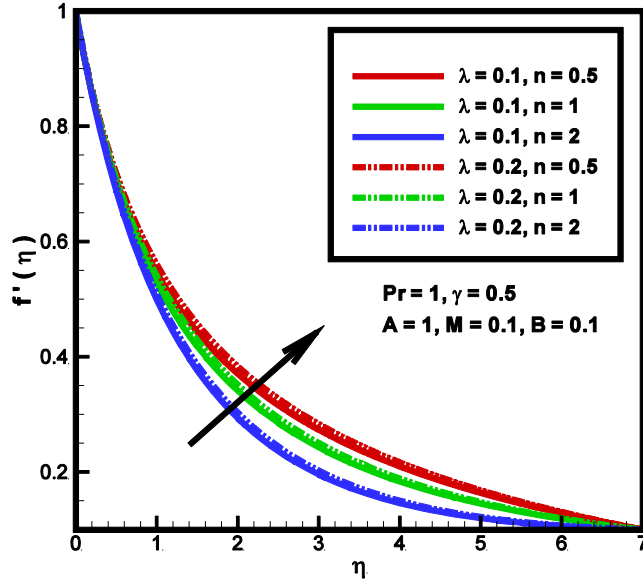
Fig. 2.5: Variation of λ on $f'(\eta)$.
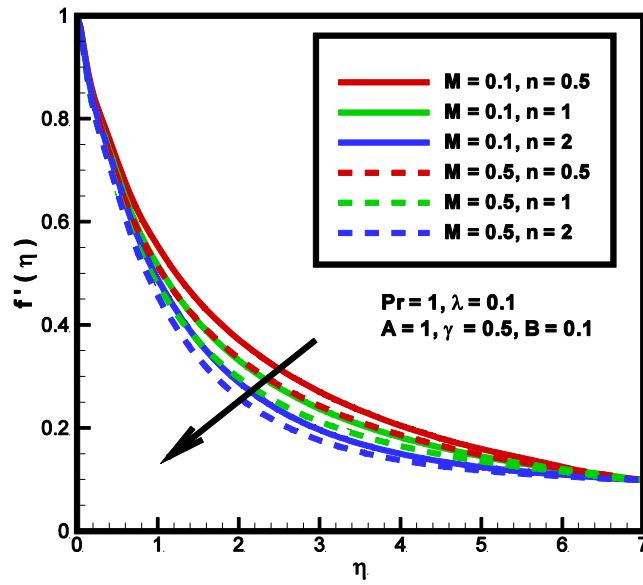
Fig. 2.6: Variation of M on $f'(\eta)$.
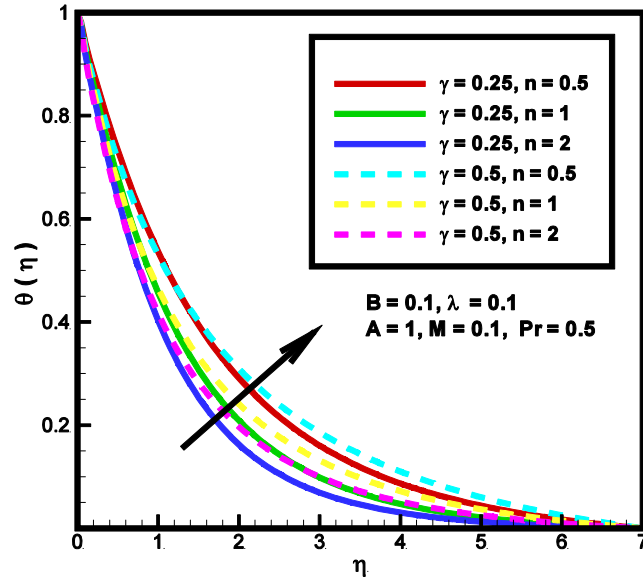
Fig. 2.7: Variation of γ on $\theta(\eta)$.
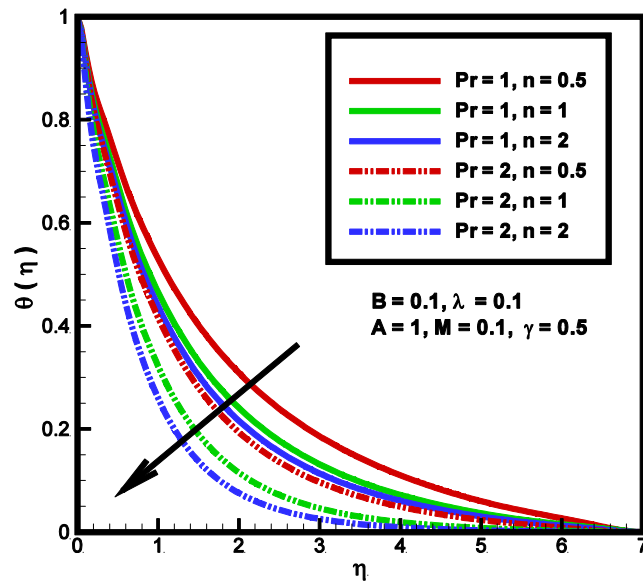
Fig. 2.8: Variation of Pr on $\theta(\eta)$.
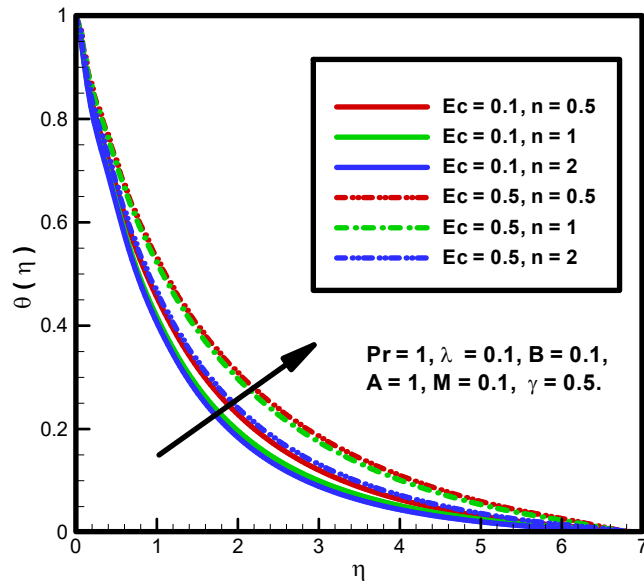
Fig. 2.9: Variation of Ec on $\theta(\eta)$.
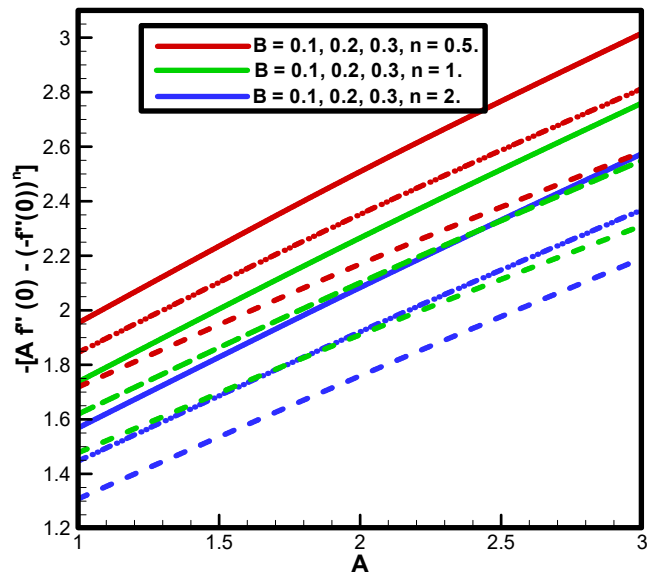
Fig. 2.10: Variations of B, A and n on wall shear stress.
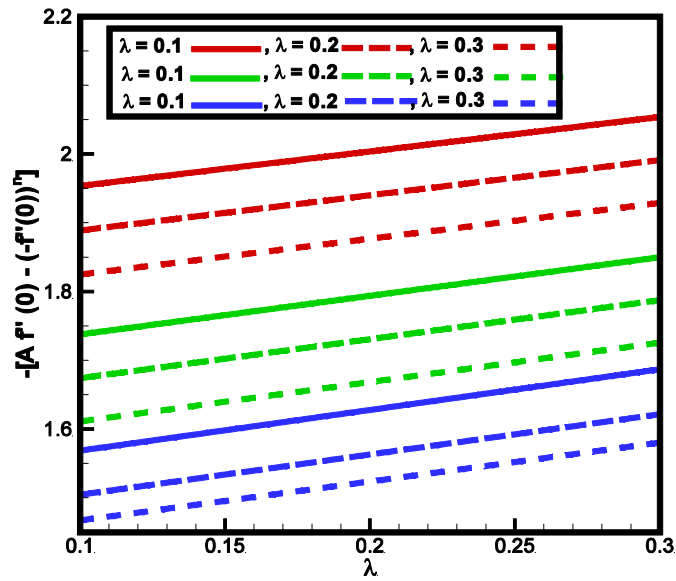
Fig. 2.11: Variations of λ, M and n on wall heat flux.
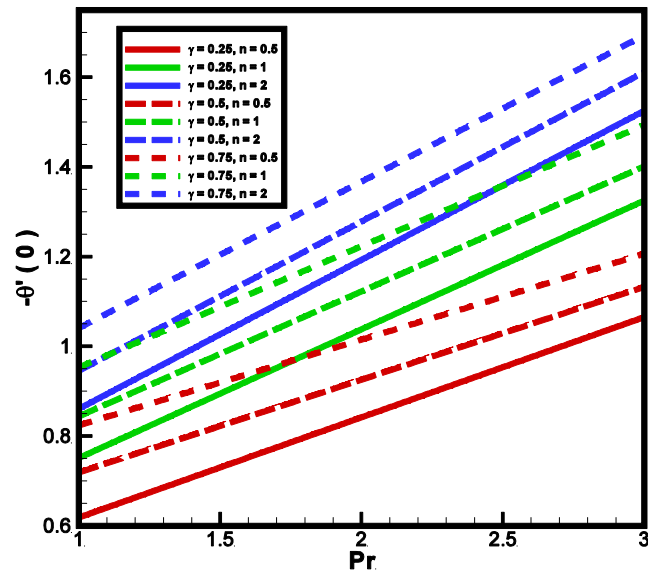
Fig. 2.12: Variations of $\gamma,$ Pr and n on wall heat flux.
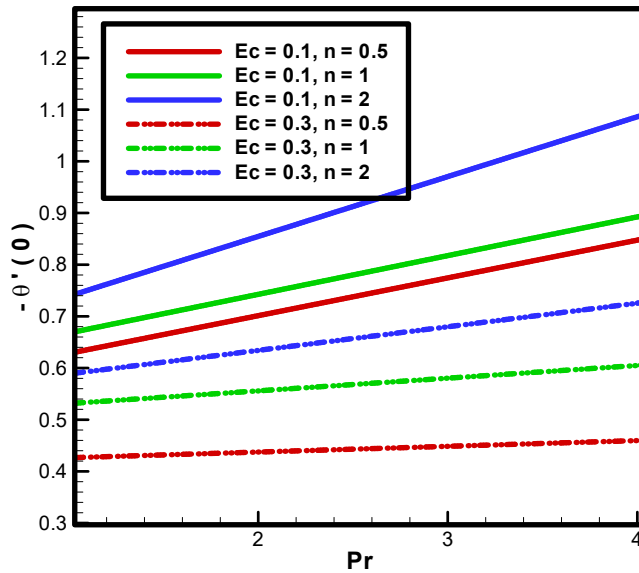
Fig. 2.13: Variations of Ec, Pr and n on wall heat flux.

Fig. 2.2 describes the behaviour of the momentum profile for several values of A and n. An analysis reveals that n play a key role. Because the behaviour of fluid changes from shear thinning to shear thickening fluid. As shear thickening fluid is more viscous than Newtonian and shear thinning fluids. Hence by increasing flow behaviour index velocity profile decreases. Also, it clearly shows that increasing material parameter, velocity profile increases. Physically, by increasing A, inertial force of fluid increases which decreases the viscous force and hence the momentum profile increases. **Fig.** 2.3 expresses the impact of B on dimensionless momentum profile. It is perceived that for $B < 1$ BL thickness decreases but velocity profile increases for $B > 1$ it has opposite effect. For $B = 1$ there is no information about boundary. **Fig.** 2.4 reveals that velocity exceeds on incrementing γ but opposite behaviour is noted for n. **Fig.** 2.5 demonstrates the behaviour of λ and n on the dimensionless momentum profile. It is perceived that by increasing λ momentum profile rises. Also, it is witnessed that for greater values of λ, momentum boundary layer thickness increases. **Fig.** 2.6 specifies the imposition of M on the velocity profile. Since an growth in M directs an increase in the Lorentz force. Strong Lorentz forces yield more opposition to the momentum transport, thus the higher values of M, causes decrease in

momentum profile. **Fig.** 2.7 shows the influence of γ on energy profile for different n. It is perceived that the energy profile and the corresponding thermal BL thickness decreases as the values of power law index increases. Also, it is noted that for $\gamma > 0$, thermal BL thickness reduces. **Fig.** 2.8 is sketched to see the impact of Pr on dimensionless energy profile. It is perceived that for higher Pr, thermal BL thickness becomes thinner, which produces a decline in the energy profile. The temperature distributions of Newtonian and non-Newtonian fluids are displayed in **Fig.** 2.9 for $Ec > 0$. As Ec increases the K.E, so fluid particle collides frequently with each other and dissipate the energy i.e., the K.E is converted into thermal energy, consequently fluid temperature increase. **Fig.** 2.10 shows the influence of B, A and n on surface drag force coefficient. It is observed that surface offer less resistance when B increases, because BL thickness progressively decreases when $B > 0$. Moreover, surface resistance coefficient enhances with an enhancement in A. Since A increases BL thickness which causes an increase in surface drag forc coefficient. **Fig.** 2.11 demonstrates the graphical representation of wall shear stress by varying γ, A and n. Hence it is perceived that the absolute value of surface resistance rises by rising A and γ, while decreases by increasing n. Since the γ has an inverse relation with Reynolds number and Reynolds number has inverse relation with skin friction coefficient. Thus, on increasing curvature parameter, Reynolds number decreases which ultimately improves the values of wall shear stress. Finally, by increasing flow behaviour index wall shear stress decreases because fluid changes from shear thinning to Newtonian and then shear thickening fluid, which ultimately causes a decrease in boundary layer thickness and hence fluid viscosity increases. As a result, wall shear stress reduces by increasing n. **Fig.** 2.12 depicts the behaviour of γ, Pr and n on wall heat flux. It is evident that by increasing γ wall heat flux increases. Since increase of γ causes the decrease in temperature near to the surface of the cylinder, therefore the thermal BL becomes thinner which causes an enhancement in a temperature gradient. From this figure, one can also observe that, by increasing Pr, local Nusselt number increases. Physically, Pr causes a decrease in temperature, which increases the temperature difference. Hence it leads to increase in the rate of heat transfer from the surface of cylinder increases. Furthermore, this graph also shows that by increasing n wall heat flux increases. **Fig.** 2.13 explains the behaviour of Ec and Pr on surface heat flux. For higher values of Ec, the

temperature difference i.e., $T_w - T_\infty$ decreases. As a result, heat transfer rate decreases which cause a decrease in the wall heat flux. Also, it is also shown in this fig that Pr increases the values of wall heat flux. Because for higher Pr fluid conductivity decreases.

Table 2.1: Comparison of present paper with published literature when $\gamma = A = \text{Pr} = \lambda = B = 0$ but $n = 1$.

M	Akbar et al. [32]	Present Results
0	-1	-1
0.5	-1.11803	-1.1180
1	-1.41421	-1.4141
5	-2.44949	-2.4495
10	-3.31663	-3.3166

Table 2.2: Variation of $\frac{1}{2}C_{fx}\sqrt{\text{Re}_b}$ with respect to γ, A, λ, M and B.

γ	A	λ	M	B	$n = 0.5, f''(0)$	$n = 1, f''(0)$	$n = 2, f''(0)$
0.25	1	0.1	0.1	0.1	-1.7316	-1.5535	-1.4233
0.5	-	-	-	-	-1.9533	-1.7373	-1.5686
0.75	-	-	-	-	-2.1616	-1.9187	-1.7159
0.5	1	-	-	-	-1.9533	-1.7373	-1.5686
-	2	-	-	-	-2.5086	-2.2655	-2.0834
-	3	-	-	-	-3.0166	-2.764	-2.5744
-	1	0.1	-	-	-1.9533	-1.7373	-1.5686
-	-	0.2	-	-	-1.8885	-1.6736	-1.5042
-	-	0.3	-	-	-1.8244	-1.6107	-1.4669
-	-	0.1	0.1	-	-1.9533	-1.7373	-1.5686
-	-	-	0.2	-	-2.0043	-1.7943	-1.5042
-	-	-	0.3	-	-2.0537	-1.7943	-1.5042
-	-	-	0.1	0.1	-1.9533	-1.8496	-1.4669
-	-	-	-	0.2	-1.8452	-1.6191	-1.4496
-	-	-	-	0.3	-1.7184	-1.4747	-1.3083

Table 2.3: Variation of $-\theta'(0)$ with respect to $\gamma, \mathrm{Pr}, \lambda, B, Ec$ and M.

γ	Pr	λ	B	Ec	M	$n = 0.5, -\theta'(0)$	$n = 1, -\theta'(0)$	$n = 2, -\theta'(0)$
0.25	1	0.1	0.1	0.1	0.1	0.6053	0.7337	0.8369
0.5	-	-	-	-	-	0.7091	0.8292	0.9277
0.75	-	-	-	-	-	0.8159	0.9286	1.0252
0.5	1	-	-	-	-	0.7091	0.8292	0.9277
-	2	-	-	-	-	0.9287	1.1353	1.2985
-	3	-	-	-	-	1.1234	1.3924	1.5948
-	1	0.1	-	-	-	0.7091	0.8292	0.9277
-	-	0.2	-	-	-	0.7130	0.8334	0.9321
-	-	0.3	-	-	-	0.7169	0.8375	0.9517
-	-	0.1	0.1	-	-	0.7091	0.8292	0.9277
-	-	-	0.2	-	-	0.7227	0.8454	0.9455
-	-	-	0.3	-	-	0.7371	0.8624	0.9638
-	-	-	0.1	0.1	-	0.7091	0.8292	0.9277
-	-	-	-	0.2	-	0.7035	0.8236	0.9225
-	-	-	-	0.3	-	0.6980	0.8181	0.9171
-	-	-	-	0.1	0.1	0.7091	0.8292	0.9277
-	-	-	-	-	0.2	0.7007	0.8199	0.9186
-	-	-	-	-	0.3	0.6928	0.8110	0.9099

Table 2.1 provides the comparison of this analysis with the published literature for different values of M. **Table** 2.2 show the influence of involve parameters γ, A, λ and B on wall shear stress for changing values of n. From the table it can be shown that surface resistance coefficient is increasing for larger values of n, γ, A and M. Since increase in these parameters increase the BL thickness, so the viscous forces near the surface become stronger. Which is a cause of increase in coefficient of skin friction. Whereas skin drag decreases for positive λ and B. **Table** 2.3 describes the variations in temperature gradient for change in physical parameters $\gamma, \mathrm{Pr}, \lambda, B$, Ec and M. When flow parameters $\gamma, \mathrm{Pr}, \lambda$, and B increases it shrinks the thermal BL. Thus, the values of $-\theta'(0)$ enhances

when larger values are awarded to parameters γ, Pr, λ and B. On the other hand, if values of physical parameters Ec and M increases it causes a decline in temperature gradient coefficient. This is physically valid because when positive values of Ec and M are considered the thermal boundary layer becomes thicker hence wall heat flux decreases.

2.4 Conclusions

A theoretical study is presented to exploit physical features of hydromagnetic mixed convection stagnant flow of Sisko fluid past a linearly stretching cylinder. The converted ODEs were solved numerically by using a shooting technique together with R-K-Fehlberg integration scheme, to analyse the outcomes of different embedded parameters on momentum and energy profiles graphically and quantitatively. The main findings of this analysis are:

- Strength of the M reduces the velocity profile but causes an increase in temperature.
- There is a direct relation of the γ with velocity and temperature profiles.
- The material parameter A and λ enhances the momentum BL thickness.
- The flow behaviour index n reduces both velocity and temperature profiles. But influence of n is opposite on the surface drag coefficient and on temperature gradient coefficient.
- Velocity ratio parameter B reduces the thermal resistance but causes an increase in the momentum profile.
- An enhancement in the surface drag coefficient is noticed against M.
- The parameters M and Ec both impart the considerable decrease in local Nusselt number.

Chapter 3

A computational analysis subject to thermophysical aspects of Sisko fluid flow over a cylindrical surface

Prominent characteristics of Sisko fluid under mixed convection and non-linear thermal radiation effects over an inclined cylinder is explored in this chapter. Heat transfer aspects are taken via convective boundary conditions and variable thermal conductivity. The BL methodology is applied to build the mathematical model in the form of PDEs. These requisite PDE's are converted into the complex ordinary ODEs system by using suitable similarity transformations. The results of subsequent ODEs is achieved by applying shooting scheme with R-K algorithm (fifth order). The graphical results are produced to explain the silent characteristics of engaged flow parameters on concerning profiles. For a better picture of fluid flow, numerical variation in surface drag force coefficient and surface heat flux coefficient is inspected in tables. Finally, the achieved results are justified by comparing with the existing literature.

3.1 Mathematical formulation

Consider a time independent, 2D, incompressible, buoyancy assistive flow of Sisko fluid past an inclined stretching cylinder. Assume that the surface is convectively heated i.e., heat can be generated/absorbed due to non-linear thermal radiation and temperature dependent conductivity. The fluid flow is assumed to be along the cylinder (i.e., in the x-axis) which is stretched continuously, velocity components are u and v along x and r directions respectively as shown in **Fig**. 3.1. Generalized continuity, momentum, and energy equations, under usual BL and Boussinesq approximations are given as

$$\frac{\partial(ru)}{\partial x} + \frac{\partial(rv)}{\partial r} = 0, \qquad (3.1)$$

$$u\frac{\partial u}{\partial x} + v\frac{\partial u}{\partial r} = \frac{a}{r\rho}\frac{\partial}{\partial r}\left(\frac{r\partial u}{\partial r}\right) - \frac{b}{r\rho}\frac{\partial}{\partial r}\left(r\left(-\frac{\partial u}{\partial r}\right)^n\right) + g\beta(T_w - T_\infty)\cos\alpha_t, \qquad (3.2)$$

$$u\frac{\partial T}{\partial x}+v\frac{\partial T}{\partial y}=\frac{1}{r\rho c_p}\frac{\partial}{\partial r}\left(rk(T)\frac{\partial T}{\partial r}\right)+\frac{Q_0}{\rho c_p}(T-T_\infty)-\frac{1}{\rho c_p}\frac{\partial q_r}{\partial r}, \qquad (3.3)$$
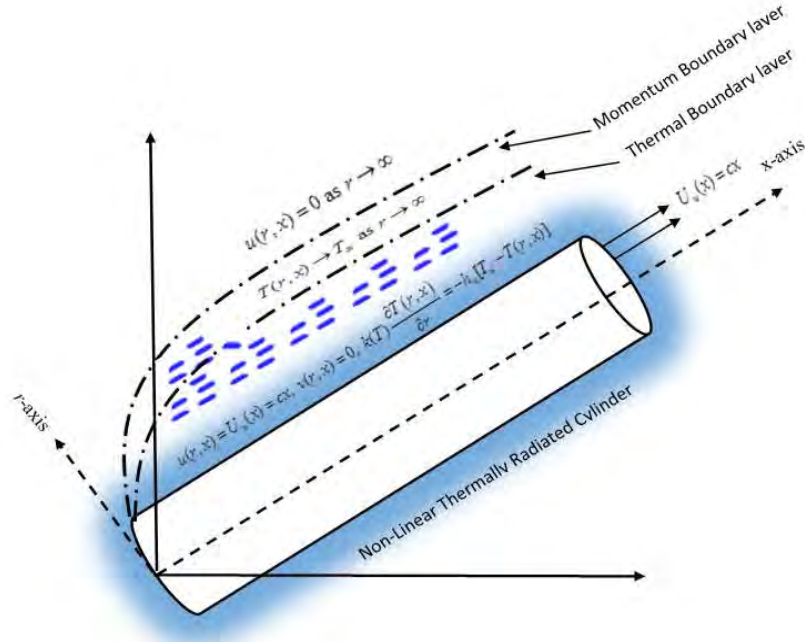
Fig.3.1: Geometry of the problem.

Where a is the higher shear rate viscosity, b is the power-law viscosity and n is flow behavior index generally known as power law index, Q_o is the heat source/sink coefficient, $T_w(x)$ and $T_\infty(x)$ are recommended surface and ambient temperature respectively. After applying Rosseland approximation, the nonlinear radiative heat flux q_r is defined as

$$q_r=-\frac{4\sigma}{3k_m}\frac{\partial T^4}{\partial r}=-\frac{16\sigma T^3}{3k_m}\frac{\partial T}{\partial r}, \qquad (3.4)$$

After inserting the Eq. (3.4) into Eq. (3.3), the energy equation takes the following form.

$$u\frac{\partial T}{\partial x}+v\frac{\partial T}{\partial y}=\frac{1}{r\rho c_p}\frac{\partial}{\partial r}\left(rk(T)\frac{\partial T}{\partial r}\right)+\frac{Q_0}{\rho c_p}(T-T_\infty)$$
$$+\frac{16\sigma}{3k_m\rho c_p}\left(T^3\frac{\partial^2 T}{\partial r^2}+3T^2\left(\frac{\partial T}{\partial r}\right)^2\right). \qquad (3.5)$$

The corresponding boundary conditions are given as

$$u(r,x) = U_w(x) = cx, \ v(r,x) = 0, \ k(T)\frac{\partial T(r,x)}{\partial r} = -h_w[T_w - T(r,x)] \text{ at } r = R$$

$$u(r,x) = 0, \ T(r,x) \to T_\infty \text{ as } r \to \infty, \tag{3.6}$$

stream function Ψ is defined as

$$u = \frac{1}{r}\frac{\partial \Psi}{\partial r}, v = \frac{-1}{r}\frac{\partial \Psi}{\partial x}. \tag{3.7}$$

To trace out the solution of Eqs. (3.1), (3.2) and (3.5) subject to the boundary conditions in Eq. (3.6), the following transformations are introduced.

$$\theta(\eta) = \frac{T - T_\infty}{T_w - T_\infty}, \ Re_b = \frac{\rho U^{2-n}x^n}{b}, \tag{3.8}$$

$$\eta = \frac{r^2 - R^2}{2Rx}Re_b^{\frac{1}{n+1}}, \psi = RxURe_b^{-\frac{1}{n+1}}f(\eta),$$

After applying above transformations in Eq. (3.8), Eq. (3.1) is identically satisfied, while Eqs. (3.2) and (3.5) take the following form,

$$A(1 + 2\gamma\eta)f''' + n(1 + 2\gamma\eta)^{\frac{n+1}{2}}(-f'')^{n-1}f''' + 2\gamma Af'' + \left(\frac{2n}{n+1}\right)ff'' - f'^2 \tag{3.9}$$

$$-(n+1)\gamma(1 + 2\gamma\eta)^{\frac{n-1}{2}}(-f'')^n + \lambda\theta\cos\alpha_t = 0,$$

$$\left(\left(1 + \frac{4}{3}R_d(1 + (\theta_T - 1)\theta)^3\right)(1 + 2\gamma\eta)\ \theta'\right)' + \left((1 + 2\eta\gamma)\varepsilon(\theta\theta'' + \theta'^2)\right) \tag{3.10}$$

$$+2\gamma\varepsilon\theta\theta' + \frac{2n}{n+1}\Pr\theta'f + \Pr\delta_H\theta = 0.$$

Associated modified boundary conditions are,

$$f(\eta) = 0, \ f'(\eta) = 1, \theta'(\eta) = -Bi(1 - \theta(\eta)) \text{ at } \eta = 0, \tag{3.11}$$

$$\lim_{\eta\to\infty} f'(\eta) = B, \ \lim_{\eta\to\infty} \theta(\eta) = 0,$$

where $\Pr, R_d, \gamma, A, \theta_T, \delta_H, Bi, \varepsilon$ and λ are defined as:

$$\Pr = \frac{xU}{\alpha_\infty Re_b^{\frac{2}{n+1}}}, R_d = \frac{16\sigma T_\infty^3}{3k_m}, \gamma = \frac{x}{RRe_b^{\frac{1}{n+1}}}, A = \frac{Re_b^{\frac{2}{n+1}}}{Re_a}, \tag{3.12}$$

$$\theta_T = \frac{T_w}{T_\infty} > 0, \ \delta_H = \frac{xQ_0}{U_w \rho c_p}, \ \text{Bi} = \frac{h_w}{k_m} xRe_b^{\frac{-1}{n+1}}, \lambda = \frac{g\beta x(T_w - T_\infty)}{U^2}.$$

Here, $Re_a = \frac{\rho Ux}{a}$ and $Re_b = \frac{\rho U^{2-n} x^n}{b}$ are local Reynold's numbers for viscous and power-law fluids, respectively. Further, it is required to discuss the physical quantities of interest such as surface drag force coefficient and temperature gradient coefficient, which are defined as

$$C_{fx} = \frac{\tau_w}{\frac{1}{2}\rho U_w^2}, \ Nu_x = \frac{xq_w}{k(T)(T_p - T_\infty)}, \quad (3.13)$$

where $\tau_w = b(-1)^{n+1}\left(\frac{\partial u}{\partial r}\right)^n_{r=R} + a\left(\frac{\partial u}{\partial r}\right)_{r=R}$ and $q_w = -k(T)\left(\frac{\partial T}{\partial r}\right)_{r=R}.$ $\quad (3.14)$

After simplification, the dimensionless form of surface drag force coefficient and surface heat flux coefficient is

$$\frac{1}{2}\left(C_{fx}Re_b^{\frac{1}{n+1}}\right) = (-1)^n(f''(0))^n + Af''(0), \quad Nu_x Re_b^{\frac{-1}{n+1}} = -\theta'(0). \quad (3.15)$$

3.2 Computational algorithm

Eqs. $(3.9) - (3.10)$ subject to boundary condition in Eqs.(3.11) are cracked numerically by using shooting method in conjunction with R-K-Fehlberg integration scheme. (Mention in chapter 1)

3.3 Results validation description

Fluid model given in Eqs. $(3.9) - (3.10)$ with boundary conditions Eq. (3.11) in the absence of Sisko parameter, mixed convection parameter, convective heat transfer, heat generation/absorption parameter, non-linear thermal radiation parameter and keeping flow behavior index $n = 1$, one can write as

$$(1 + 2\gamma\eta)f''' + 2\gamma f'' + ff'' - f'^2 = 0, \quad (3.16)$$

$$(1 + 2\gamma\eta)(\theta'' + \varepsilon(\theta\theta'' + \theta'^2)) + 2\gamma(1 + \varepsilon\theta)\theta' + \text{Pr} f\theta' = 0, \quad (3.17)$$

and corresponding end point conditions reduces to

$$f(\eta) = 0, f'(\eta) = 0, \theta(\eta) = 1, \text{ at } \eta = 0, \tag{3.18}$$
$$f'(\eta) \to 0, \theta(\eta) \to 0. \text{ as } \eta \to \infty.$$

Eqs. (3.22) − (3.24) is the mathematical modelling of the physical system, which were already discussed by Rangi et al. [51] (see Fig. 3.2). Fig. 3.3 shows the bar graph, which is constructed to compare the results of the present work with those of Rangi et al. [51]. An excellent match is noticed, which confirm the validity of the computational procedure.
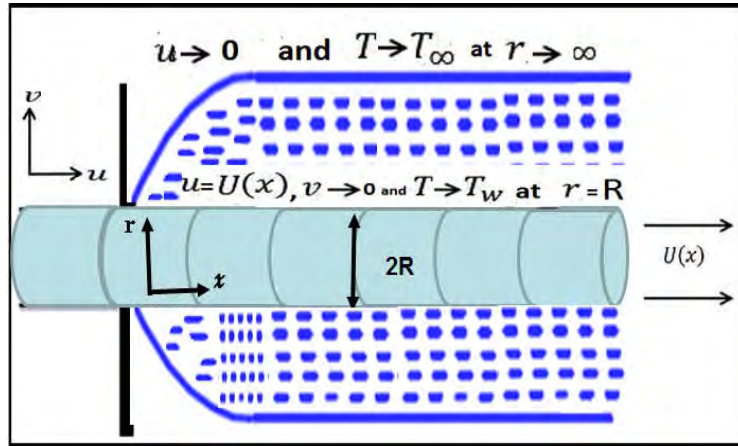
Fig. 3.2: Geometry of the problem of Rangi et al. [51]
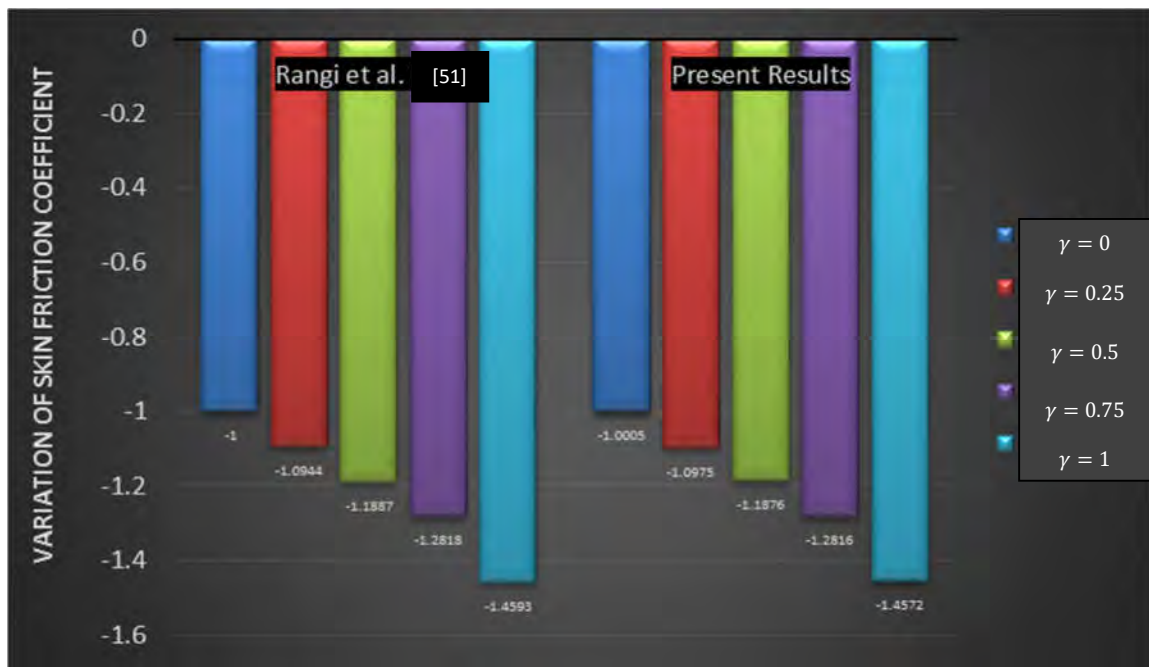
Fig. 3.3: Bar Graph for comparative values of wall shear stress coefficient for dissimilar values of curvature factor γ.

52

3.4 Physical and graphical outcomes

An inclusive study of the computed results by varying concerned pertinent flow parameters on velocity and temperature profiles has been presented here. Moreover, the physical outcomes of both surface drag force coefficient and surface heat flux coefficient are comprehensively discussed in both graphical and tabular forms. **Fig.** 3.1 indicates the physical configuration of the problem while **Fig.** 3.2 shows the flow chart of the shooting method. **Fig.** 3.3 shows the geometry of the flow problem discussed by Rangi et al. [55]. **Figs.** $3.4 - 3.12$ presents the effect of the embedded dimensionless parameters, such as Sisko parameter A, buoyancy assistive parameter λ, curvature parameter γ, Prandtl number Pr, variable thermal conductivity parameter ϵ, heat generation/absorbtion parameter δ_H, angle of inclination α_t, non-linear thermal radiation parameter R_d, and temperature ratio parameter θ_T on velocity and temperature profiles. Also, in **Figs.** $3.13 - 3.17$ the effects of embedded parameters on surface drag force coefficient and surface heat flux coefficient are presented.
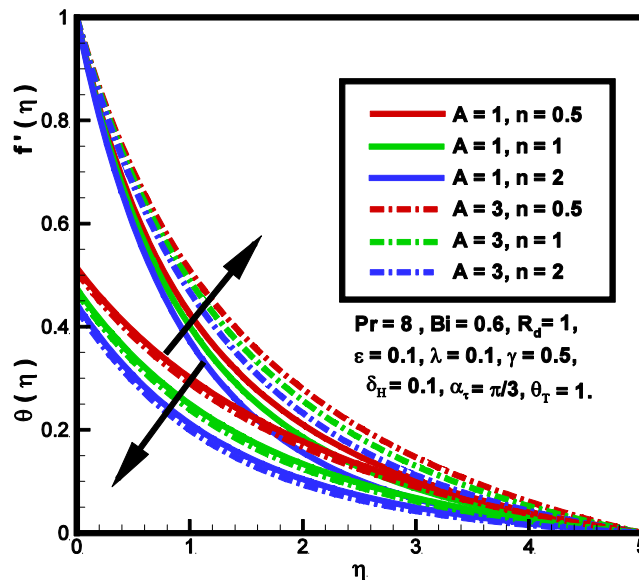
Fig. 3.4: Variations of A and n on $\theta(\eta), f'(\eta)$.
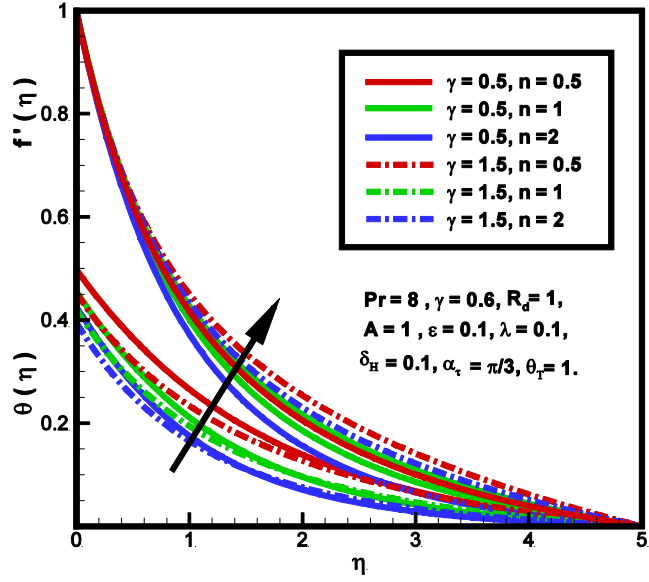
Fig. 3.5: Variations of γ and n on $\theta(\eta), f'(\eta)$.
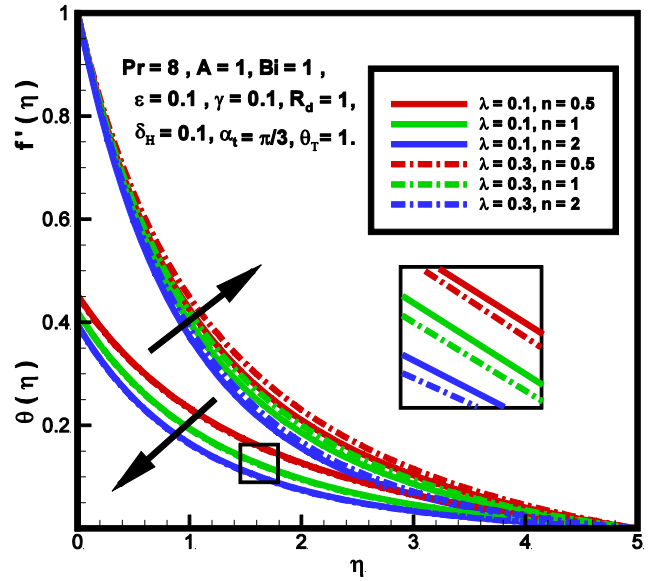
Fig. 3.6: Variations of λ and n on $\theta(\eta), f'(\eta)$.
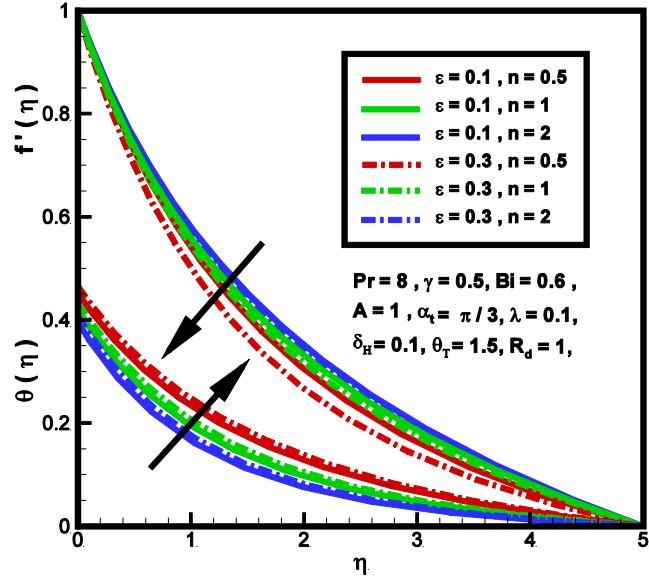
Fig. 3.7: Variations of ε and n on $\theta(\eta), f'(\eta)$.
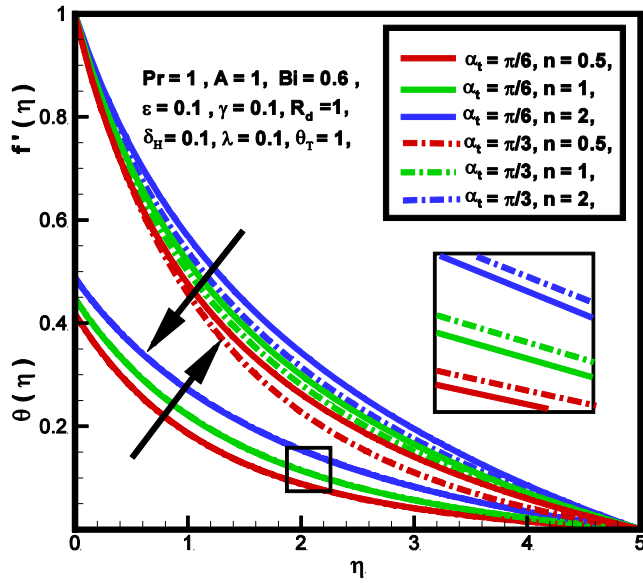
Fig. 3.8: Variations of α_t and n on $\theta(\eta), f'(\eta)$.
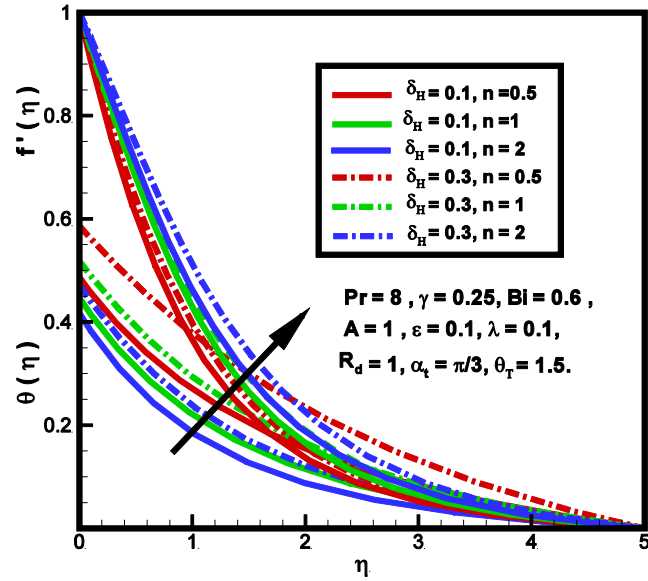
Fig. 3.9: Variations of δ_H and n on $\theta(\eta), f'(\eta)$.
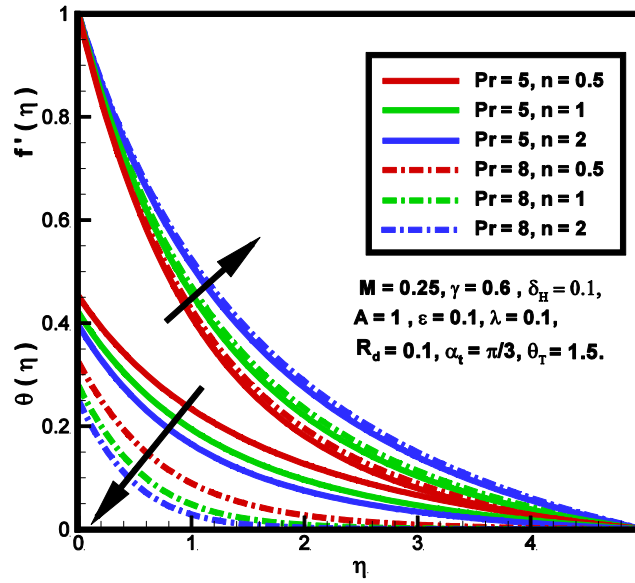
Fig. 3.10: Variations of Pr and n on $\theta(\eta), f'(\eta)$.
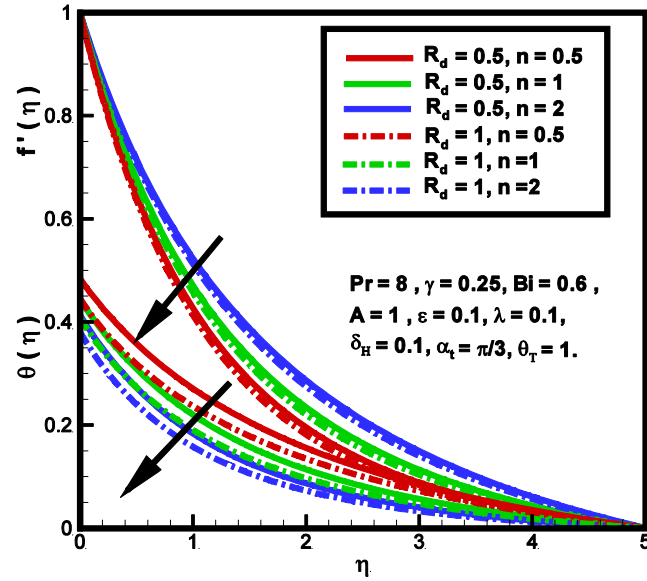
Fig. 3.11: Variations of R_d and n on $\theta(\eta), f'(\eta)$.
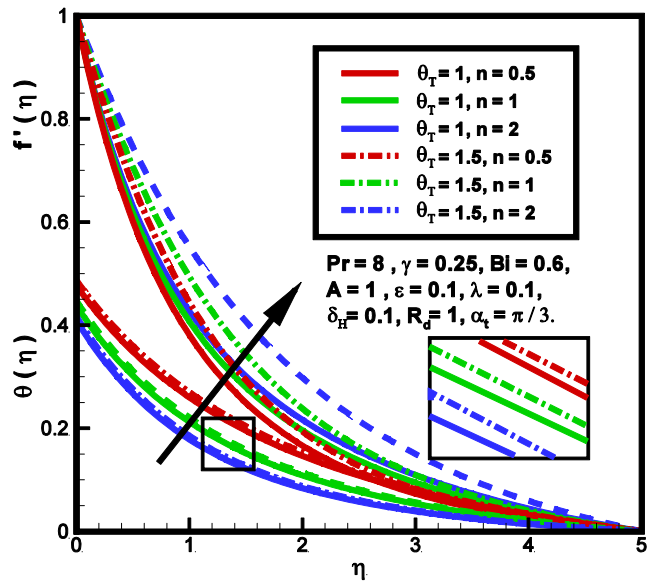
Fig. 3.12: Variations of θ_T and n on $\theta(\eta), f'(\eta)$.
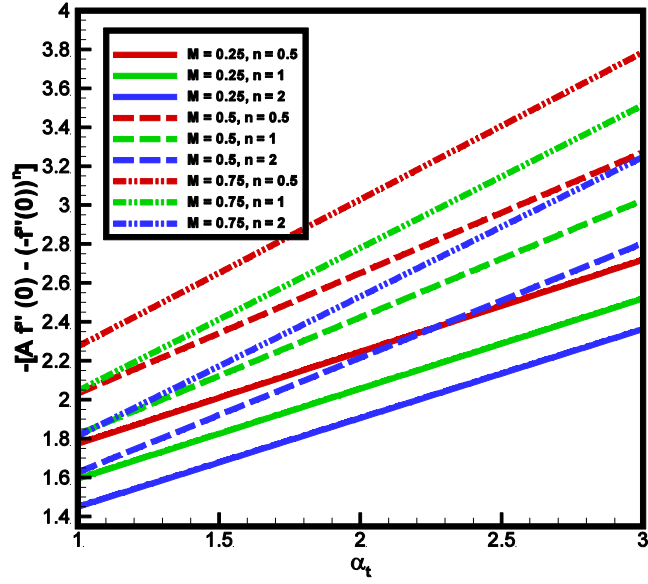
Fig. 3.13: Variations of α_t, M and n on the skin friction coefficient.
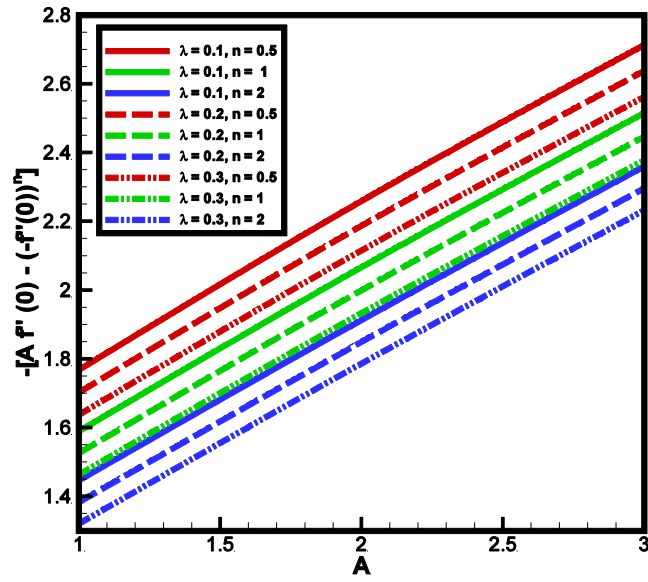
Fig. 3.14: Variations of λ, A and n on the skin friction coefficient.
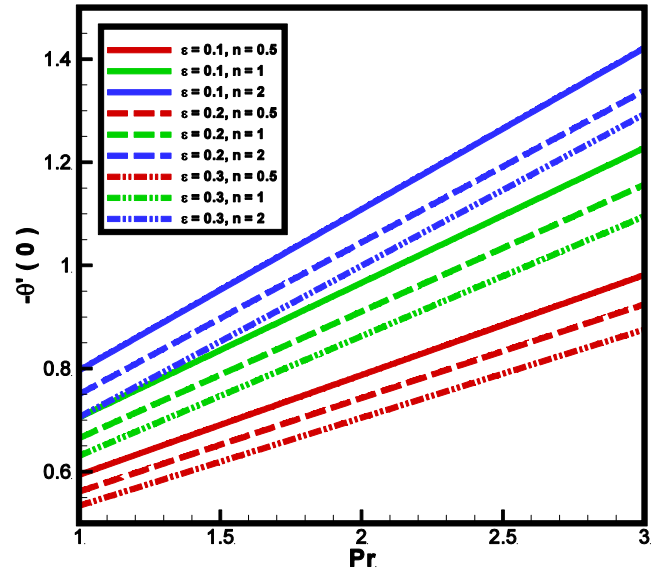
Fig. 3.15: Variations of $\Pr, \varepsilon$ and n on the locl Nusselt number.
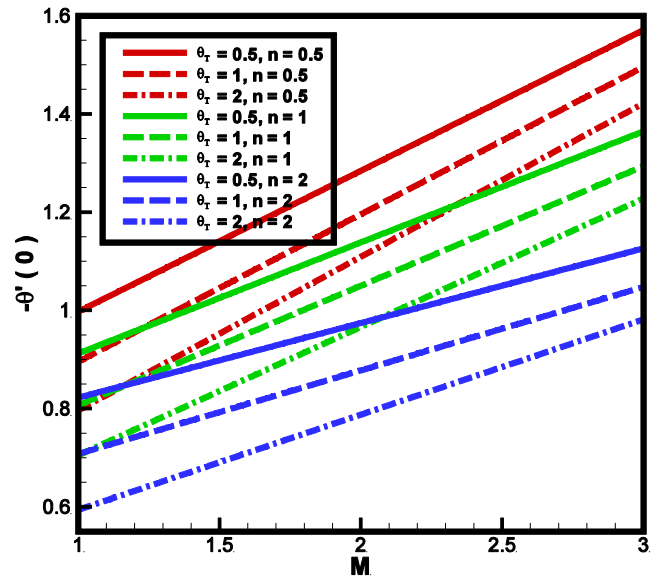
Fig. 3.16: Variations of θ_T, M and n on the local Nusselt number.
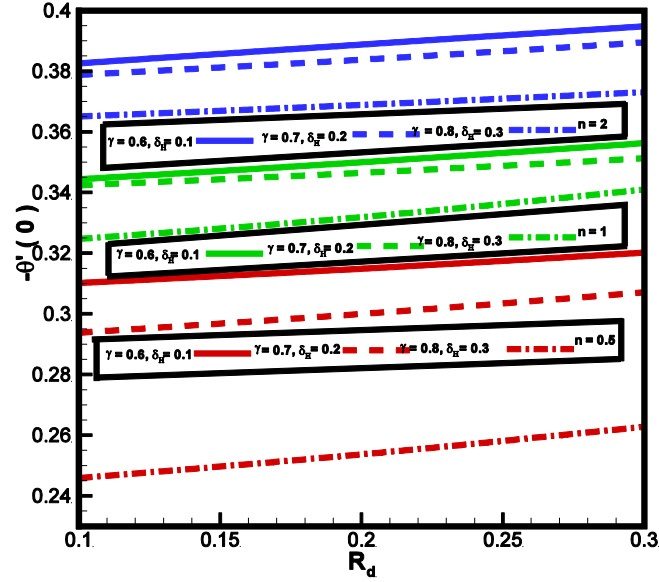
Fig. 3.17: Variations of R_d, δ_H, γ and n on the local Nusselt number.

Fig. 3.4 describes the behavior of temperature and velocity profiles for A and *n.* It is noticed $n > 0$ leads to decline in the momentum profile and the corresponding BL thickness. Since we are managing Sisko fluid, which is a blend of viscous and non-Newtonian fluids, (both shear thinning to shear thickening in nature). As viscosity of shear thickening fluids is higher than Newtonian and shear thinning fluids, hence *n* decreases velocity profile. Further, it is clearly shown, from the figure that by increasing material parameter the velocity profile increases, because by increasing *A* the inertial forces of fluid increases, which causes a decrease in viscous forces. But it has opposite effect on temperature profile, i.e., it reduces the temperature profile. **Fig.** 3.5 reveals the joint inspiration of γ and n on both velocity and temperature profiles. This graph shows that fluid velocity and temperature increases with an increase in γ, while *n* has an opposite effect on it. As far as velocity profile is concerned, these curves reveal that the velocity profile decreases by increasing values of $n.$ This happens because, when the behavior of the fluid changes from shear thinning to shear thickening, it becomes more compact and denser as a result, the velocity and temperature curves turns out to be decreasing in nature. **Fig.** 3.6 shows the effect of λ on both velocity and temperature profiles. It is perceived that growth in λ

causes an escalation in the velocity profile. Because positive values of λ can make the increasing convection current as a result velocity profile increase. **Fig.** 3.6 also represents the influence of λ ($\lambda > 0$ corresponds to assisting flow) on temperature profile. For $\lambda > 0$ produces a reasonable drop in thermal BL thickness, as a result temperature profile decrease. **Fig.** 3.7 reflects inciting nature of energy profile and decline velocity profile for $\epsilon > 0$. Physically when we increase the thermal conductivity parameter ϵ, fluid offers more conductance, due to this the transfer of heat increases, ultimately temperature enhances but opposite trend is notice for velocity profile. **Fig.** 3.8 shows the pivotal behavior of α_t on both momentum and energy profiles. It is noted that by enlarging the α_t momentum profile decreases whereas energy profile increases. **Fig.** 3.9 shows the impact of δ_H on both momentum and energy distributions. It is noticed that for $\delta_H > 0$ significant amount of heat is produced, which enhances the movement of fluid and hence the fluid velocity increases. Also, enhancement in the velocity distribution gives rise to average kinetic energy; ultimately, the temperature profiles increase. **Fig.** 3.10 is designed to see the impact of Pr on dimensionless temperature and velocity profiles for changing n. It is noticed that by enlarging Pr, the thermal BL thickness becomes thinner, which causes a decline in temperature profile and rise in velocity profile. **Fig.** 3.11 demonstrate the influence of R_d on both momentum and energy profiles for different values of n. From these curves, both velocity and temperature decrease against increasing values of R_d. **Fig.** 3.12 illustrates the nature of momentum and energy distributions versus θ_T, and n. For $\theta_T > 0$ the temperature difference between fluid and free stream reduces, consequently temperature and velocity of the fluid increases. **Fig.** 3.13 reveals the graphical representation of surface drag coefficient by varying parameters α_t, γ and n. It is witnessed that, for $\alpha_t > 0$ and $\gamma > 0$ the coefficient of surface drag force increases absolutely, whereas an inverse action is noted for increasing n. Since the γ has an inverse relation with the Reynolds number and the Reynolds number is inversely related to the skin friction coefficient, an increase in γ causes dropdown in the Reynolds number which ultimately improves the values of surface drag force coefficient. Finally, the flow behavior index n decreases the surface drag coefficient because the nature of the fluid changes. **Fig.** 3.14 shows the graphical interpretation of surface drag coefficient for λ, A and n. It is evident that by an increasing λ, the surface drag force decreases, because an increase in λ

strengthens the buoyancy force and decreases the viscous force, which alternatively reduces the surface drag force. **Fig.** 3.15 indicates the impacts of ε, Pr and n on surface heat flux. This graph reveals that temperature gradient coefficient increases for higher values of Pr and n while opposite trends is noted for ε. **Fig.** 3.16 shows the graphical interpretation of θ_T, γ, and n on the temperature gradient coefficient. It is evident that by increasing the γ, temperature gradient coefficient increases. The reason behind is that with the increase in γ, the temperature near the surface of cylinder decreases, thus thermal boundary layer becomes thin, which causes enhancement in the temperature gradient. From this figure, it is also shown that, increasing both temperature ratio parameter θ_T and flow behavior index n, the local Nusselt number increases. **Fig.** 3.17 shows the graphical behavior of R_d, δ_H, Bi and n on surface heat flux**.**

Table 3.1: Numerical variation of $\frac{1}{2}C_{fx}\mathrm{Re}_b^{\frac{1}{n+1}}$ for different values of A, M, λ and n.

A	M	λ	$n = 0.5,$ $f''(0)$	$n = 1,$ $f''(0)$	$n = 2,$ $f''(0)$
1	0.25	0.1	-1.7676	-1.5892	-1.4462
2	-	-	-2.2589	-2.0663	-1.9127
3	-	-	-2.7130	-2.5151	-2.3598
1	0.25	-	-1.7676	-1.5892	-1.4462
-	0.5	-	-2.0265	-1.8178	-1.6256
-	0.75	-	-2.2680	-2.0428	-1.8135
-	0.25	0.1	-1.7676	-1.5892	-1.4462
-	-	0.2	-1.7019	-1.5255	-1.3824
-	-	0.3	-1.6369	-1.4627	-1.3198

Table 3.2: Numeric values of $Nu_x \mathrm{Re}_b^{\frac{1}{n+1}}$ for increasing values of Pr, M, ϵ and n.

Pr	M	ϵ	$n = 0.5$ $-\theta(0)$	$n = 1$ $-\theta(0)$	$n = 2$ $-\theta(0)$
1	0.25	0.1	0.5903	0.6959	0.7849
2	-	-	0.7947	0.9825	1.1319
3	-	-	0.9781	1.2196	1.4101
1	0.25	-	0.5903	0.6969	0.7849
-	0.5	-	0.7064	0.8021	0.8871
-	0.75	-	0.8214	0.9095	0.9914
-	0.25	0.1	0.5903	0.6969	0.7849
-	-	0.2	0.5584	0.6576	0.7395
-	-	0.3	0.5312	0.6239	0.7006

Table 3.3: Effect of R_d, δ_H, γ, and n on $Nu_x \mathrm{Re}_b^{\frac{1}{n+1}}$.

R_d	δ_H	γ	$n = 0.5$ $-\theta(0)$	$n = 1$ $-\theta(0)$	$n = 2$ $-\theta(0)$
0.1	0.1	0.6	0.3102	0.3376	0.3651
0.2	-	-	0.3149	0.3424	0.3689
0.3	-	-	0.3202	0.3513	0.3731
0.1	0.1	-	0.3102	0.3424	0.3651
-	0.2	-	0.2929	0.3367	0.3645
-	0.3	-	0.2400	0.3075	0.3456
-	-0.1	-	0.3113	0.3343	0.3601
-	-0.2	-	0.3734	0.3954	0.4238
-	-0.3	-	0.4052	0.4312	0.4815
-	0.1	0.6	0.3102	0.3424	0.3731
-	-	0.7	0.3263	0.3595	0.3904
-	-	0.8	0.3534	0.3968	0.4192

Table 3.1 shows the outcomes of embedded physical parameters on the wall shear stress coefficient. This table confirms that by enlarging the values of A and γ, the wall shear stress coefficient increases but it possesses opposite behavior towards λ and n. **Table** 3.2 displays numerical variation in surface heat flux and for γ, Pr, n and ε. It is reflected from the tables that for higher values of Pr and n, coefficient surface heat flux increases, while it decreases by increasing the variable thermal conductivity parameter ε. **Table** 3.3 displays the effect of R_d, δ_H, Bi and n on surface heat flux. It is witnessed that, for positive values of R_d, Bi, and n the magnitude of the temperature gradient coefficient increases.

3.5 Conclusion

A computational is developed to investigate the mixed convection and non-linear radiation effects on the Sisko fluid flow over an inclined stretching cylinder in the presence of variable thermal conductivity and convective boundary conditions. Impact of embedded physical parameters on momentum as well as energy profiles are discussed in detailed. The main findings of present analysis are itemized as follows:

- Both velocity and temperature distributions show an increasing behavior against the thermal radiation parameters.
- The velocity profile is an increasing function of mixed convection parameter, while the temperature profile shows an opposite behavior against it.
- A remarkable increment is noted in the velocity profile for positive values of flow behavior index, material, and curvature parameters.
- In the presence of non-linear radiation, a significant enhancement in temperature is observed for the thermal conductivity parameter, while it shows opposite trend towards the Prandtl number.
- The coefficient of skin friction increases against positive values of curvature and material parameters, while it shows a decreasing behavior against mixed convection and power-law index.
- The surface heat flux increases for γ, Pr and n, but reduces against ε.

Chapter 4

Numerical investigation of MHD Prandtl melted fluid flow towards cylindrical Surface: Comprehensive outcomes

Present study is included to encounter the mathematical structure of Prandtl fluid flow over an inclined stretched cylinder. Modelling of this newly suggested model is demonstrated in three different ways. Momentum equation for concerned model is formed under the role of an induced Lorentz field, whereas the thermal and mass transport mechanisms admit the role of heat generation/absorption process and chemical reaction phenomenon. For more practical and schematic assessment of present exertion, the field expressions are described mathematically in terms of PDE's. The obtained complex differential system is transformed into ODE's by means of suitable transformations. Improved numerical simulation is performed by way of Cash and Carp method to anticipate the pattern of thermo-physical distribution towards an existing involved constraint.

4.1 Mathematical formulation

4.1.1 Flow field description

The momentum equation for present problem can be written as:

$$\rho \frac{dV}{dt} = \nabla \cdot \boldsymbol{T} + J \times B, \tag{4.1}$$

where V, J, B, and $\boldsymbol{T}$ are defined as follows:

$$V = [v(x,r), 0, u(x,r)], \ J = \sigma(V \times B), \ B = B_0 + b, \ T = -pI + S. \tag{4.2}$$

Stress tensor for Prandtl fluid is given as:

$$S = \left(\frac{P}{\dot{\gamma}} \arcsin\left(\frac{1}{c}\dot{\gamma}\right)\right) A_1, \tag{4.3}$$

The physical regime of the current study is presented in **Fig**. 4.1. An incompressible, steady flow of hydromagnetic Prandtl fluid flow towards a linearly varying inclined stretching

cylinder is considered. The velocity components along horizontal direction is u and along vertical direction is v. The cylinder is stretched along the horizontal direction with linear velocity. It is assumed that the cylinder makes an angle α_t with the horizontal, and exposed to uniform orthogonal magnetic field B_0, where B_0 is a constant related to magnetic field strength, it is also assumed that $T_\infty > T_m$ and $T_s < T_m$.
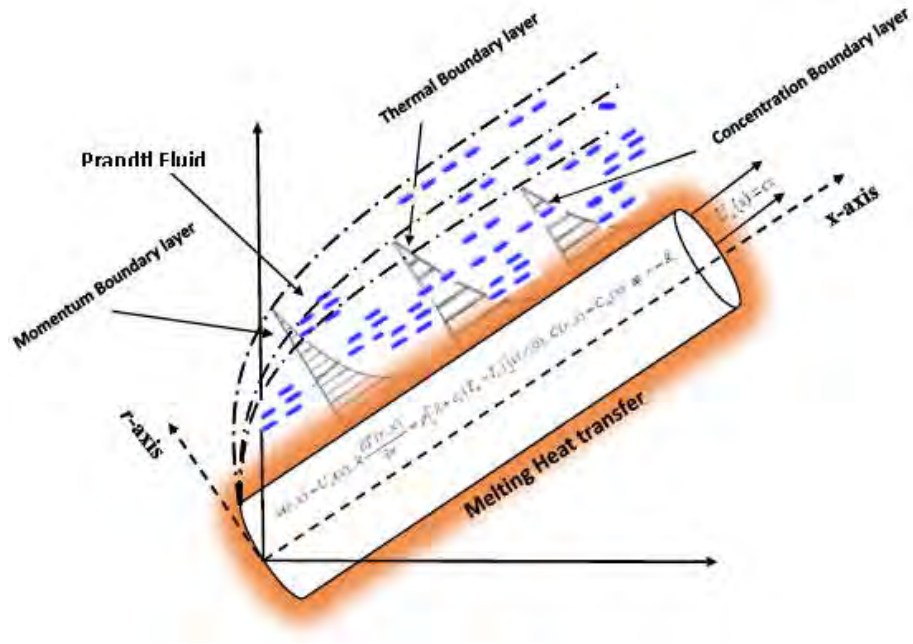
Fig. 4.1: Geometry of the problem.

After applying boundary layer approximation, governing equations takes the form as:

$$\frac{\partial(ru)}{\partial x} + \frac{\partial(rv)}{\partial r} = 0, \tag{4.4}$$

$$u\frac{\partial u}{\partial x} + v\frac{\partial u}{\partial r} = \frac{A}{\rho c}\frac{\partial^2 u}{\partial r^2} + \frac{A}{2\rho c^3}\left(\frac{\partial u}{\partial r}\right)^2\frac{\partial^2 u}{\partial r^2} + \frac{A}{r\rho c}\frac{\partial u}{\partial r} + \frac{A}{6r\rho c^3}\left(\frac{\partial u}{\partial r}\right)^3 - \sigma\frac{B_0^2}{\rho}$$
$$+ (g\beta_T(T - T_m) + g\beta_c(C - C_m))\cos\alpha_t, \tag{4.5}$$

subjected to boundary restrictions:

66

$$u(r,x) = U_w(x), \ k\frac{\partial T(r,x)}{\partial r} = \rho[\lambda + c_s(T_m - T_s)]v(r,0), \ \text{at} \ r = R,$$
$$u(r,x) \to 0, \ \text{as} \ r \to \infty. \tag{4.6}$$

By introducing stream function such that:

$$u = \frac{1}{r}\frac{\partial \Psi}{\partial r}, v = \frac{-1}{r}\frac{\partial \Psi}{\partial x}. \tag{4.7}$$

Eq. (4.5) can be transformed into non-linear ODE by using the following set of transformations:

$$\theta(\eta) = \frac{T - T_m}{T_\infty - T_m}, \phi(\eta) = \frac{C - C_m}{C_\infty - C_m}, \tag{4.8}$$

$$\eta = \frac{r^2 - R^2}{2Rx}\left(\frac{U}{vx}\right)^{\frac{1}{2}}, \Psi = (Uvx)^{\frac{1}{2}}Rf(\eta),$$

After applying above transformations, the continuity equation in Eq. (4.6) identically satisfied and the momentum Eq. (4.7) takes the dimensionless form as:

$$\alpha(1 + 2\gamma\eta)f''' + \alpha\beta(1 + 2\gamma\eta)^2 f''^2 f''' + \frac{4}{3}\gamma\alpha\beta(1 + 2\gamma\eta)(f'')^3 + 2\gamma\alpha f'' - (f')^2 \cdot$$
$$+\lambda(\theta + N\phi)\cos\alpha_t - M^2 f' = 0, \tag{4.9}$$

where the associated boundary conditions take the form:

$$f'(\eta) = 1, \text{Pr}f(\eta) + M_L\theta'(\eta) = 0 \ \text{at} \ \eta = 0, \tag{4.10}$$
$$f'(\eta) \to 0, \ \text{at} \ \eta \to \infty,$$

The involve dimensional parameter are defined as:

$$\alpha = \frac{A}{\mu c}, \beta = \frac{a^3 x^2}{2c^2 v}, \gamma = \frac{1}{R}\sqrt{\frac{vx}{U_w}}, \lambda = \frac{Gr}{Re^2}, N = \frac{Gc}{Gr}$$

$$M_f = \sqrt{\frac{\sigma x B_0^2}{\rho U}}, \text{Pr} = \frac{v}{\dot{\alpha}}, M_L = \frac{c_p(T_\infty - T_m)}{\lambda_1 + c_s(T_m - T_s)}, Gr = \frac{g\beta_T(T_\infty - T_m)}{v^2}, \tag{4.11}$$

$$Gc = \frac{g\beta_c(C_\infty - C_w)}{v^2}.$$

The wall drag factor can be defined as:

$$C_f = \frac{\tau_w}{\frac{1}{2}\rho(U_W)^2},$$

(4.12)

where τ_w is surface shear stress, expressed as,

$$\tau_w = \left[\frac{P}{c}\left(\frac{\partial u}{\partial r}\right) + \frac{P}{6c^3}\left(-\frac{\partial u}{\partial r}\right)^3\right]_{r=R},$$

(4.13)

dimensionless form of Eq. (4.12) is defined as:

$$\frac{1}{2}C_{fx}\text{Re}_x{}^{1/2} = Af''(0) + \beta(f''(0))^3.$$

(4.14)

4.1.2 Heat convection analysis

The energy equation for temperature is conducted with the exhibition of heat source/sink effect and melted heat transfer. Due to which magnetic interaction parameter becomes very small as a result there will be a very small amount of energy loss, so the viscous dissipation is neglected. After applying the usual boundary approximation, the energy equation reduces as follows:

$$u\frac{\partial T}{\partial x} + v\frac{\partial T}{\partial r} = \frac{\dot{\alpha}}{r}\frac{\partial}{\partial r}\left(r\frac{\partial T}{\partial r}\right) + \frac{Q_0(T - T_s)}{\rho c_p} + \frac{\sigma B_o^2}{\rho c_p}u^2,$$

(4.15)

The thermal endpoint conditions are given as:

$$T = T_m \text{ at } r = R, T \to T_\infty \text{ as } r \to \infty,$$

(4.16)

where T and T_m are temperature of fluid and melting surface, respectively. The condition associated to melting heat transfer is:

$$k\left(\frac{\partial T(r,x)}{\partial r}\right)_{r=R} = \rho[\lambda_L + c_s(T_m - T_s)]v(r,0).$$

(4.17)

here T_m is the melting temperature, λ_L is latent heat of the fluid, T_s is solid surface temperature, c_s is the heat capacity of the solid surface. To find the non-dimensional form

of Eq. (4.15) under boundary conditions in Eqs. (4.16) and (4.17) the following appropriate transformations are considered to reduce the PDEs into ODEs:

$$\eta = \frac{r^2 - R^2}{2R}\left(\frac{U}{vx}\right)^{\frac{1}{2}}, \ \theta(\eta) = \frac{T - T_m}{T_\infty - T_m}, \ \varphi(\eta) = \frac{C - C_m}{C_\infty - C_m}. \tag{4.18}$$

In view of above-defined variables, the Eq. (4.17) is defined as:

$$(1 + 2\gamma\eta)\,\theta'' + 2\gamma\theta' + \Pr(f\theta' + \delta_H\theta) = 0, \tag{4.19}$$

transformed boundary conditions are,

$$\theta(\eta) = 0 \text{ at } \eta = 0, \ \ \theta(\eta) = 1 \text{ at } \eta \to \infty. \tag{4.20}$$

where Pr and δ_H defined as:

$$\Pr = \frac{v}{\dot\alpha}, \delta_H = \frac{xQ_0}{\rho c_p U_w}, \tag{4.21}$$

In the present study, the physical quantity of interest with respect to heat convection is a local Nusselt number, which is given by,

$$Nu_x = \frac{xq_w}{k(T_\infty - T_m)}, q_w = -k\left(\frac{\partial T}{\partial r}\right)_{r=R}, \tag{4.22}$$

where q_w denotes surface heat flux. By incorporating Eq. (4.18) into Eq. (4.22) the reduced Nusselt number is obtained as:

$$Nu_x \mathrm{Re}_x^{-1/2} = -\theta'(\eta), \text{ at } \eta \to 0. \tag{4.23}$$

4.1.3 Mass diffusion analysis

The mass description is conceded in the occurrence of the chemical reaction. The boundary layer approximated equation of the mass diffusion is given by:

$$u\frac{\partial C}{\partial x} + v\frac{\partial C}{\partial r} = \frac{D}{r}\frac{\partial}{\partial r}\left(r\frac{\partial C}{\partial r}\right) - K(C - C_\infty), \tag{4.24}$$

where C, D, K and C_∞ are the concentration, mass diffusivity, chemical reaction rate constant and ambient concentration, respectively. The related boundary constrains are as follows:

$$C(r, x) = C_m \text{ at } r = R, \tag{4.25}$$

$$C(r, x) \to C_\infty \text{ as } r \to \infty.$$

Substitution of non-dimensionless concentration $\varphi(\eta) = \frac{C - C_m}{C_\infty - C_m}$ into Eq. (4.24), we obtain:

$$(1 + 2\gamma\eta)\,\phi'' + 2\gamma\phi' + Sc(f\phi' - \delta_c\phi) = 0, \tag{4.26}$$

the corresponding boundary conditions in Eq. (4.25) takes the form:

$$\phi(\eta) = 0 \text{ at } \eta = 0, \; \phi(\eta) = 1 \text{ at } \eta \to \infty, \tag{4.27}$$

where Sc is Schmidt number, δ_c is chemical reaction parameter, which are defined as:

$$Sc = \frac{\nu}{D}, \delta_c = \frac{Kx}{U_w}. \tag{4.28}$$

The important physical quantity with respect to mass diffusion is mass flux coefficient, defined as:

$$Sh_x = \frac{x j_x}{D(C_\infty - C_m)}, j_w = -D\left(\frac{\partial C}{\partial r}\right). \tag{4.29}$$

In dimensionless form, the Sherwood number is expressed as:

$$Sh_x Re_x^{-1/2} = -C'(\eta), \text{ at } \eta \to 0. \tag{4.30}$$

4.2 Computational Algorithm

The resulted ordinary differential Eqs. (4.9), (4.19) and (4.26) with the accompanied boundary restrictions (4.10), (4.20) and (4.27) are solved with Runge-Kutta-Fehlberg (R.K.F) scheme. (Mentioned in Chapter 1)

4.3 Physical and graphical outcomes

The present section provides comprehensive study of numerically calculated results and effect of all pertinent physical parameters on the momentum, energy, and concentration profiles. Furthermore, the surface drag force coefficient, the temperature gradient and surface mass flux coefficient are presented in the graphical and tabular form.

4.3.1 Nondimensional velocity profile

For detail analysis, results are given to carry out a parametric study showing the effects of the dimensionless parameters namely, Prandtl fluid parameter α, elastic parameter β, mixed convection parameter λ, concentration buoyancy parameter N, Prandtl number Pr, magnetic field parameter M, and melting parameter M_L on velocity profile.
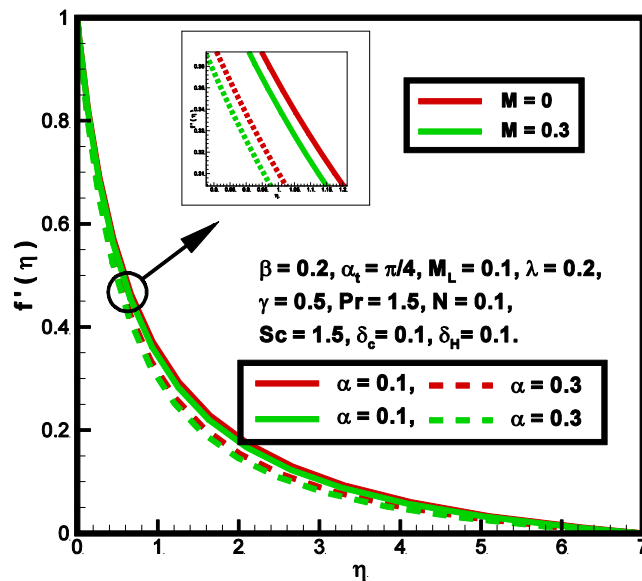
Fig. 4.2: Impact of α on $f'(\eta)$ in absence/presence of M.
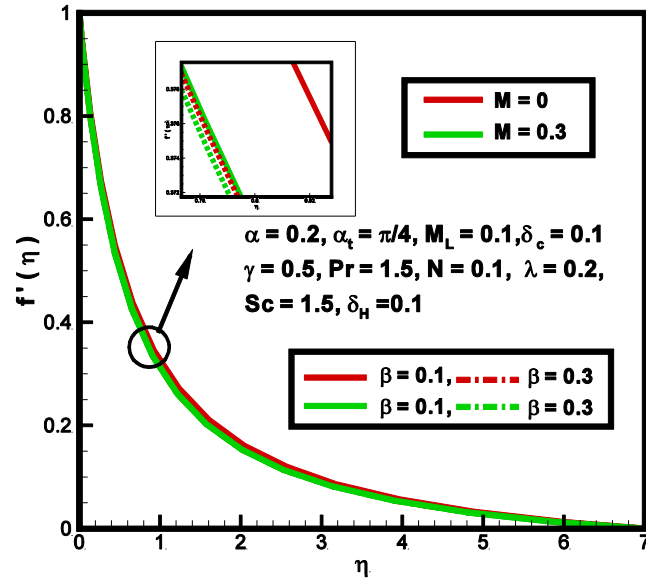
Fig. 4.3: Impact of β on $f'(\eta)$ in absence/presence of M.
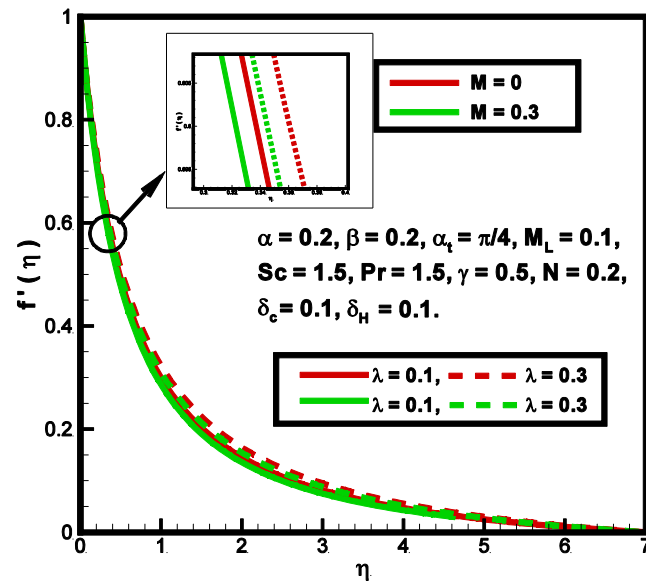
Fig. 4.4: Impact of λ on $f'(\eta)$ in absence/presence of M.
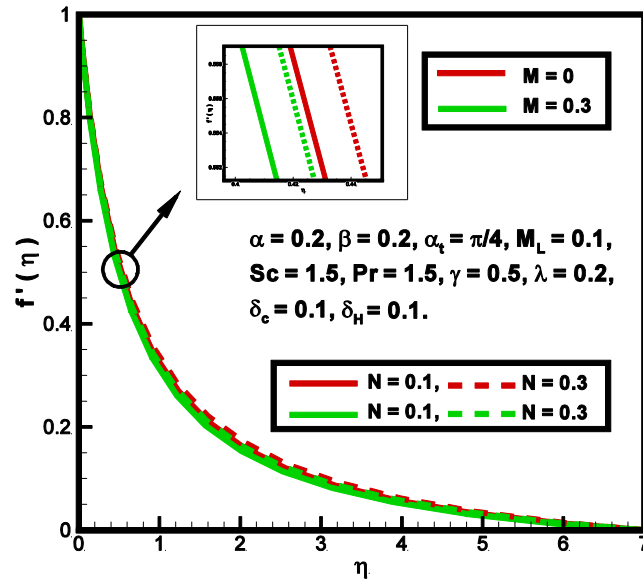
Fig. 4.5: Impact of N on $f'(\eta)$ in absence/presence of M
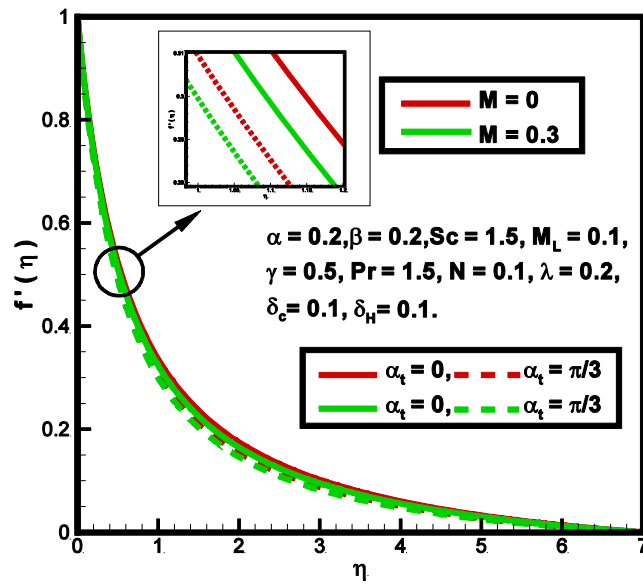
Fig. 4.6: Impact of α_t on $f'(\eta)$ in absence/presence of M.
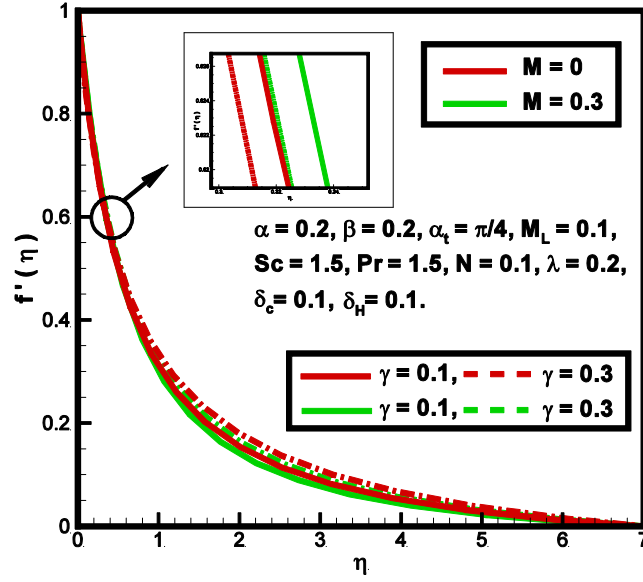
Fig. 4.7: Impact of γ on $f'(\eta)$ in absence/presence of M.
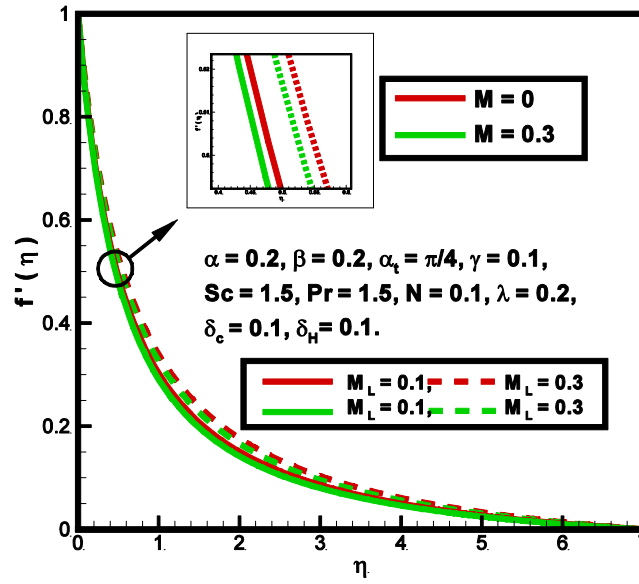
Fig. 4.8: Effect of M_L on $f'(\eta)$ in absence/presence of M.

Figs. 4.2 and 4.3 depicts variation of α, and β, on velocity profile respectively in the absence/presence of M. Both graphs reveal that for $\alpha > 0$ and $\beta > 0$, the B.L thickness reduces irrespective of absence/presence of M, which results decrease in velocity profiles. **Figs.** 4.4 and 4.5 exhibits momentum profile for altering values of λ and N in absence/presence of M. Impact of λ on velocity profile is shown in **Fig.** 4.4. In the present case when $\lambda > 0$ buoyancy force acts in the direction of mainstream and fluid accelerates. Furthermore, N is the ratio of concentration to thermal buoyancy forces so with an increment in the values of N the concentration buoyancy force increases, as a result velocity profile increase (see Fig. 4.5). **Fig.** 4.6 is plotted zero and non-zero M to see the impact of α_t on velocity distribution. It is perceived that by increasing angle of inclination gravity factor decreases, consequently velocity profile decreases regardless of the zero and non-zero M. Moreover, increase in α_t causes reduction in buoyancy forces which is also the reason for reduction of velocity profile. Since increase in M leads to an increase the amount of Lorentz force. Which has the propensity to slow down the flow. Strong Lorentz forces yields more opposition to the momentum transport, thus higher values of M, causes decrease in hydrodynamics boundary layer thickness. **Fig.** 4.7 reveals that fluid velocity exceeds on increment of γ in the absence/presence of M. These curves prescribed that the velocity of the fluid disappears asymptotically. **Fig.** 4.8 specifies the velocity distribution for altering M_L. in the absence/presence of M. Regardless absence/presence of M, the velocity distribution rises for resign values of M_L. It is because, at the start of the melting process the surface under consideration is in solid state and the local source is at constant temperature, so initially heat conduction is the main cause of heat transfer due to absence of melting zone. After heating the analysed material near the heat source, one can find the formation of melting zone and melt begins to circulate in this zone. Such circulation leads to an increase in the molecular motion of the particles of the material and hence convection heat transfer starts to play his role as a result the melting heat transfer mounted the velocity profile.

4.3.2 Nondimensional temperature profile

The objective of the present section is to contemplate the impact of involved parameters like γ, Pr, M_L, and δ_H, on temperature distribution. **Fig.** 4.9 is developed for the physical interpretation of γ on temperature distribution in the absence/presence of M. It is noticed that the behaviour M and γ on temperature profile are same i.e., temperature and the corresponding thermal BL thickness increases as M and γ increases. This is on account of, γ parameter increases the surface heat transfer, as a result temperature distribution decreases near the skin of the cylinder, but it is responsible in the enhancement of the temperature profile away from the surface. On the other hand, presence of M reduces motion of the fluid particles, consequently, some amount of work is done which is converted into heat energy enhancing the temperature.
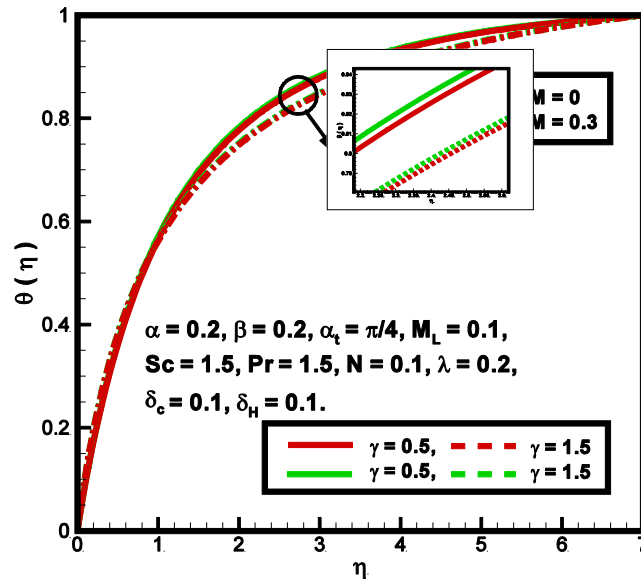
Fig. 4.9: Impact of γ on $\theta(\eta)$ in absence/presence of M.
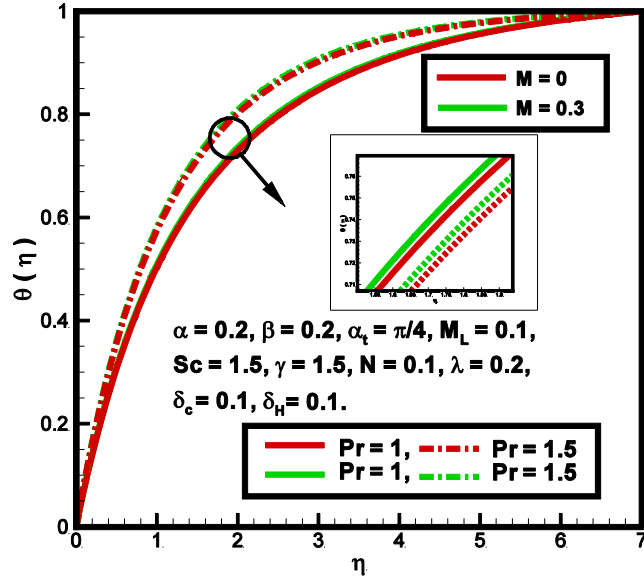
Fig. 4.10: Impact of Pr on $\theta(\eta)$ in absence/presence of M.
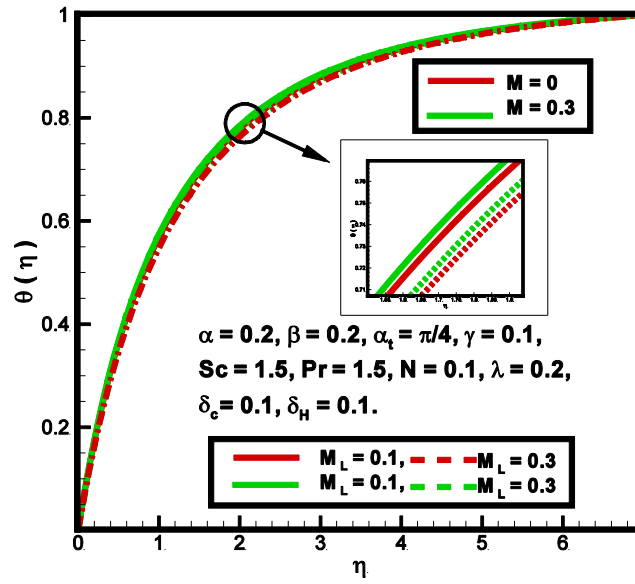
Fig. 4.11: Impact of M_L on $\theta(\eta)$ in absence/presence of M.
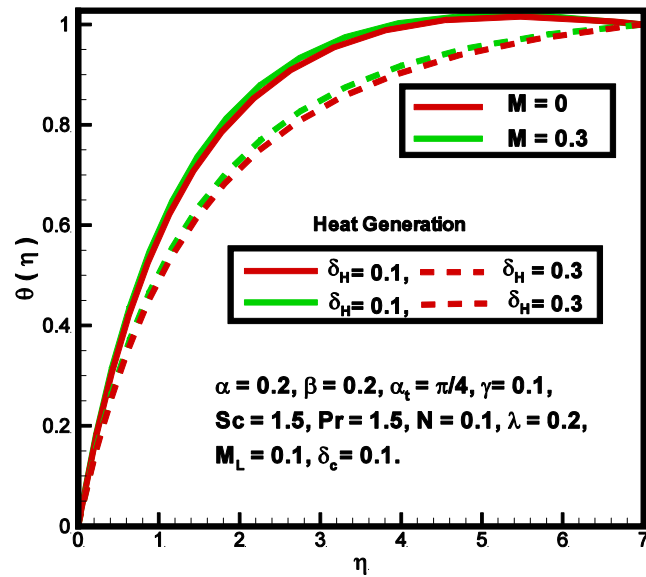
Fig. 4.12: Impact of δ_H on $\theta(\eta)$ in absence/presence of *M.*
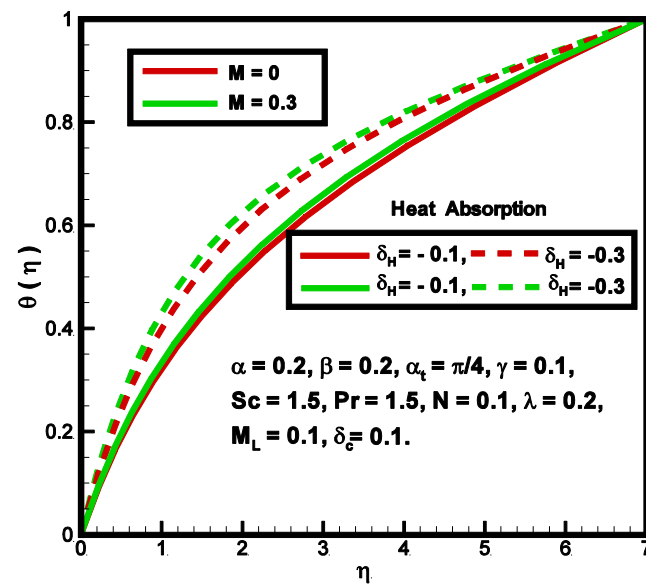
Fig. 4.13: Impact of δ_H on $\theta(\eta)$ in absence/presence of *M.*

Fig. 4.10 specifies the impact of Pr on temperature distribution for varying M. The graphical study depicts that behaviour of both M and Pr on temperature distribution are opposite. It is revealed that in absence of M and by upgrading the values of Pr, momentum diffusivity increases, and thermal diffusivity decreases, as a result, respective boundary layer thickness decreases which reduces the temperature profile. But in presence of M, fluid temperature increases. **Fig.** 4.11 exhibits the temperature distribution for distinct M_L. It is noted that temperature profile drops due to increasing values of M_L. Physically, $M_L > 0$ is reason for increase in the temperature of melting surface consequently temperature difference of melting surface and ambient temperature increases, which reduces the fluid temperature. But with the increase of M_L, thermal BL thickness increases. **Fig.** 4.12 and 4.13 illustrates the impact of heat absorption/generation parameter cases over temperature profiles with and without magnetic force. **Fig.** 4.12 reflects inciting nature of temperature profile in case of heat generation i.e., $\delta_H > 0$, while **Fig.** 4.13 revels restraining nature of temperature profile for heat absorption case i.e., $\delta_H < 0$. It is also evident that temperature enhancement can also control efficiently by adding heat absorption into the system as shown in **Fig.** 4.13.

4.3.3 Nondimensional concentration profile

In this section we have prepared various plots to examine different rheological features of the embedded parameter such as Schmidt number Sc and chemical reaction parameter δ_c on mass diffusion profile. **Fig.** 4.14 addresses about the conduct of Sc on concentration profile in absence/presence of M. It is perceived that, the solutal BL thickness decreases by growing Sc. Physically Sc is inversely related to mass diffusivity. So, by enlarging Sc will bring reduction in the solutal BL due to which concentration distribution decreases. **Fig.** 4.15 displays the concentration profile across the flow domain. It is evident that existence of destructive chemical reaction δ_c decreases the concentration profile and resulting thicker concentration boundary layer.
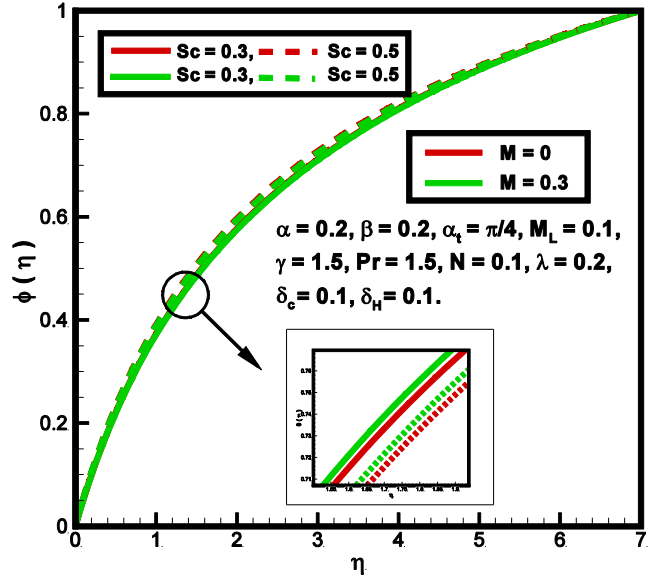
Fig. 4.14: Effect of Sc on $\phi(\eta)$ in absence/presence of M.
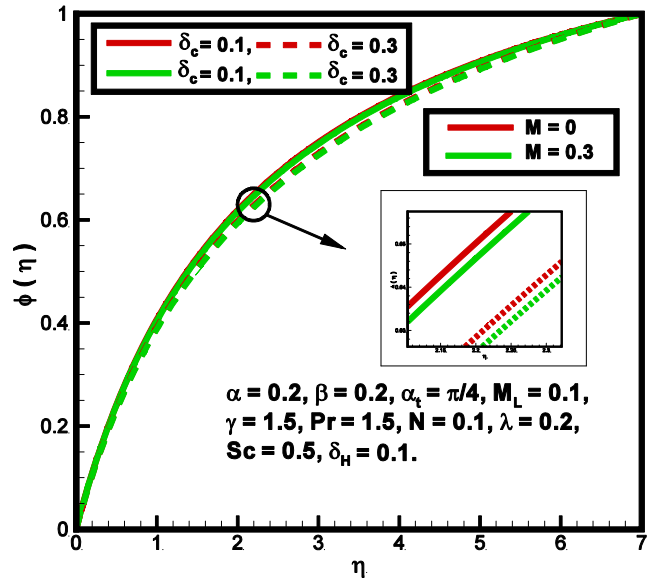
Fig. 4.15: Effect of δ_c on $\phi(\eta)$ in absence/presence of M.

Table 4.1: Numerical data of wall shear stress for $\alpha, \beta, \gamma, \lambda, N, \alpha_t, M$ and M_L when $\text{Pr} = 1.5, \delta_H = 0.1, Sc = 0.5$ and $\delta_c = 0.1$.

α	β	γ	λ	N	α_t	M	M_L	$\alpha f''(0) + \beta[f''(0)]^3$
1	0.2	0.5	0.1	0.1	$\pi/4$	0.1	0.2	-1.1896
2	-	-	-	-	-	-	-	-1.6996
3	-	-	-	-	-	-	-	-2.2155
1	0.2	-	-	-	-	-	-	-1.1896
-	0.4	-	-	-	-	-	-	-1.3138
-	0.5	-	-	-	-	-	-	-1.4201
-	0.2	0.5	-	-	-	-	-	-1.1896
-	-	1	-	-	-	-	-	-1.4651
-	-	1.5	-	-	-	-	-	-1.7481
-	-	0.5	0.1	-	-	-	-	-1.1896
-	-	-	0.3	-	-	-	-	-0.9688
-	-	-	0.5	-	-	-	-	-0.7872
-	-	-	0.1	0.1	-	-	-	-1.1896
-	-	-	-	0.3	-	-	-	-1.1752
-	-	-	-	0.5	-	-	-	-1.1610
-	-	-	-	0.1	$\pi/6$	-	-	-1.1811
-	-	-	-	-	$\pi/4$	-	-	-1.1896
-	-	-	-	-	$\pi/3$	-	-	-1.2386
-	-	-	-	-	$\pi/4$	0.1	-	-1.1896
-	-	-	-	-	-	0.3	-	-1.2253
-	-	-	-	-	-	0.7	-	-1.5328
-	-	-	-	-	-	0.1	0.2	-1.1896
-	-	-	-	-	-	-	0.4	-1.2711
							0.6	-1.3831

Table 4.2: Numerical data of surface heat flux coefficient for $\gamma, \text{Pr}, \delta_H$ and M_L when $\alpha = 1, \beta = 0.2, \lambda = 0.1, N = 0.1, \alpha_t = \frac{\pi}{4}, M = 0.1, Sc = 0.5,$ and $\delta_c = 0.1$.

γ	Pr	δ_H	M_L	$\theta'(0)$
0.5	1.5	0.1	0.2	1.1035
1	-	-	-	1.2223
1.5	-	-	-	1.3723
0.5	1.5	-	-	1.1035
-	3	-	-	1.5420
-	5	-	-	2.1173
-	1.5	0.1	-	1.1035
-	-	0.2	-	1.4441
-	-	0.3	-	1.9282
-	-	0.1	0.2	1.1035
-	-	-	0.4	1.4312
-	-	-	0.6	1.8115

Table 4.3: Numerical variation of Sherwood number for $\gamma, Sc,$ and δ_c when $\text{Pr} = 1.5, \alpha = 1, \beta = 0.2, \lambda = 0.1, N = 0.1, \alpha_t = \frac{\pi}{4}, M = 0.1, Sc = 0.5, M_L = 0.1$ and $\delta_H = 0.1$.

γ	Sc	δ_c	$-\phi'(0)$
0.5	0.5	0.1	0.5463
1	-	-	0.7934
1.5	-	-	0.9946
0.5	0.5	-	0.5463
-	1	-	0.6008
-	1.5	-	0.6458
-	0.5	0.1	0.5463
-	-	0.2	0.6042
-	-	0.3	0.6513

Table 4.1 is exhibited to explain the effects of $\alpha, \beta, \gamma, \lambda, N, \alpha_t, M$ and M_L on surface drag force coefficient. It is perceived that surface drag force coefficient increases for all positive values of $\alpha, \beta, \gamma, \lambda, N, \alpha_t, M$ and M_L but opposite behavior is noted for increase in λ and N. **Table** 4.2 is equipped to check the influence of involving parameters on coefficient of surface heat flux. It is manifested from the numeric values that coefficient of surface heat flux is increasing for all positive values of $\gamma, \text{Pr}, \delta_H$ and M_L. **Table** 4.3 depicts the variation in Sherwood number for change in the physical parameters γ, Sc and δ_c. It is noticed that the Sherwood number is decreasing function of γ, Sc and δ_c.

4.4 Conclusion

The obtained results are itemized as follows:

- The velocity distributions reflect an inciting attribute towards the melting parameter, curvature parameter and the mixed convection parameter.
- The velocity profile declines for the Prandtl fluid parameter, elastic parameter and an inclination.
- The fluid temperature reflects inciting nature towards the magnetic field parameter, curvature parameter and the melting parameter.
- In the absence of the magnetic field the temperature profile declines for Prandtl number but an opposite attitude is recorded when the magnetic field is considered.
- The concentration distributions shows decline attitude for both the Schmidt and chemical reaction parameter. This nature is preserved for both magnetized and non-magnetized cases.

Chapter 5

Numerical communication of chemically reactive species in MHD Prandtl nano-fluid flow towards stretching cylinder.

Magnetohydrodynamic Prandtl nanofluid flow induced by stretching cylindrical surface along with partial slip condition is studied numerically in this chapter. The flow field characteristics are elaborated in the presence/absence of chemical reaction phenomena. To be more specific, the obtained higher ordered equations are transformed into system of first order differential equations with the source of similarity transformation. A numerical algorithm is executed to find the solution of Prandtl nanofluid flow due to cylindrical stretching surface. The effect logs of engaged parameters are reported through graphical outcomes while the variations of physical quantities are discussed by way of tabular structure.

5.1 Mathematical formulation

Let us assume the 2D, incompressible, laminar, and steady boundary-layer electrically conducting Prandtl nanofluid towards a linearly stretching cylinder. The axial line of cylinder is assumed to be *x-axis* and radial direction perpendicular to cylinder axis is *r-axis*. Let u and v be the velocity components along x and r directions, respectively. The cylinder is stretched axially with linear velocity and exposed to uniform orthogonal magnetic field B_0. Furthermore, the generated magnetic field is very small in comparison with applied one due to low magnetic Reynolds number assumption as shown in **Fig.** 5.1.
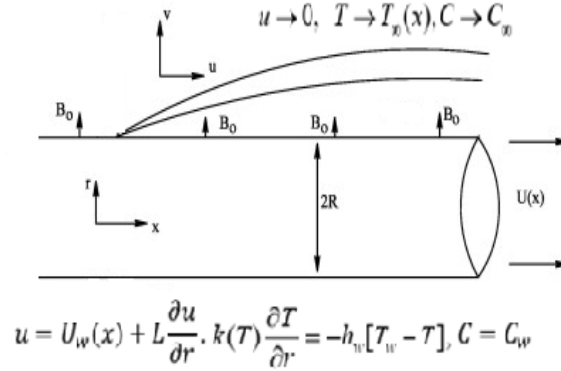
Fig. 5.1: Geometry of the problem.

In the non-existence of pressure gradient, and by means of usual BL approximations, the continuity, momentum, energy, and concentration equations are described as.

$$\frac{\partial(ru)}{\partial x} + \frac{\partial(rv)}{\partial r} = 0,$$

(5.1)

$$u\frac{\partial u}{\partial x} + v\frac{\partial u}{\partial r} = \frac{A}{\rho c}\frac{\partial^2 u}{\partial r^2} + \frac{A}{2\rho c^3}\left(\frac{\partial u}{\partial r}\right)^2\frac{\partial^2 u}{\partial r^2} + \frac{A}{r\rho c}\frac{\partial u}{\partial r} + \frac{A}{6r\rho c^3}\left(\frac{\partial u}{\partial r}\right)^3 - \sigma\frac{B_0^2}{\rho}u,$$

(5.2)

$$u\frac{\partial T}{\partial x} + v\frac{\partial T}{\partial r} = \frac{\dot{\alpha}}{r}\frac{\partial}{\partial r}\left(r\frac{\partial T}{\partial r}\right) + \tau D_B\left(\frac{\partial C}{\partial r}\frac{\partial T}{\partial r}\right) + \frac{\tau D_T}{T_\infty}\left(\frac{\partial T}{\partial r}\right)^2 + \frac{A}{c\rho c_p}\left(\frac{\partial u}{\partial r}\right)^2$$

$$+ \frac{A}{6c^3\rho c_p}\left(\frac{\partial u}{\partial r}\right)^3,$$

(5.3)

$$u\frac{\partial C}{\partial x} + v\frac{\partial C}{\partial r} = \frac{D_B}{r}\frac{\partial}{\partial r}\left(r\frac{\partial C}{\partial r}\right) + \frac{D_T}{rT_\infty}\frac{\partial}{\partial r}\left(r\frac{\partial T}{\partial r}\right) - K(C - C_\infty).$$

(5.4)

Subjected to the boundary conditions,

$$u = U_w(x) + L\frac{\partial u}{\partial r}, v = 0, k(T)\frac{\partial T}{\partial r} = -h_w[T_w - T], C = C_w \text{ at } r = R,$$

$$u \to 0, \ T \to T_\infty(x), C \to C_\infty \text{ as } r \to \infty.$$

(5.5)

In above σ is the electrical conductance, C_w is the volumetric fraction of nano-fluid at wall, and C_∞ is the ambient concentration, D_B is Brownian diffusion coefficient, D_T is the thermophoresis diffusion coefficient, K is chemical reaction rate constant, and h_w

represents the coefficient of heat transfer.

The stream function for fluid is defined as:

$$u = \frac{1}{r}\frac{\partial \Psi}{\partial r}, \quad v = \frac{-1}{r}\frac{\partial \Psi}{\partial x}. \tag{5.6}$$

The governing problem of flow configuration is transformed into dimensionless non-linear ODE's by using following set of transformations,

$$\theta(\eta) = \frac{T - T_\infty}{T_w - T_\infty}, \quad \phi(\eta) = \frac{C - C_\infty}{C_w - C_\infty},$$

$$\eta = \frac{r^2 - R^2}{2Rx}\left(\frac{U_w}{vx}\right)^{\frac{1}{2}}, \quad \Psi = (U_w vx)^{\frac{1}{2}} R f(\eta), \tag{5.7}$$

After applying the above transformations, obtained system in dimensionless form will be:

$$\alpha(1 + 2\gamma\eta)f''' + \alpha\beta(1 + 2\gamma\eta)^2 f''^2 f''' + \frac{4}{3}\gamma\alpha\beta(1 + 2\gamma\eta)\,(f'')^3 + 2\gamma\alpha f''$$
$$-(f')^2 + ff'' - M^2 f' = 0, \tag{5.8}$$

$$(1 + 2\gamma\eta)\,\theta'' + 2\gamma\theta' + \Pr f\theta' + \Pr(1 + 2\gamma\eta)\,(Nb\theta'\phi' + Nt\theta'^2) = 0, \tag{5.9}$$

$$(1 + 2\gamma\eta)\phi'' + 2\gamma\phi' + Le\Pr(f\phi' - \delta_c\phi) + \frac{Nt}{Nb}(2r\theta' + (1 + 2\gamma\eta)\theta'') = 0, \tag{5.10}$$

The corresponding end point conditions take the form.

$$\left.\begin{array}{l} f(\eta) = 0, \ f'(\eta) = 1 + \lambda f''(0), \text{ at } \eta = 0 \text{ and } f'(\eta) \to 0, \text{ at } \eta \to \infty, \\ \theta(\eta) = 1 \text{ at } \eta = 0 \text{ and } \theta'(\eta) = -Bi\big(1 - \theta(\eta)\big) \text{ as } \eta \to \infty, \\ \phi(\eta) = 1 \text{ at } \eta = 0 \text{ and } \phi(\eta) = 0 \text{ at } \eta \to \infty. \end{array}\right\} \tag{5.11}$$

The dimensionless involve parameters are defined as:

$$\left.\begin{array}{l} \alpha = \dfrac{A}{\mu c}, \beta = \dfrac{a^3 x^2}{2c^2 v}, \gamma = \dfrac{1}{R}\sqrt{\dfrac{vx}{U_w}}, Nb = \dfrac{\tau D_B (C_w - C_\infty)}{\rho c_p v}, \\[3mm] M_f = \sqrt{\dfrac{\sigma x B_0^2}{\rho U_w}}, \Pr = \dfrac{v}{\dot{\alpha}}, \mathrm{Re} = \dfrac{U_w x}{v}, \mathrm{Le} = \dfrac{\dot{\alpha}}{D_B}, Bi = \dfrac{h_w}{k}\sqrt{\dfrac{vx}{U_w}} \\[3mm] Nt = \dfrac{\tau D_T (T_w - T_\infty)}{T_\infty \rho c_p v}, \delta_c = \dfrac{Kx}{U_w}, \end{array}\right\} \tag{5.12}$$

The physical parameter defined as

$$C_{fx} = \frac{\tau_w}{\frac{1}{2}\rho U_w^2}, Nu_x = \frac{xq_w}{k(T_\infty - T_m)}, Sh_x = \frac{xj_w}{D(C_\infty - C_m)}. \tag{5.13}$$

Here τ_w and q_w are defined as:

$$\tau_w = \left[\frac{A}{C}\left(\frac{\partial u}{\partial r}\right) + \frac{A}{6C^3}\left(-\frac{\partial u}{\partial r}\right)^3\right]_{r=R}, q_w = -k\left(\frac{\partial T}{\partial r}\right)_{r=R}, j_w = -D\left(\frac{\partial C}{\partial r}\right)_{r=R} \tag{5.14}$$

while non-dimensionless form of the surface drag coefficient, surface heat flux coefficient and surface mass flux are defined as:

$$\left.\begin{array}{c} \frac{1}{2}C_f Re^{1/2} = \alpha f''(\eta) + \frac{\alpha\beta}{3}(f''(\eta))^3 \text{ at } \eta \to 0, \\ Nu_w Re^{-1/2} = -\theta'(\eta), \text{ at } \eta \to 0, \\ Sh Re^{-1/2} = -\phi'(\eta), \text{ at } \eta \to 0. \end{array}\right\} \tag{5.15}$$

5.2 Computational algorithm

The governing set of equations (Eqs. $(5.8) - (5.10)$) under endpoint conditions in Eq. (5.11) are solved by an efficient numerical scheme called shooting technique with Runge-Kutta-Fehlberg method. (Mention in Chapter 1)

5.3 Physical and graphical outcomes

This section is fascinated to examine the rheological features of embedded parameter namely Prandtl fluid parameter α, elastic parameter β, curvature parameter γ, velocity slip parameter λ^*, magnetic field parameter M, Brownian motion parameter Nb, Prandtl number Pr, thermophoresis parameter Nt, Biot number Bi, chemical reaction parameter δ_c and Lewis number Le on fluid velocity, temperature, and concentration. Moreover, physical quantities of interest i.e., surface drag force coefficient, surface heat flux coefficient and surface mass flux coefficient are reported by means of both straight-line curve fitting and tabular structure.
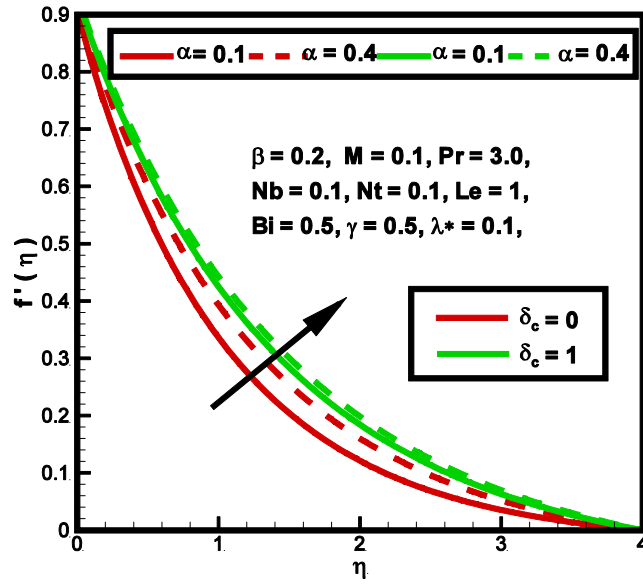
Fig. 5.2: Impact of α on $f'(\eta)$ in absence/presence of δ_c.
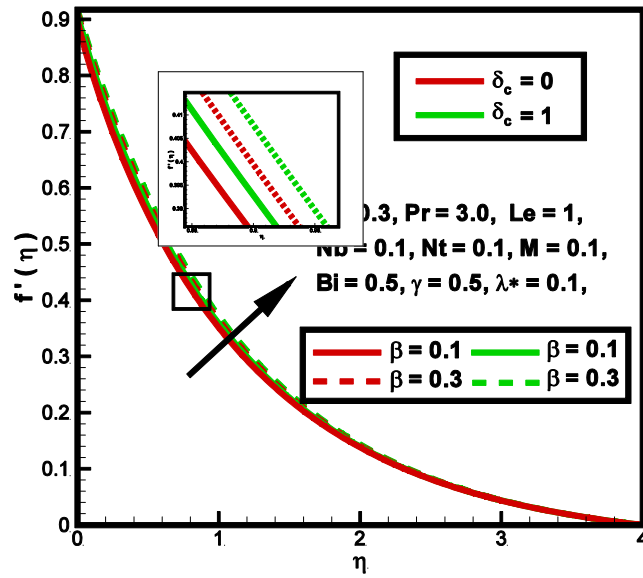
Fig. 5.3: Impact of β on $f'(\eta)$ in absence/presence of δ_c.
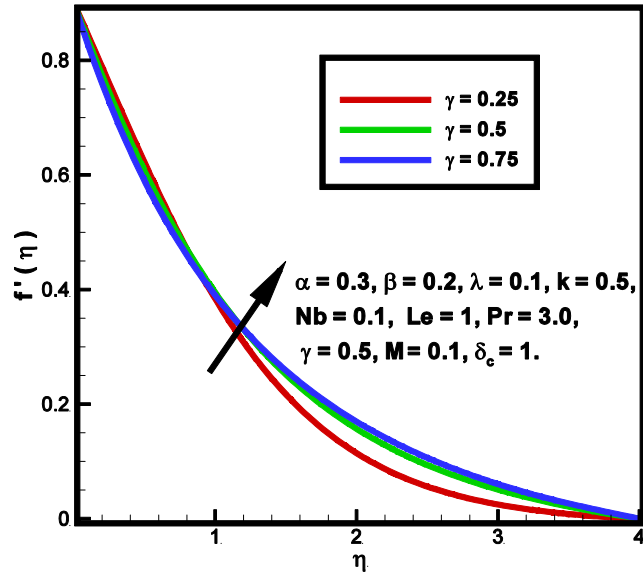
Fig. 5.4: Impact of γ on $f'(\eta)$ in absence/presence of δ_c.
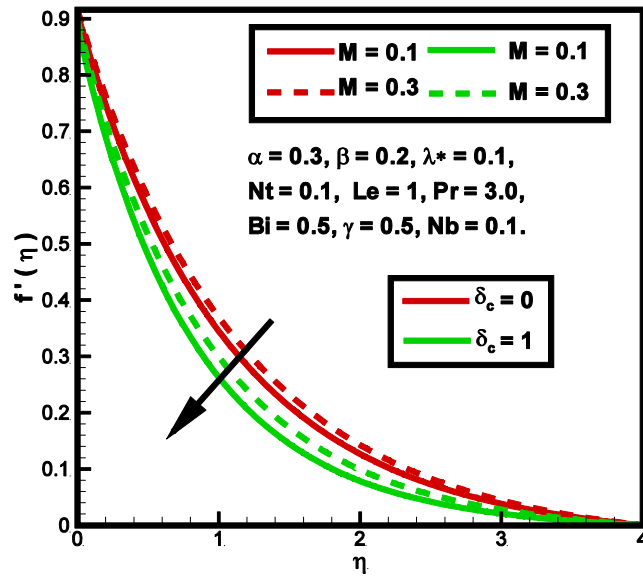
Fig. 5.5: Impact of M on $f'(\eta)$ in absence/presence of δ_c.
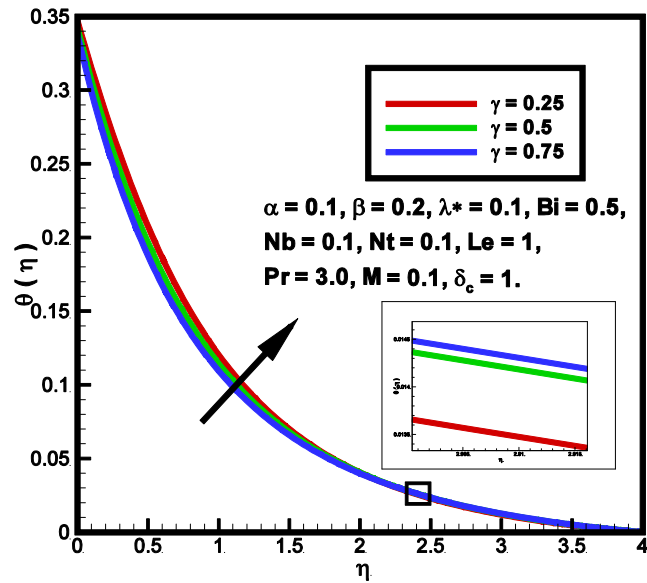
Fig. 5.6: Impact of γ on $\theta(\eta)$ in the absence/presence of δ_c.
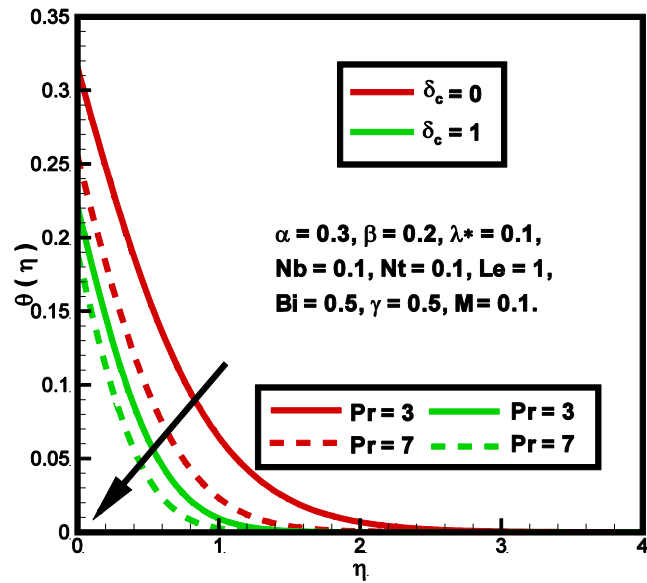
Fig. 5.7: Impact of Pr on $\theta(\eta)$ in the absence/presence of δ_c.
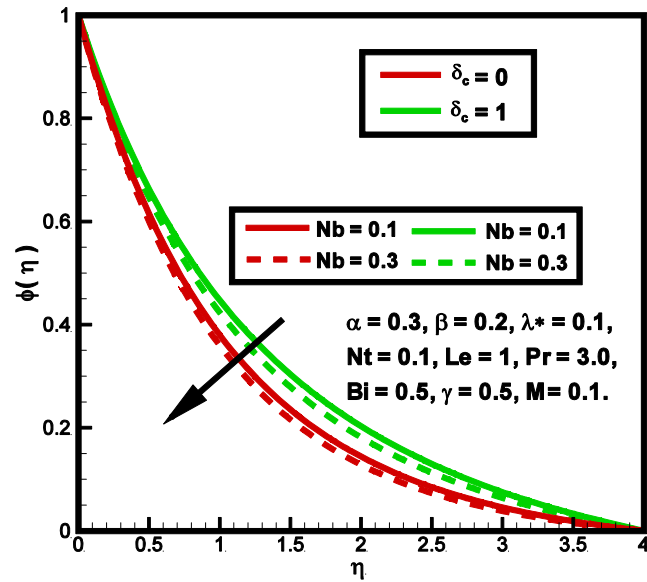
Fig. 5.8: Impact of Nb on $\theta(\eta)$ in the absence/presence of δ_c.
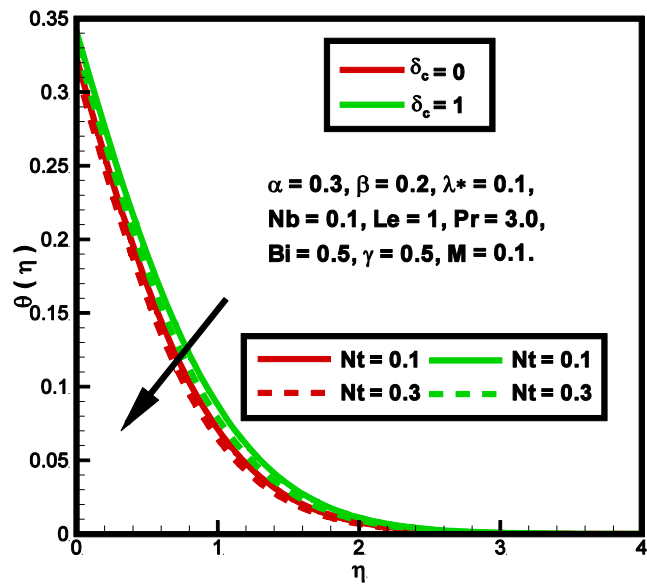
Fig. 5.9: Impact of Nt on $\theta(\eta)$ in the absence/presence of δ_c.
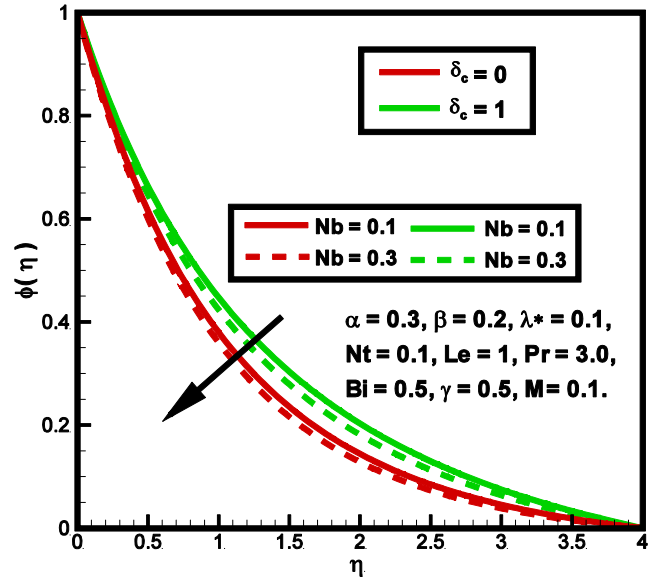
Fig. 5.10: Impact of Nb on $\phi(\eta)$ in the absence/presence of δ_c.
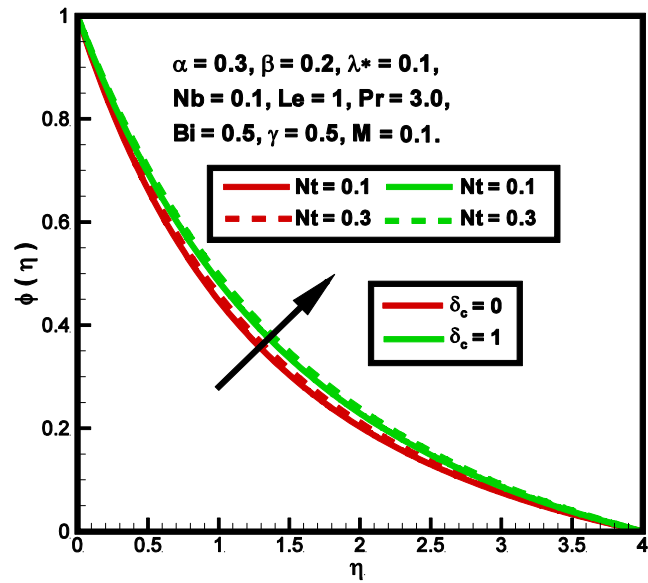
Fig. 5.11: Impact of Nt on $\phi(\eta)$ in the absence/presence of δ_c.
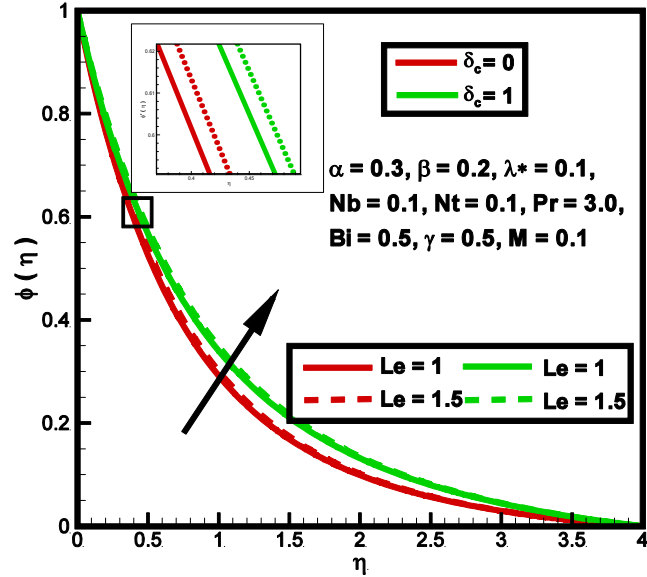
Fig. 5.12: Impact of Le on $\phi(\eta)$ in the absence/presence of δ_c.
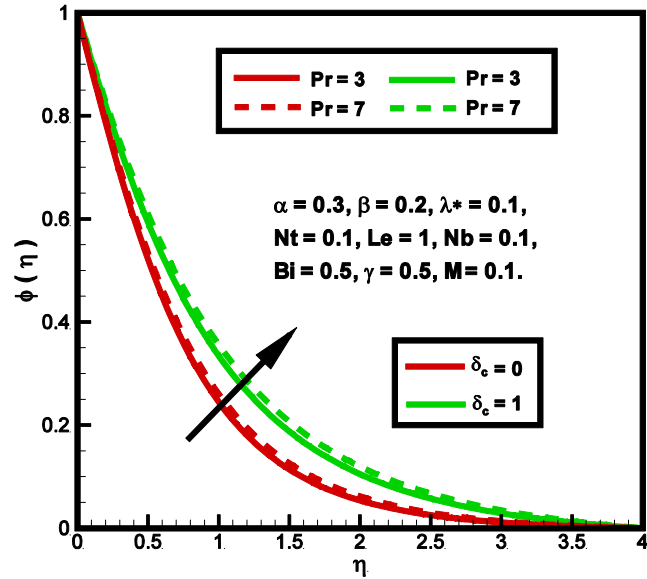
Fig. 5.13: Impact of Pr on $\phi(\eta)$ in the absence/presence of δ_c.
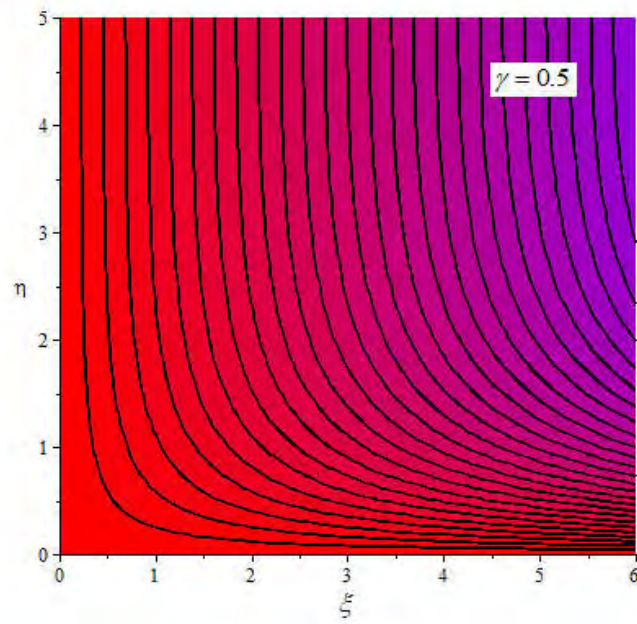
Fig. 5.14(a): Streamlines against curvature parameter.
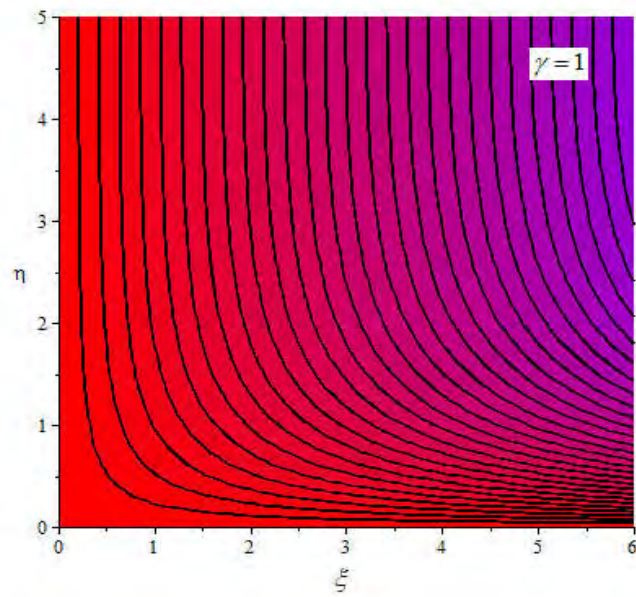
Fig. 5.14(b): Streamlines against curvature parameter.
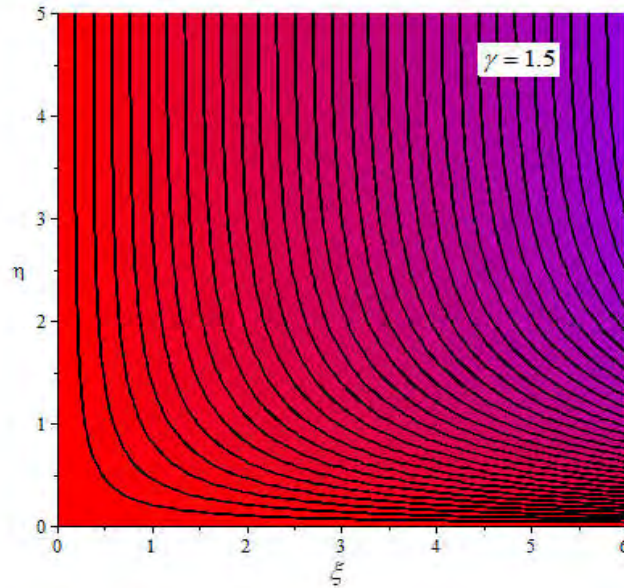
Fig. 5.14(c): Streamlines against curvature parameter.

Figs. 5.2 and 5.3 depict the effects of α and β on fluid velocity respectively in the absence/presence of δ_c. From graphical trends it is perceived that for higher values of both α and β the momentum BL thickness reduces irrespective of involvement of chemical reaction, but it is clear from both figures the significant decline is observed when flow regime is manifested with chemical reaction effect. **Fig.** 5.4 reveal that the variation of Prandtl Eyring fluid velocity towards γ when system is undergoing with chemical reaction. It is seen from these curves that the fluid velocity shows an increasing nature via γ. As $\gamma > 0$ admits decrease in radius of cylinder thus less resistance is offered towards Prandtl Eyring fluid particles and consequently velocity enhances. **Fig.** 5.5 elucidates the impact of M on Prandtl Eyring fluid temperature for zero and non-zero δ_c. It is clear from these curves an increase in M leads to resist fluid motion. **Fig.** 5.6 is developed for the physical interpretation of γ on temperature. It is observed by increasing γ temperature profile increases. **Fig.** 5.7 predicts the impression of Pr on fluid temperature for zero and non-zero values of δ_c. The graphical plotting depicts that both δ_c and Pr having same effect on fluid temperature. It is noted that for $\delta_c = 0$ and by enlarging the values of Pr, the momentum diffusivity increases, and thermal

diffusivity decreases. Therefore, thermal BL thickness becomes thinner which causes decline in fluid temperature. It is also noted that for $\delta_c > 0$ the thermal BL thickness decreases rapidly which brings a significant decrease in temperature. It is on the grounds that some temperature in the form of energy is used to augment the chemical reaction. **Fig.** 5.8 elucidates the impact of Nb on temperature for zero and non-zero δ_c. It is found that for both cases the fluid temperature shows an inciting trend against positive values of Nb. Since Brownian motion expedites the movement of molecules, thus they collide with each other very rapidly and produce thermal energy. On the contrary, presence of δ_c drops the fluid temperature. **Fig.** 5.9 assess the effect of Nt on fluid temperature for zero and non-zero δ_c. It is seen that the fluid temperature increases for positive values of Nt for zero and non-zero δ_c. **Fig.** 5.10 displays the combined effect of Nb and δ_c on nanoparticle concentration. It is seen those higher values of Nb drops the nanoparticle concentration because increment in Nb is responsible for random motion of nanoparticles, as a result concentration decreases. However, in presence of destructive chemical nanoparticle concentration profile increases resulting the thicker concentration boundary layer. **Fig.** 5.11 reveals the effect of Nt for zero and non-zero δ_c. It is clear from these curves that both parameters have same impact on nanoparticle concentration. **Fig.** 5.12 discloses the effect of Le on concentration profile of nanofluid for zero and non-zero δ_c. Concentration profile increases for higher values of Le regardless of δ_c. **Fig.** 5.13 investigates the impact of Pr on nanoparticle volume fraction in absence/presence of chemical reaction. It is evident that by increasing Pr and δ_c nanoparticle volume fraction increases significantly.
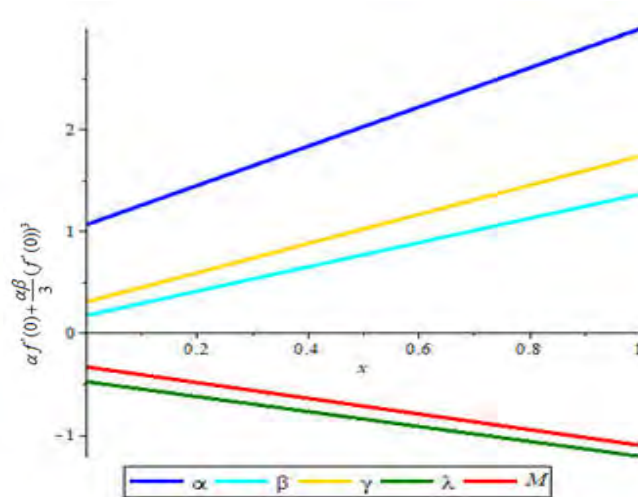
Fig. 5.15: Straight line curve fitting for wall shear stress.
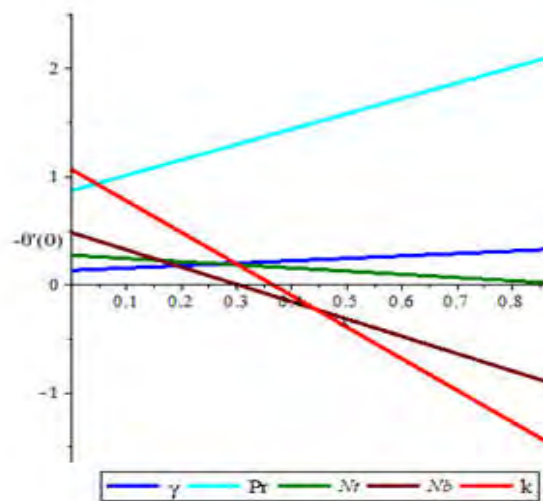
Fig. 5.16: Straight line curve fitting for heat transfer rate.
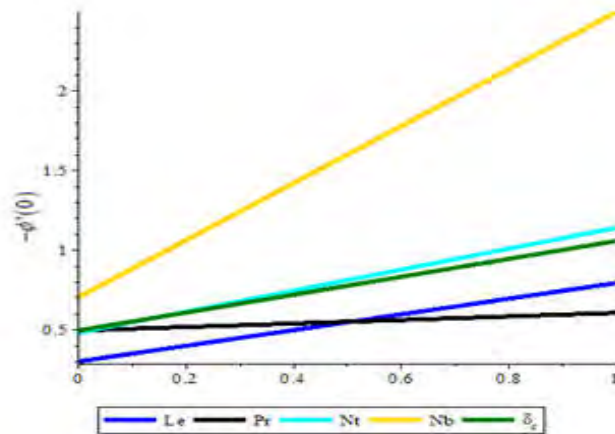
Fig. 5.17: Straight line curve fitting for mass transfer rate.

Fig. 5.14(a), **Fig.** 5.14(b), and **Fig.** 5.14(c) are prepared to examine the flow pattern of Prandtl nanofluid. **Fig.** 5.15 and **Table** 5.1 are demonstrated parallel to elaborate the effects of $\alpha, \beta, \gamma, \lambda$ and M on wall shear stress. It is perceived that surface drag force coefficient is increasing for all positive values of α, β, γ but opposite behaviour is noted for λ and M. **Fig.** 5.16 and **Table** 5.2 are equipped to check the influence of embedded parameters on temperature gradient. It is noted from these numeric values that the coefficient of surface heat flux increases for all positive values of γ, Pr and decreases for Nt, Nb and k. **Fig.** 5.17 and **Table** 5.3 depicts the variations in local Sherwood number via Le, Pr, Nt, Nb and δ_c. The involved parameters enhance the local Sherwood number.

Table 5.1: Numerical variation of skin-friction coefficient for different parameters.

α	β	γ	λ^*	M	$\alpha f''(0) + \dfrac{\alpha\beta}{3}[f''(0)]^3$
0.3	0.2	0.5	0.1	0.1	-0.4073
0.4	-	-	-	-	-0.9012
0.5	-	-	-	-	-1.4121
0.3	0.2	-	-	-	-0.4073
-	0.4	-	-	-	-0.6481
-	0.5	-	-	-	-0.7635
-	0.2	0.5	-	-	-0.4096
-	-	1	-	-	-1.1251
-	-	1.5	-	-	-1.7481
-	-	0.5	0.1	-	-0.4073
-	-	-	0.3	-	-0.2612
-	-	-	0.5	-	-0.1815
-	-	-	0.1	0.1	-0.4073
-	-	-	-	0.3	-0.5626
-	-	-	-	0.7	-0.7253

Table 5.2: Numerical variation of heat transfer rate for different parameters.

γ	Pr	Nt	Nb	Bi	$-\theta'(0)$
0.5	3	0.1	0.1	0.5	0.2417
1	-	-	-	-	0.3556
1.5	-	-	-	-	0.4517
0.5	3	-	-	-	0.2417
-	5	-	-	-	0.4320
-	7	-	-	-	0.7121
-	3	0.1	-	-	0.2417
-	-	0.2	-	-	0.2141
-	-	0.3	-	-	0.1782
-	-	0.1	0.1	-	0.2417
-	-	-	0.2	-	0.2212
-	-	-	0.3	-	0.2031
-	-	-	0.1	0.1	0.7104
-	-	-	-	0.3	0.5158

Table 5.3: Numerical variation of mass transfer rate for different parameters.

Le	Pr	Nt	Nb	δ_c	$-\phi'(0)$
0.5	0.5	0.1	0.1	0.1	0.5463
1	-	-	-	-	0.7934
1.5	-	-	-	-	0.9946
0.5	0.5	-	-	-	0.5463
-	1	-	-	-	0.6008
-	1.5	-	-	-	0.6458
-	0.5	0.1	-	-	0.5463
-	-	0.2	-	-	0.6124
-	-	0.3	-	-	0.7314
-	-	0.1	0.1	-	0.5463
-	-	-	0.2	-	0.8201
-	-	-	0.3	-	1.1241
-	-	-	-	0.1	0.5463
-	-	-	-	0.2	0.6042

5.4 Conclusion

The current attempt deals numerical execution on hydromagnetic flow of Prandtl nano fluid due to stretching cylinder with partial slip condition. The fluid flow regime is established with chemical reaction phenomena. The modelled mathematical equations are converted into a system of ODEs and then shooting method was applied to explain the physical characteristics of involved parameters. For zero and non-zero δ_c, conclusions of present analysis are listed as follows:

- Prandtl fluid velocity indicates an inciting trend towards both Prandtl fluid and elastic parameters.
- Fluid velocity and temperature both are increasing functions of curvature parameter, Brownian motion and thermophoresis parameters.
- Fuid velocity and temperature both are decreasing function of Magnetic field.

- Nanoparticle concentration decreasing by increasing Nb while opposite trend is noticed via Nt, $\boldsymbol{Le}$ and Pr.

- Skin-friction coefficient shows increasing nature for α, β, γ but opposite behaviour is observed for λ and M.

- It is observed from these numeric values that the coefficient of surface heat flux is increases for all positive values of γ, Pr and decreases for Nt, Nb and k.

- Local Sherwood number shows an inciting value via Le, Pr, Nt, Nb and δ_c.

Chapter 6

Mathematical analysis on MHD Prandtl-Eyring nanofluid new mass flux conditions

A theoretical study has been presented to investigate the important characteristics of magnetohydrodynamics (MHD) Prandtl-Eyring nanofluid flow over stretching surface. Effect of convective and Navier slip boundary conditions are included in flow field. Concentration of nanoparticles is assumed along with higher order chemical reactions and Nield-condition. The mathematical modelling of this physical flow problem accomplished the nonlinear partial differential equations along with appropriate boundary conditions. The non-dimensional form of governing problem is yielded with the aid of similarity variables. The pivotal physical quantities, i.e., velocity, temperature, and concentration (in non-dimensional form) within boundary layer region are computed with shooting technique. The physical significance of flow controlling parameters on velocity, temperature and concentration is illustrated through graphs. Additionally, thermophysical aspects of fluid near stretching surface (wall friction factor, wall heat flux and wall mass flux) are instantiated graphically. A comparison of the current solution with reported data is established to validate the accuracy of adapted procedure. It is observed that the current findings agree with existing data. This led to confidence on adapted numerical procedure.

6.1 Mathematical formulation

Consider a two-dimensional incompressible, non-Newtonian Prandtl-Eyring nanofluid flow over a stretching sheet. The plane surface is assumed at $y = 0$ which stretched linearly along positive x-direction with velocity $U(x) = ax$ and the fluid is filled in the region $y > 0$. A transverse magnetic field of strength B_0 is applied in orthogonal direction. The convective heat transfer is considered, and effects of higher order chemical reactions are included in the concentration of nanoparticles as well.

$$\frac{\partial u}{\partial x} + \frac{\partial v}{\partial y} = 0, \tag{6.1}$$

$$u\frac{\partial u}{\partial x} + v\frac{\partial u}{\partial y} = \frac{A}{\rho}\frac{\partial^2 u}{\partial y^2} - \frac{A}{2\rho C^3}\left(\frac{\partial u}{\partial y}\right)^2\frac{\partial^2 u}{\partial y^2} - \frac{\sigma B_0^{\,2}}{\rho}u, \tag{6.2}$$

$$u\frac{\partial T}{\partial x} + v\frac{\partial T}{\partial y} = \alpha\frac{\partial^2 T}{\partial y^2} + \tau D_B\left(\frac{\partial C}{\partial y}\cdot\frac{\partial T}{\partial y}\right) + \frac{\tau D_T}{T_\infty}\left(\frac{\partial T}{\partial y}\right)^2, \tag{6.3}$$

$$u\frac{\partial C}{\partial x} + v\frac{\partial C}{\partial y} = D_B\frac{\partial^2 T}{\partial y^2} + \frac{D_T}{T_\infty}\frac{\partial^2 T}{\partial y^2} + K(C - C_\infty)^n, \tag{6.4}$$

the Navier slip conditions, convective conditions and Nield boundary conditions are assumed,

$$u = U(x) + L\frac{\partial u}{\partial y}, \; v = 0, \; -\kappa\frac{\partial T}{\partial y} = h(T_w - T), \; D_B\frac{\partial C}{\partial y} + D_T\frac{\partial T}{\partial y} = 0 \text{ at } y = 0, \tag{6.5}$$

$$u \to 0, \; T \to T_\infty, \; C \to C_\infty \text{ at } y \to \infty.$$
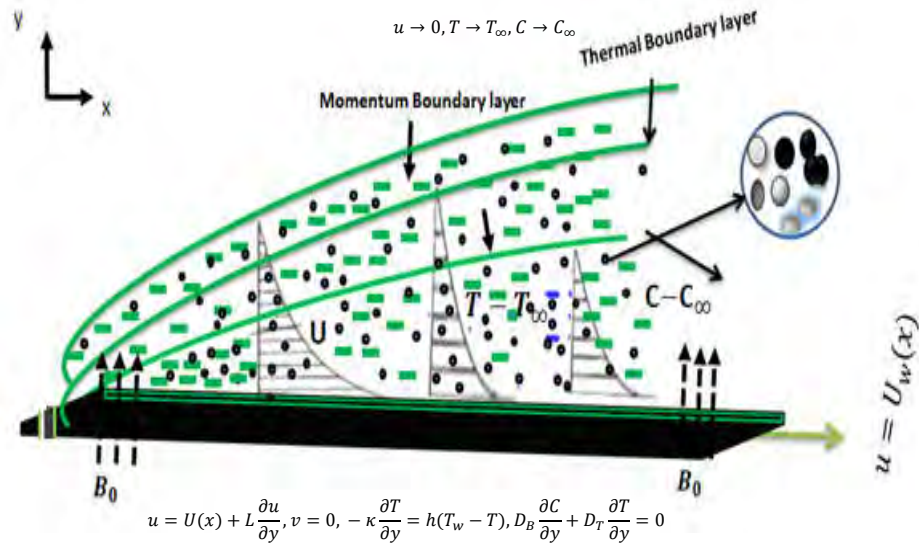
Fig. 6.1: Geometry of the problem.

In the above system of equations u, v denotes the velocity components in x and y directions, respectively. A and C represents fluid parameters, ρ displays the non-Newtonian fluid density, σ the electrical conductivity, fluid temperature is denoted by T, α is the thermal diffusivity, τ is the ratio of heat capacity of nanoparticles with the base

fluid, D_B is the coefficient of Brownian diffusion, coefficient of thermophoresis diffusion is symbolized by D_T, sheet surface temperature is represented by T_w while ambient temperature and ambient concentration are denoted by T_∞ and C_∞. K is the chemical reaction and n is the power law exponent, L is the parameter related to velocity slip, κ is the thermal conductivity and h is coefficient of convective heat flow.

The stream function for the current flow analysis is defined below,

$$u = \frac{\partial \Psi}{\partial y}, v = -\frac{\partial \Psi}{\partial x}. \tag{6.6}$$

The governing problem of flow configuration is transferred to dimensionless form with the applications of below defined appropriate set of similarity transforms,

$$\eta = \sqrt{\frac{a}{v}}y, \ \Psi = \sqrt{avx}f(\eta), \ \theta = \frac{T - T_\infty}{T_w - T_\infty}, \ \phi = \frac{C - C_\infty}{C_w - C_\infty}. \tag{6.7}$$

Now similarity variables (see Eq. (6.7)) are inserted into governing partial differential equations Eqs. (6.1) - (6.4). The similarity variables identically satisfy continuity equation while momentum, energy and concentration equations are transferred to the following system of nonlinear ordinary differential equations,

$$\alpha f''' - \alpha \beta f''^2 f''' - f'^2 + ff'' - Mf' = 0, \tag{6.8}$$

$$\theta'' + \Pr(f\theta' + Nb\theta'\phi' + Nt\theta'^2) = 0, \tag{6.9}$$

$$\phi'' + \frac{Nt}{Nb}\theta'' + \Pr Le(f\phi' - \delta_c\phi^n) = 0, \tag{6.10}$$

while prescribed two-point conditions are re-designed to

$$f(0) = 0, \ f'(0) = 1 + \lambda^* f''(0), \ \theta'(0) = -Bi(1 - \theta(0)), \ Nb\theta'(0) + Nt\phi'(0) = 0, \tag{6.11}$$
$$f'(\infty) \to 0, \ \theta(\infty) \to 0, \ \phi(\infty) \to 0.$$

In the above boundary value problem, the symbols $\alpha, \beta, M, \lambda, Nb, Nt, \Pr, Bi, Le$ and R display the Prandtl-Eyring parameters, Hartmann number, velocity slip parameter, Brownian motion parameter, thermophoresis parameter, Prandtl number, Biot number, Lewis number and chemical reaction parameter, respectively. These non-dimensional parameters are defined as follows,

$$\alpha = \frac{A}{\mu C}, \ \beta = \frac{a^3 x^2}{2C^2 v}, \ M = \frac{\sigma B^2}{a\rho}, \ \lambda^* = L\sqrt{\frac{a}{v}}, \tag{6.12}$$

$$Nt = \frac{\tau D_T (T_w - T_\infty)}{\alpha T_\infty}, \ Nb = \frac{\tau D_B (C_w - C_\infty)}{\alpha}, \ \text{Pr} = \frac{v}{\alpha},$$

$$\gamma = \frac{h}{\kappa}\sqrt{\frac{a}{v}}, \ Le = \frac{v}{D_B}, \ \delta_c = \frac{K}{a}.$$

Flow features near the surface are important part of present flow configuration. The physical quantities which deliberate the thermophysical properties near the surface are defined as

$$C_{fx} = \frac{\tau_w}{\frac{1}{2}\rho U^2}, \ Nu_x = \frac{xq_w}{\kappa(T_w - T_\infty)}, \ Sh_x = \frac{xq_m}{D_B(C_w - C_\infty)}, \tag{6.13}$$

where $C_{fx}, Nu_x,$ and Sh_x are mathematical symbols of coefficient of wall friction, local Nusselt number and local Sherwood number in order while τ_w, q_w and q_m expresses the wall shear stress, wall heat flux and wall mass flux, respectively. The laterally defined variables are mathematically given below,

$$\tau_w = \frac{A}{C}(\frac{\partial u}{\partial y})_{y=0} - \frac{A}{6C^3}(\frac{\partial u}{\partial y})^3_{y=0}, \ q_w = -\kappa(\frac{\partial T}{\partial y})_{y=0}, \ q_m = -D_B(\frac{\partial C}{\partial y})_{y=0}. \tag{6.14}$$

The similarity expressions of skin friction coefficient, local Nusselt number and local Sherwood number are found with the aid of similarity transforms (by inserting Eq. (6.7) into Eqs. (6.13) -(6.14))

$$\frac{1}{2}C_{fx}Re_x^{\frac{1}{2}} = \alpha f''(0) - \frac{\alpha\beta}{3}[f''(0)]^3, \ Nu_x Re_x^{-\frac{1}{2}} = -\theta'(0), \ Sh_x Re_x^{-\frac{1}{2}} = -\phi'(0). \tag{6.15}$$

In the above defined relations Re_x displays the local Reynolds number.

6.2 Computational algorithm

For better solution (in physical sense) of this system, numerical scheme (i.e., shooting technique) is utilized because this scheme provide freedom to choose feasible values of flow controlling parameters. The first action in this procedure is to convert higher order differential system into first order equations. The resulting system of equations is tackled with Runge-Kutta-Fehlberg scheme, but first missing initial approximations are required

and finite upper limit for η_∞ is to choose and convert this system into initial value problem. Now resulting initial value problem is solved with Runge-Kutta-Fehlberg scheme. The solution of this initial value problem corresponds to the solution of boundary value problem, such that it satisfies the boundary conditions. If the total error is less than tolerance value. Then computed solution will be the required solution, on the other hand assumed initial conditions are refined with the aid of Newton's method. This computing procedure is terminated when calculated solution satisfies the desired criteria.

6.3 Physical and graphical outcomes

The present work focuses on convective heat transfer of MHD Prandtl-Eyring nanofluid flow over stretched surface with Navier slip condition and chemical reactions. Flow govern problem is solved with Runge-Kutta-Fehlberg numerical scheme and presented through graphs and tables.

6.3.1 Non-dimensional velocity profile

The variations in the velocity curves are depicted through **Fig.** 6.2 against different values of controlling parameters α, β, λ and M. **Fig.** 6.2(A) elaborates the physical significance of Prandtl-Eyring parameter α on velocity profile. The magnitude of velocity enhances very rapidly for increasing values of Prandtl-Eyring parameter α. For higher values of Prandtl-Eyring parameter α, the viscosity of fluid decreases. Therefore, the average velocity of Prandtl-Eyring fluid enhances. **Fig.** 6.2(B) shows opposite trend of the fluid velocity against fluid parameter β, it brings resistance to fluid particles, as a result, the velocity of Prandtl-Eyring fluid declines. The influences of Navier slip parameter λ on dimensionless velocity are disclosed via **Fig.** 6.2(C). Enhancement in slip parameter λ creates more disturbance and decelerates the fluid motion; it can be observed from **Fig.** 6.2(D). As physical consequences of Hartmann number M brings enhancement in Lorentz force. Since it has resistive nature, thus fluid particles face strong resistance in context of their movement, therefore, the average velocity of Prandtl-Eyring fluid declines.

(A)

Legend:
- α = 1.0 (red solid)
- α = 1.4 (green dashed)
- α = 1.7 (blue dash-dot)
- α = 2.0 (black dashed)

$\beta = 0.2$, M = 0.1, Pr = 3.0, Nb = Nt = 0.1, $\delta_c = 0.1$, n = 2.0, $\lambda* = 0.1$, Le = 1.0, Bi = 0.5.

Axis: $f'(\eta)$ vs η

(B)

Legend:
- β = 0.1 (red solid)
- β = 0.4 (green dashed)
- β = 0.6 (blue dash-dot)
- β = 0.8 (black dashed)

$\alpha = 1.5$, M = 0.1, Pr = 3.0, Nt = Nb = 0.1, $\delta_c = 0.1$, n = 2.0, $\lambda* = 0.1$, Le = 1.0, Bi = 0.5.

Axis: $f'(\eta)$ vs η
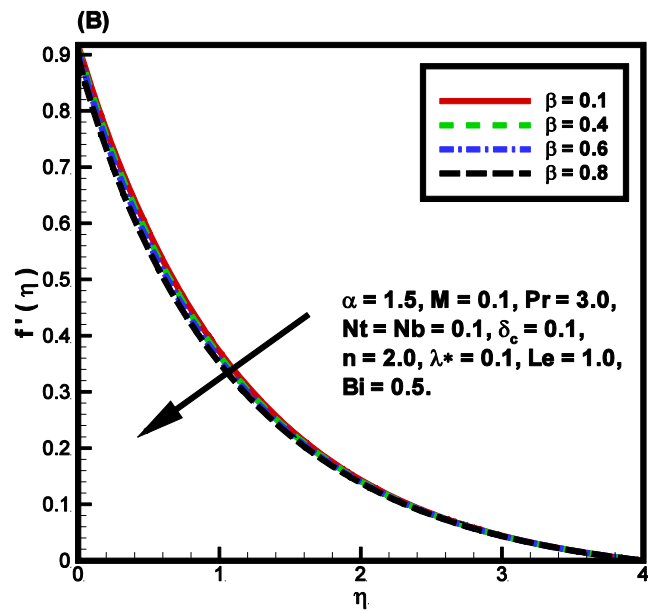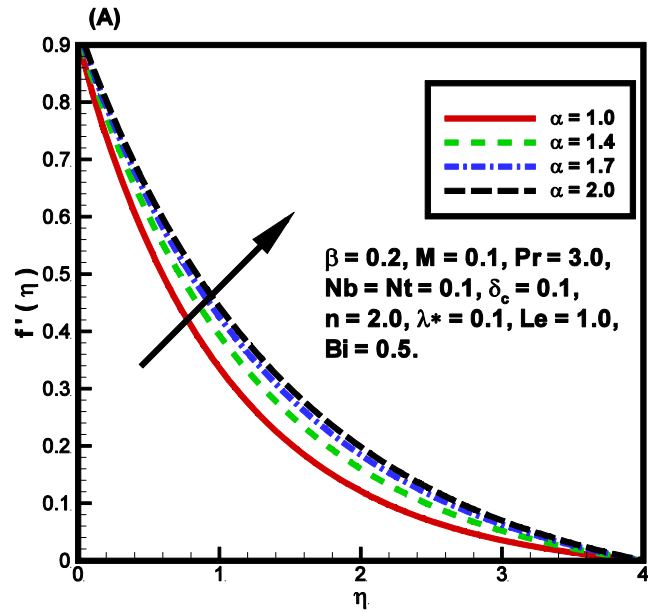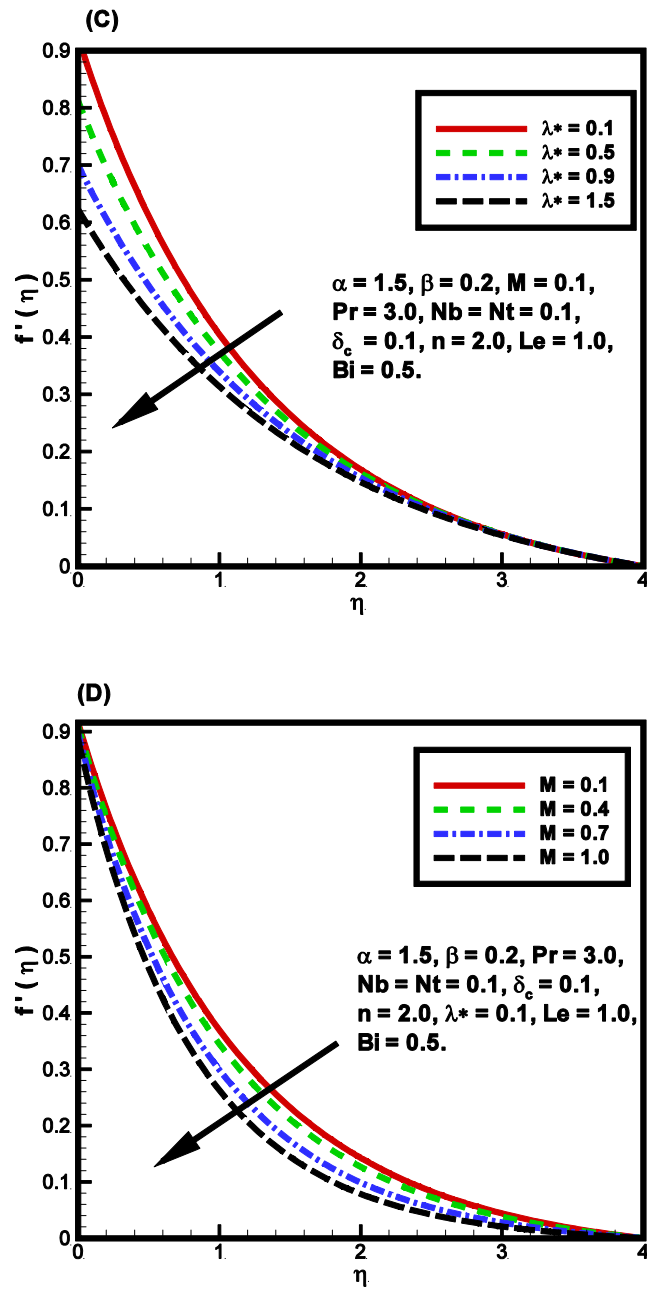
Fig 6.2: **(A)** Fluid velocity against fluid parameter α, **(B)** Fluid velocity against fluid parameter β, **(C)** Fluid velocity against slip parameter λ, **(D)** Fluid velocity against Hartmann number M.

6.3.2 Non-dimensional temperature profile

Behaviour of temperature profile is demonstrated via **Figs.** 6.3((A)-(D)) verses increasing values of $Nb, Nt,$ Pr and Bi. The dominance of Brownian motion on fluid thermal energy is surveyed through **Fig.** 6.3(A). As enlarging Brownian motion phenomenon accelerates collision process of solid nanoparticles and fast-moving liquid particles. This collision losses particles mechanical energy, this energy is converted into thermal form and hence temperature of the fluid enhances. This physical fact is validated via **Fig.** 6.3(A). The physical outcomes of thermophoresis on thermal energy are highlighted with the help of **Fig.** 6.3(B). As thermophoretic force pushes the hot fluid particles away from the surface, this process accelerates the transportation of thermal energy into fluid. As a result, fluid temperature rises very rapidly (it can be observed from the **Fig.** 6.3(B)). **Fig.** 6.3(C) portraits the variations of Prandtl number Pr on temperature profile (in physical sense). One can observed that the fluid with low Prandtl number Pr possesses high thermal energy and vice versa. It holds because Prandtl number Pr corresponds inversely with capability of conduction. In **Fig.** 6.3(D) Biot number Bi estimates the quotient of heat transfer resistances inside and on the surface. As a result, the temperature profile decreases.

(B)

(C)
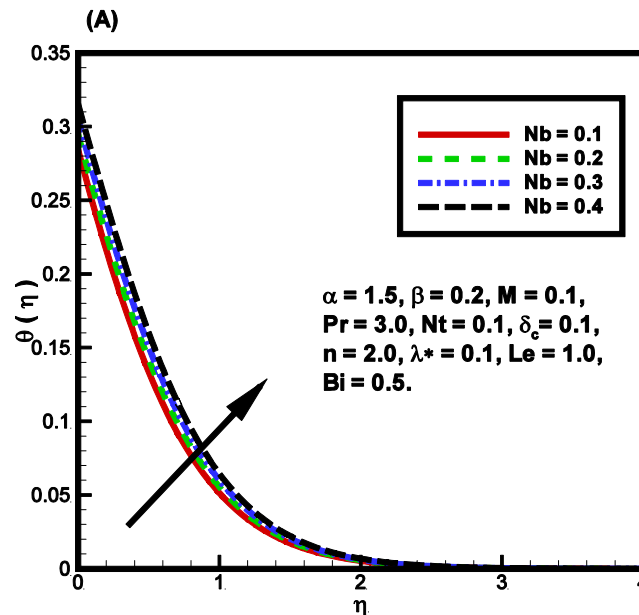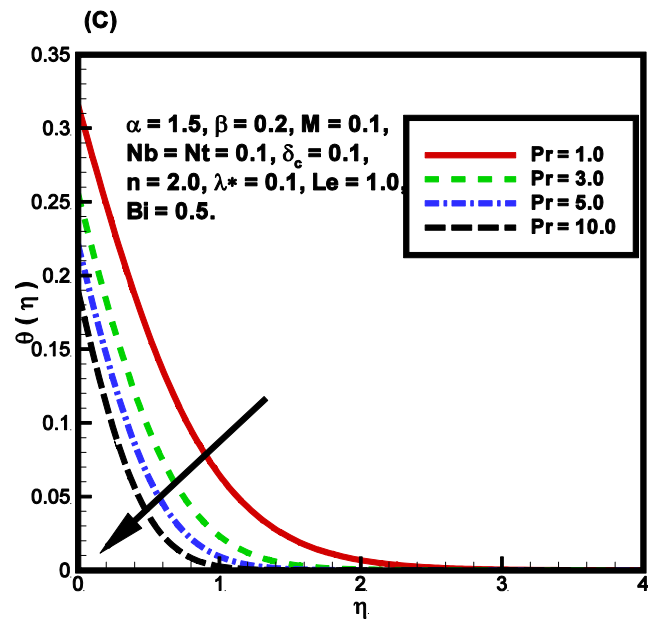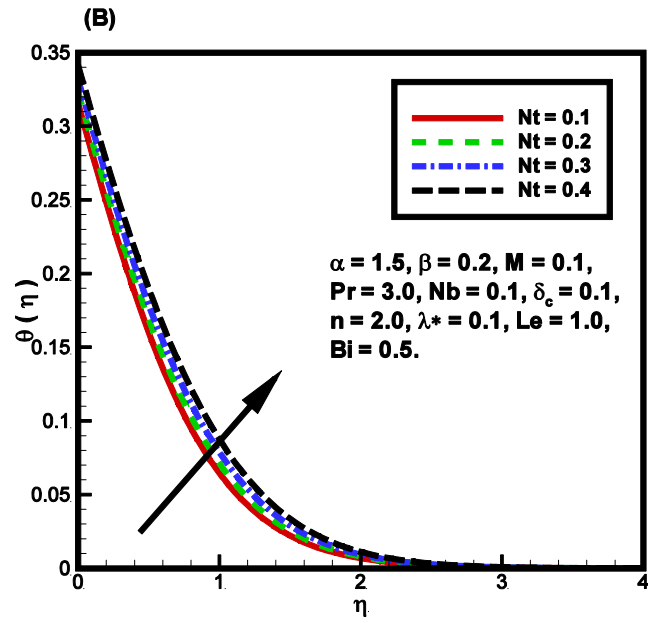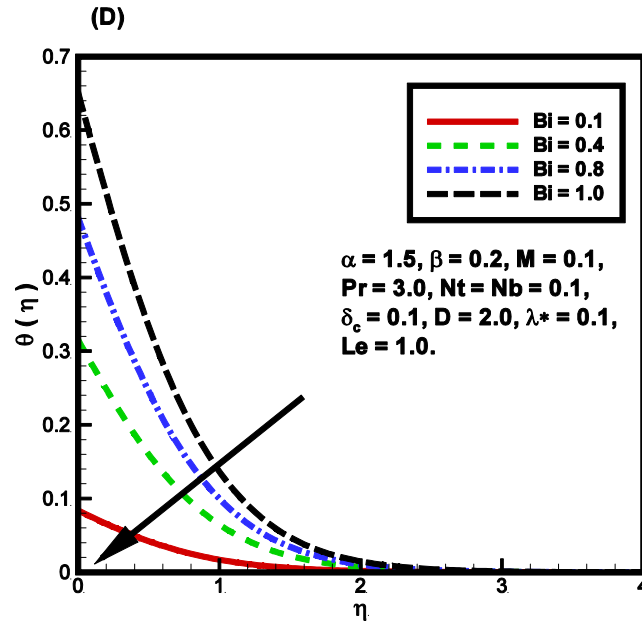
Fig. 6.3: (A) Fluid temperature versus Brownian motion parameter Nb, **(B)** Fluid temperature versus thermophoresis para5meter Nt, **(C)** Fluid temperature versus Prandtl number Pr, **(D)** Fluid temperature versus Biot number Bi.

6.3.3 Non-dimensional concentration profile

The modifications in concentration profile verses thermophysical are assessed through **Figs.** 6.4((A)-(F)). The influences of nonlinearity index of chemical reaction n on nanoparticle concentration are discussed with the help of **Fig.** 6.4(A). It can be noticed that the increasing order of chemical reaction boosts the concentration of nanoparticle. **Fig.** 6.4(B) elaborates the solutal variations concisely against chemical reaction parameter R. The strength of chemical reaction causes depletion in nanoparticle concentration. Physical aspects of concentration profile verses Lewis number Le are deliberated with the aid of **Fig.** 6.4(C). Since Lewis number relates the momentum diffusion to mass diffusion. Hence nanofluid having large Lewis number possess low concentration and vice versa. **Fig.** 6.4(D) addressed the effects of Prandtl number Pr on nanofluid concentration. This figure manifested that the Prandtl number Pr immensely reduces the concentration profile. **Figs.** 6.4((E)-(F)) represent the attributes of non-

dimensional nanofluid concentration verses Brownian motion parameter Nb and thermophoresis parameter Nt. It can be observed that both the parameters have reverse effects on nanofluid concentration. Since Brownian motion disperses the nanoparticles in irregular way. Hence this causes reduction in concentration profile. On the other hand, thermophoresis phenomenon propelled the hot particle from surface through nanofluid, as a result, concentration of nanoparticles enhances.

(A)

(B)

(C)

α = 1.5, β = 0.2, , M = 0.1,
Pr = 3.0, Nt = Nb = 0.1,
δ_c = 0.1, n = 2.0, λ* = 0.1,
Bi = 0.5.

——	Le = 1.0
- - -	Le = 2.0
—·—·	Le = 5.0
- - -	Le = 10.0

(D)

α = 1.5, β = 0.2, M = 0.1,
Nt = Nb = 0.1, δ_c = 0.1,
Le = 1.0, n = 2.0, λ* = 0.1
Bi = 0.5.

——	Pr = 2.0
- - -	Pr = 3.0
—·—·	Pr = 5.0
- - -	Pr = 10.0

(E)

$\alpha = 1.5, \beta = 0.2, M = 0.1,$
$Pr = 3.0, Nt = 0.1, \delta_c = 0.1,$
$Le = 1.0, n = 2.0, \lambda* = 0.1,$
$Bi = 0.5.$

Nb = 0.1
Nb = 0.2
Nb = 0.3
Nb = 0.4

(F)

$\alpha = 1.5, \beta = 0.2, M = 0.1,$
$Pr = 3.0, Nb = 0.1, \delta_c = 0.1,$
$Le = 1.0, n = 2.0, \lambda* = 0.1,$
$Bi = 0.5.$

Nt = 0.1
Nt = 0.2
Nt = 0.3
Nt = 0.4
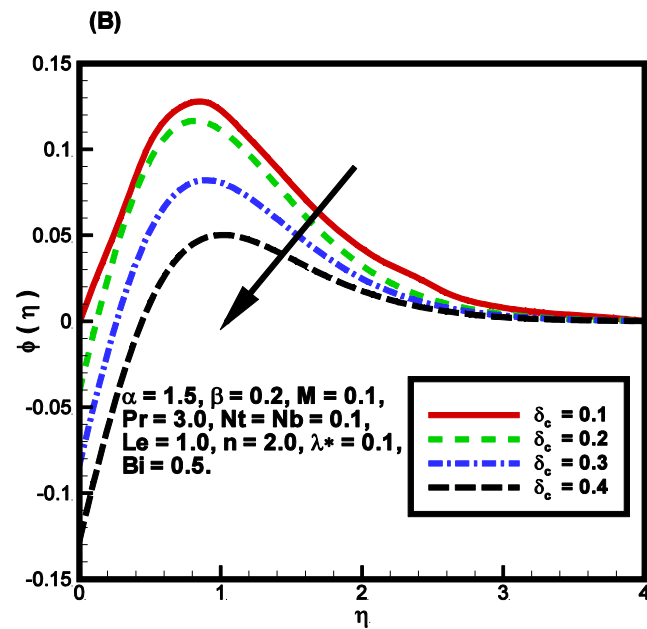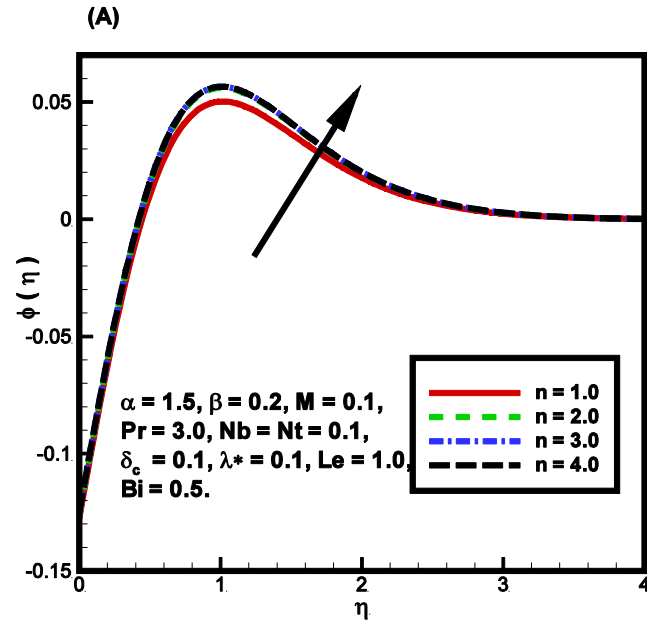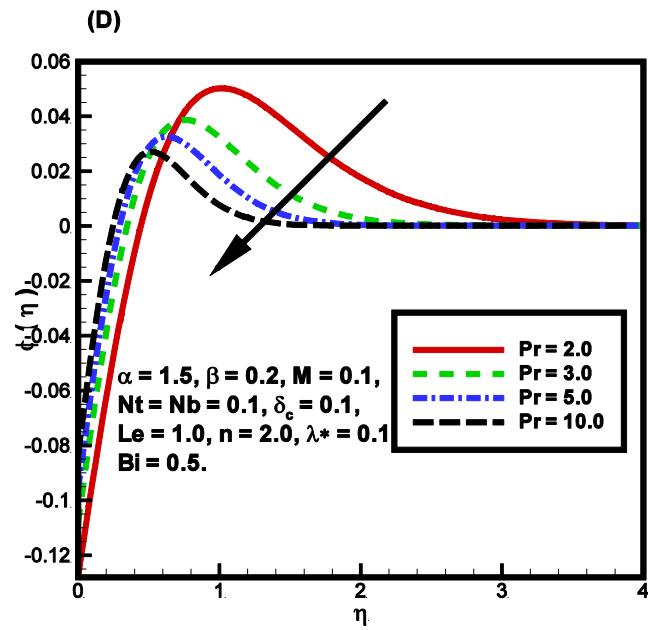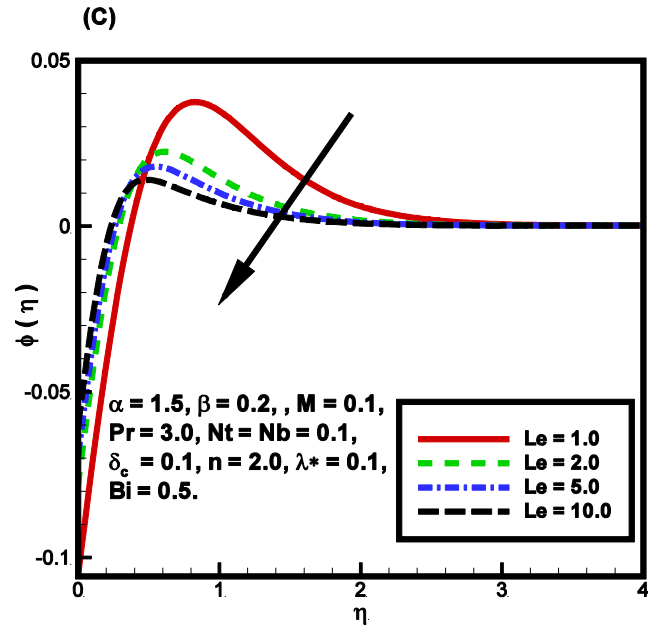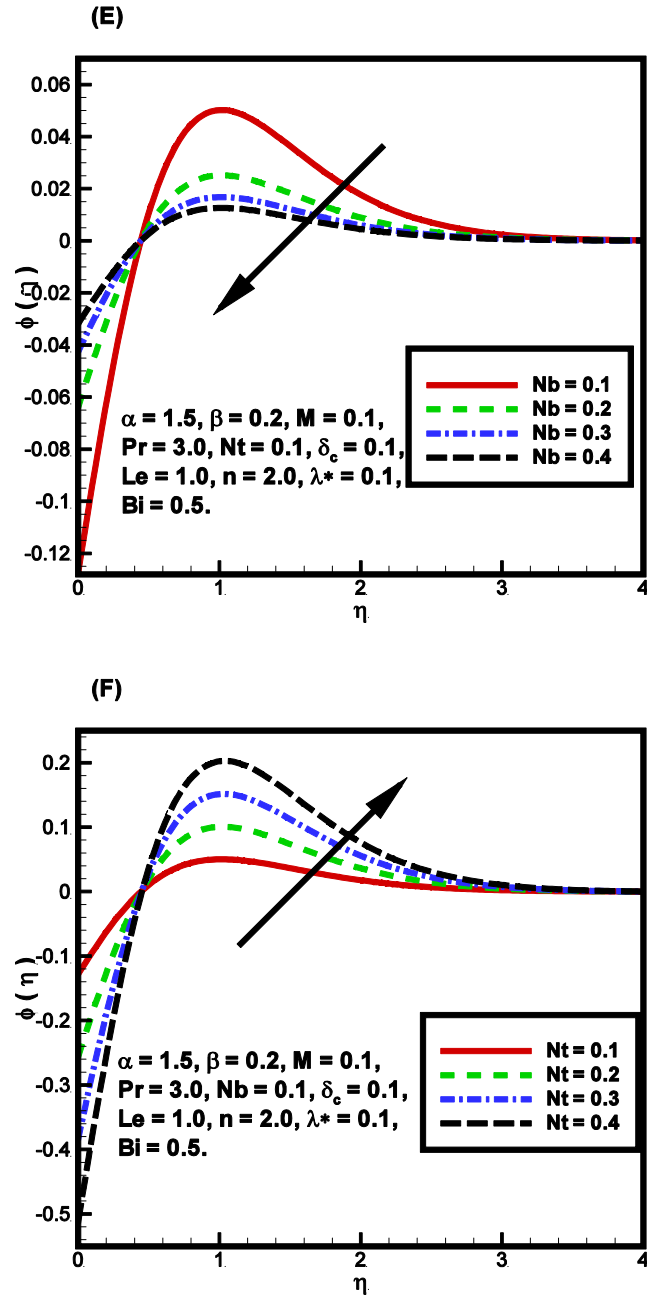
Fig. 6.4: **(A)** Nanoparticle concentration verses power law exponent n, **(B)** Nanoparticles concentration verses chemical reaction parameter δ_c, **(C)** Nanoparticles concentration verses Lewis number Le, **(D)** Nanoparticles concentration verses Prandtl number Pr, **(E)** Nanoparticles concentration verses Brownian motion parameter Nb, **(F)** Nanoparticles concentration verses thermophoresis parameter Nt.

6.3.4 Non-dimensional wall friction factor

The impact of controlling parameters α, β, λ and M on wall friction factor (for both Newtonian nanofluid and non-Newtonian nanofluid) are discussed via **Figs.** 6.5((A)-(B)). **Fig.** 6.5(A) predicts that the surface friction of non-Newtonian nanofluid is quite greater than viscous nanofluid surface friction. Additionally, partial slip condition reduces the wall friction very much in both cases. **Fig.** 6.5(B) narrates the consequences of momentum controlling parameters $\alpha, \beta,$ and M on wall friction. Fluid parameters α and β have opposite impact on surface friction of nanofluid. The wall friction enlarges towards fluid parameter α while fluid parameter β minimizes the surface friction. Similar aspects are noticed for the wall friction towards Hartmann number M.
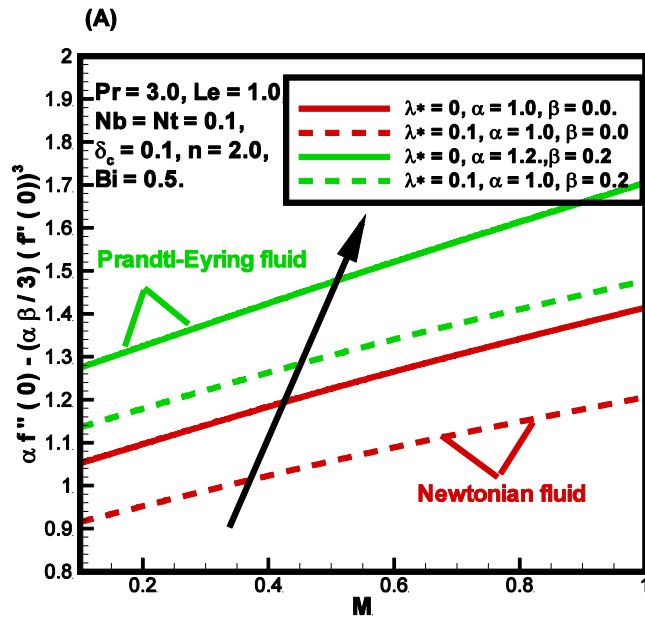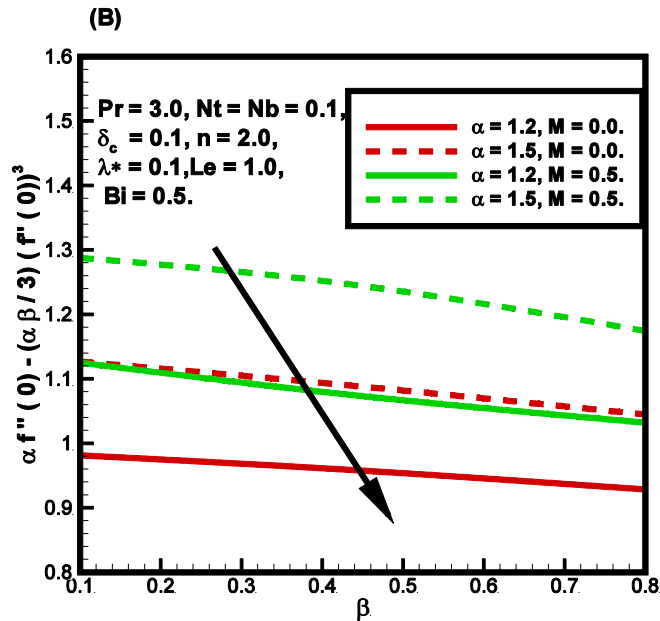
Figs. 6.5:((A)-(B)) Impacts of governing parameters α, β, λ and M on wall friction factor.

6.3.5 Non-dimensional wall heat flux

The influence of thermal parameters $Nb, Nt,$ Pr and Bi on wall temperature gradient are exhibited via **Figs.** 6.6((A)-(B)). Variations in wall heat flux against physical parameters Nb, Pr and Bi reveals with the aid of **Fig.** 6.6(A). Both Biot number Bi and Brownian motion parameter Nb reduces the wall heat flux while Prandtl number Pr intensify the wall friction factor. **Fig.** 6.6(B) communicate the aspects of wall heat flux towards controlling flow parameters Pr, Nt and Bi. This figure predicts that thermophoresis parameter Nt decelerate the rate of heat transfer from surface.
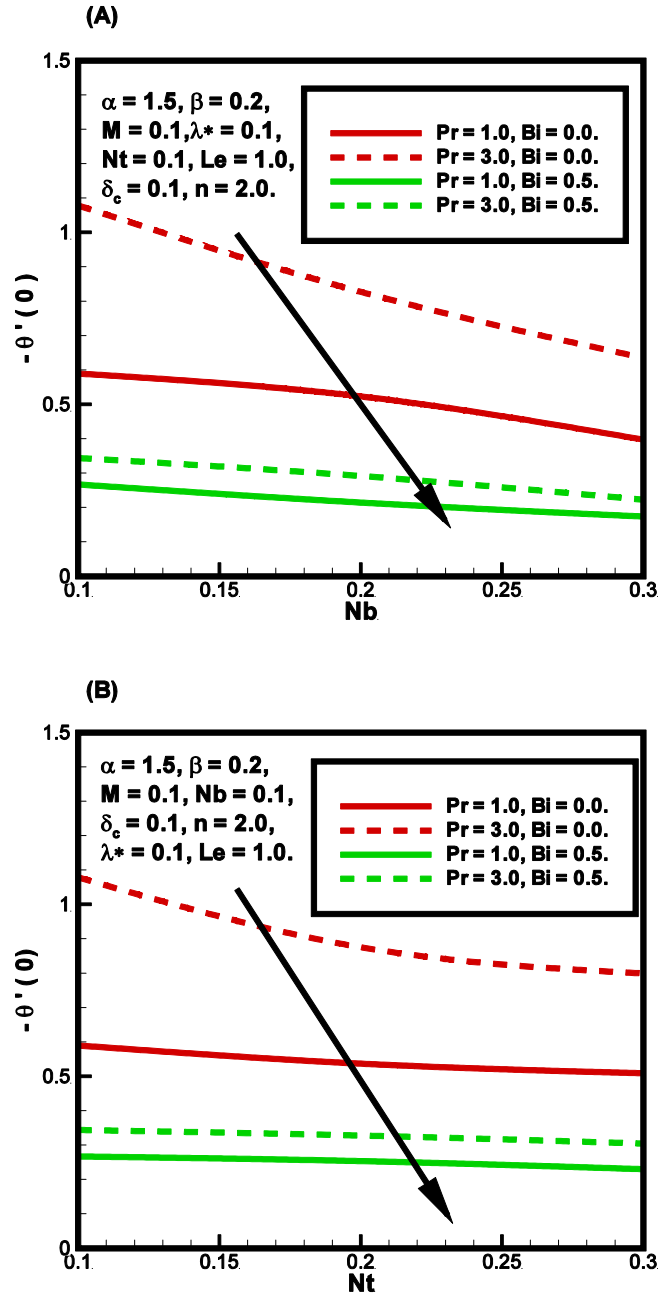
Figs. 6.6:((A)-(B)) Combined influences of controlling parameters Nb, Nt, Pr and Bi on wall heat flux.

6.3.6 Non-dimensional wall mass flux

The variations in non-dimensional wall mass flux is investigated against involving thermophysical parameters namely, $\mathrm{Pr}, Le, R, n, Nt$ and Nb via **Figs. 6.7**((A)-(B)). Fig.

6.7(A) divulges the impacts of flow parameters Le, R and Nb on wall mass gradient. All three parameters Le, R and Nb enhances the wall mass flux very rapidly (this can be observed from **Fig**. 6.7(A)). The consequences of flow controlling parameters $\Pr, n$ and Nt on wall mass flux are observed from **Fig.** 6.7(B). This figure exposes that the controlling parameters $\Pr, n$ and Nt accelerates the rate of mass transfer from surface.
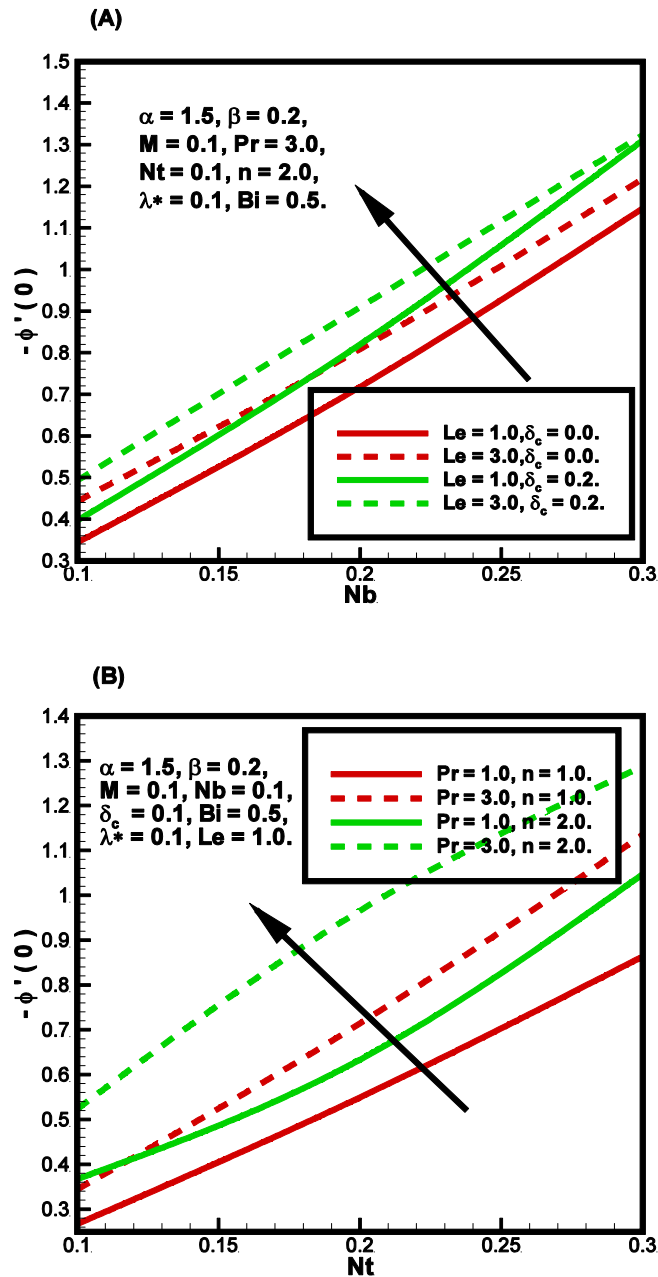
Figs. 6.7: ((A)-(B)) Consequences of thermo-physical parameters $Nb, Nt, \Pr, Le, R$ and n on wall mass flux.

To access the accuracy of calculated results, a comparison is established with previously reported data through **Table** 6.1. This comparison shows that the present results have quite resemblance with previous data which leads to give confidence on adapted method. To insight physical aspects of under considered problem more explicitly, the computed results are presented through graphical and tabular manner.

Table 6.1: Comparison of skin friction coefficient against different values of Hartmann number M and fixing $\alpha = 1, \beta = \lambda^* = 0$.

M	Akbar et al. [32]	Malik et al. [31]	Present Result
0	-1	-1	-1
0.5	-1.11803	-1.11802	-1.1180
1.0	-1.41421	-1.41419	-1.4142
5.0	-2.44949	-2.44845	-2.4495
10	-3.31663	-3.31657	-3.3166

Table 6.2: Fluctuations in wall friction factor i.e., $\alpha f''(0) - \frac{\alpha\beta}{3}(f''(0))^3$ verses growing values of flow parameters α, β, λ^* and M.

α	β	λ^*	M	$\alpha f''(0) - \frac{\alpha\beta}{3}(f''(0))^3$
1.0				-0.8947
1.4				-1.1352
1.7				-1.3521
2.0				-1.6201
1.5	0.1			-1.1498
	0.4			-1.1165
	0.6			-1.0804
	0.8			-1.0447
	0.2	0.1		-1.1409
		0.5		-0.9969
		0.9		-0.6886
		1.5		-0.4598
		0.1	0.1	-1.1409
			0.4	-1.2084
			0.7	-1.3060
			1.0	-1.4359

Table 6.3: Effects of thermal parameters $Nb, Nt, \Pr$ and Bi on wall heat flux i.e., $-\theta'(0)$.

Nb	Nt	$\Pr$	Bi	$-\theta'(0)$
0.1	0.1	3.0	0.5	0.4834
0.2				0.3440
0.3				0.2145
0.4				0.1443
0.1	0.1			0.4834
	0.2			0.4120
	0.3			0.3392
	0.4			0.2671
	0.1	1.0		0.2671
		3.0		0.4834
		5.0		0.6737
		10.0		0.9061
		3.0	0.1	0.5231
			0.4	0.4630
			0.8	0.2937
			1.0	0.0917

Table 6.4: Numerical variations in wall mass flux against variations in thermo-physical parameters $Nb, Nt, \Pr, Le, R$ and n.

Nt	Nb	$\Pr$	Le	R	n	$-\phi'(0)$
0.1	0.1	3.0	1.0	0.1	2.0	0.5231
0.2						0.8920
0.3						1.1357
0.1	0.1					0.5231
	0.2					1.1656
	0.3					1.5782
	0.1	1.0				0.3773
		3.0				0.5231
		5.0				0.7972
		3.0	1.0			0.5231
			2.0			0.9088
			5.0			1.2863
			1.0	0.1		0.5231
				0.2		0.6258
				0.3		0.7810
				0.1	1.0	0.5129
					2.0	0.5231
					3.0	0.5289

Tables 6.2-6.4 reports the alterations in wall friction factor, wall heat flux and wall mass flux against physical parameters namely, $\alpha, \beta, \lambda, M, Bi, \text{Pr}, Le, R, n$ and Nb (in tabular notations). **Table** 6.2 exhibits the wall friction factor by varying involving parameters α, β, and M. In absolute sense, the flow parameters α and M grow the surface friction rapidly while physical parameters β and λ have opposite effects on the wall friction. **Table** 6.3 represents the behaviour of controlling parameters Bi, Pr, Nt and Nb on wall heat flux. The wall temperature gradient increases towards Prandtl number Pr, on the other hand, rest of the involved parameters Bi, Nt and Nb reflects opposite trend. **Table** 6.4 shows influence of physical parameters Pr, Le, R, n, and Nb on wall mass flux. It is observed that the mass flux is increasing function of all controlling parameters Pr, Le, R, n, and Nb.

6.4 Conclusions

The major concern of presented work is to explore the combined effects of higher order chemical reactions and magnetic field on slip flow of Prandtl-Eyring nanofluid flow over stretching sheet with convective and Neild boundary conditions. To have clear insight of physical problem, numerical approach named shooting technique is implemented and the obtained results are illustrated via graphical as well as tabular manners. The key outcomes of present communication are outlined as

- In qualitative sense, an enhancement in the Prandtl-Eyring parameter α tends to accelerate the fluid motion while Prandtl-Eyring parameter β, slip parameter $\lambda*$ and Hartmann number M provide resistance to fluid motion. As a result, the Prandtl-Eyring fluid velocity declines.

- Fluid temperature rises for Brownian motion parameter Nb and thermophoresis parameter Nt while Biot number Bi and Prandtl number Pr are responsible for the drop the temperature.

- Thermophoresis parameter Nt and chemical reaction order index n increase the concentration of nanoparticles while concentration profile reduces for the higher values of Brownian motion parameter Nb, Prandtl number Pr, chemical reaction parameter R and Lewis number Le.

- Magnitude of wall friction factor incites for the Hartmann number M and Prandtl-

Eyring parameter α. On the other hand the surface friction decreasing towards both the Prandtl-Eyring parameter β and slip parameter λ^*.

- Heat flux at boundary is inversely proportional to Brownian motion parameter Nb, ,thermophoresis parameter $Nt,$ Biot number Bi and Prandtl number Pr.

Thesis General Concluding Remarks

The prime findings of present thesis are itemized as follows,

- The fluid velocity subject to Sisko, Prandtl and Prandtl Eyring models are found increasing function of curvature.

- The fluid velocity subject to Sisko, Prandtl and Prandtl Eyring models are found decreasing function of magnetic field parameter.

- The fluid temperature subject to Sisko, Prandtl and Prandtl Eyring models reflects decline values towards Prandtl number.

- The fluid concentration subject to Sisko, Prandtl and Prandtl Eyring shows an inverse variation towards Lewise number.

- The surface quantities which include Nusselt number and Skin friction coefficient are enriched for cylindrical surface as compared to flat surface.

- Mass flux at boundary escalates for increasing values of the thermophoresis parameter Nt, chemical reaction order index n, Brownian motion parameter Nb, Prandtl number Pr, chemical reaction parameter R and Lewis number Le.

Biliography

[1] A.W. Sisko, The flow of lubricating greases, Industrial & Engineering Chemistry, 50(1958)1789-1792.

[2] S. Nadeem and N.S. Akbar, Peristaltic flow of Sisko fluid in a uniform inclined tube, Acta Mechanica Sinica, 26(2010)675-683.

[3] S. Nadeem, N.S. Akber and K. Vajravelu, Peristaltic flow of a Sisko fluid in an endoscope, Analytical and Numerical solutions, International Journal of Computer Mathematics, 88(2011)1013-1023.

[4] N.S. Akber, Peristaltic Sisko nano fluid in an asymmetric channel, Applied Nanoscience, 4(2014)663-673.

[5] M. Khan, Q. Abbas and K. Duru, Magnetohydrodynamic flow of a Sisko fluid in annular pipe: A numerical study, International Journal for Numerical Methods in Fluids, 62(2010)1169-1180.

[6] R. Malik, M. Khan, A. Munir and W.A. Khan, Flow and heat transfer in Sisko fluid with convective boundary condition, Plos One, 9(2014) e0107989.

[7] M.Y. Malik, Arif Hussain, T. Salahuddin and M. Awais, Numerical Solution of MHD Sisko fluid over a stretching cylinder and heat transfer analysis, International Journal of Numerical Methods for Heat & Fluid Flow, 26(2016)1787-1801.

[8] N. Moallemi, I. Shafieenejad and A. Novinzadeh, Exact solutions for flow of a Sisko fluid in pipe, Iranian Mathematical Society, 37(2011)49-60.

[9] A. Munir, A. Shahzad, and M. Khan, Mixed convection heat transfer in Sisko fluid with viscous dissipation: Effects of assisting and opposing buoyancy, Chemical Engineering Research and Design, 97(2015)120-127.

[10] A.M. Siddiqui, A.R. Ansari, A. Ahmad and N. Ahmad, On Taylor's scraping problem and flow of a Sisko fluid, Mathematical Modelling and Analysis, 14(2009)515-529.

[11] R.M. Darji and M.G. Timol, Similarity analysis for unsteady natural convective boundary layer flow of Sisko fluid, International Journal of Advances in Applied Mathematics and Mechanics, 1(2014)22-36.

[12] M.W. Dunn, Non-Newtonian fluid flow through fabrics, National Textile Centre Annual Report: November (1999) M98–P02.

[13] S. Nadeem, H. Sadaf and N.S. Akbar, Analysis of peristaltic flow of Prandtl fluid model in an endoscope, Journal of Power Technologies, 94(2014)1-11.

[14] N.S. Akbar, Blood flow analysis of Prandtl fluid model in tapered stenosed arteries, Ain Shams Engineering Journal, 5(2014)1267-1275.

[15] S. Jothi, A.R. Parasad and M.V.S. Reddy, Perestaltic flow of Prandtl fluid in a symmetric channel under the effect of magnetic field, Advances in Applied Science Research, 3(2012)2108-2119.

[16] S.U.S. Choi, Enhancing thermal conductivity of fluids with nanoparticles, The Proceedings of the 1995, ASME International Mechanical Engineering Congress and Exposition, San Francisco, USA, ASME, FED 231/MD 66(1995)99-105.

[17] S.U.S. Choi, Z.G. Zhang, W. Yu, F.E. Lockwood and E.A. Grulke, Anomalously thermal conductivity enhancement in nanotube suspensions, Applied Physics Letters, 79(2001)2252-2254.

[18] H.U. Kang, S.H. Kim and J.M. Oh, Estimation of thermal conductivity of nanofluid using experimental effective particle volume, Experimental Heat Transfer, 19(2006)181-191.

[19] D.H. Yoo, K.S. Hong and H.S. Yang, Study of thermal conductivity of nanofluids for the application of heat transfer fluids, Thermochimica Acta, 455(2007)66-69.

[20] X.Q. Wang and A.S. Mujumdar, A review on nanofluids-Part I: Theoretical and numerical investigation, Brazilian Journal of Chemical Engineering, 25(2008)613-630.

[21] J. Buongiorno, Convective transport in nanofluids, ASME Journal of Heat Transfer, 128(2006)240-250.

[22] W.A. Khan and I. Pop, Boundary-layer flow of a nanofluid past a stretching sheet, International Journal of Heat and Mass Transfer, 53(2010)2477-2483.

[23] P. Rana and R. Bhargava, Flow and heat transfer of a nanofluid over a nonlinearly stretching sheet: A numerical study, Communications in Nonlinear Science and Numerical Simulation, 17(2012)212-226.

[24] F. Mabood, W.A. Khan and A.I.M. Ismail, MHD boundary layer flow and heat transfer of nanofluids over a nonlinear stretching sheet: A numerical study, Journal of Magnetism and Magnetic Materials, 374(2015)569-576.

[25] M.Y. Malik, Imad Khan, Arif Hussain and T. Salahuddin, Mixed convection flow of MHD Eyring-Powell nanofluid over a stretching sheet: A numerical study, AIP Advances, 5(2015)117118.

[26] Arif Hussain, M.Y. Malik, T. Salahuddin, S. Bilal and M. Awais, Combined effects of viscous dissipation and Joule heating on MHD Sisko nanofluid over a stretching cylinder, Journal of Molecular Liquids, 231(2017)341-352.

[27] H. Alfven, Existence of electromagnetic-hydrodynamic waves, Nature, 150(1942)405-406.

[28] T. Sarpkaya, Flow of non-Newtonian fluids in a magnetic field, AIChE Journal, 7(1961)324-328.

[29] S.J. Liao, On the analytic solution of magnetohydrodynamic flows of non-Newtonian fluids over a stretching sheet, Journal of Fluid Mechanics, 488(2003)189-212.

[30] F. Mabood, W.A. Khan and A.I.M. Ismail, MHD stagnation point flow and heat transfer impinging on stretching sheet with chemical reaction and transpiration, Chemical Engineering Journal, 273(2015)430-437.

[31] M.Y. Malik, T. Salahuddin, Arif Hussain and S. Bilal, MHD flow of tangent hyperbolic fluid over a stretching cylinder: Using Keller box method, Journal of Magnetism and Magnetic Materials, 395(2015)271-276.

[32] N.S. Akbar, A. Ebaid and Z.H. Khan, Numerical analysis of magnetic field effects on

Eyring-Powell fluid flow towards a stretching sheet, Journal of Magnetism and Magnetic Materials, 382(2015)355-358.

[33] S. Nadeem, R. Haq and C. Lee, MHD flow of a Casson fluid over an exponentially shrinking sheet, Scientia Iranica, Transactions B: Mech. Eng, 19(2012)1550-1553.

[34] S. Nadeem, R. Haq, N.S. Akbar and Z.H. Khan, MHD three-dimensional Casson fluid flow past a porous linearly stretching sheet, Alex. Eng. J, 52(2013)577-582.

[35] A.M. Ismail, S. Ganesh and C.K. Kirubhashankar, Unsteady MHD flow between two parallel plates through porous medium with one plate moving uniformly and the other plate at rest with uniform suction, Int. J. Sci. Eng. Tech. Res, 3(2014)6-10.

[36] E.M. Abo-Eldahab and A.M. Salem, MHD flow and heat transfer of non- Newtonian power-law fluid with diffusion and chemical reaction on a moving cylinder, Heat and Mass Transfer, 41(2005)703-708.

[37] R.S.R. Gorla, Mixed convection in an axisymmetric stagnation flow on a vertical cylinder, Acta Mechanica, 99(1993)113-123.

[38] N. Bachok and A. Ishak, Mixed convection boundary layer flow over a permeable vertical cylinder with prescribed surface heat flux, European Journal of Scientific Research, 34(2009)46-54.

[39] Y.Y. Lok, J.H. Merkin and I. Pop, Mixed convection flow near the axisymmetric stagnation point on a stretching or shrinking cylinder, International Journal of Thermal Sciences, 59(2012)186-194.

[40] K.U. Rehman, M.Y. Malik, T. Salahuddin and M. Naseer, Dual stratified mixed convection flow of Eyring-Powell fluid over an inclined stretching cylinder with heat generation/absorption effect, AIP Advances, 6(2016)075112.

[41] I. Ullah, I. Khan and S. Shafie, MHD natural convection flow of Casson nanofluid over nonlinearly stretching sheet through porous medium with chemical reaction and thermal radiation, Nanoscale Research Letters, 11(2016)527.

[42] N.A.M. Zin, I. Khan and S. Shafie, The impact silver nanoparticles on MHD free

convection flow of Jeffrey fluid over an oscillating vertical plate embedded in a porous medium, Journal of Molecular Liquids, 222(2016)138-150.

[43] K.U. Rehman, M.Y. Malik, S. Bilal and M. Bibi, Numerical analysis for MHD thermal and solutal stratified stagnation point flow of Powell-Eyring fluid induced by cylindrical surface with dual convection and heat generation effects, Results in Physics, 7(2017)482-492.

[44] M. Sheikholeslami and A.J. Chamkha, Influence of Lorentz forces on nanofluid forced convection considering Marangoni convection, Journal of Molecular Liquids, 225(2017)750-757.

[45] K.U. Rehman, M.Y. Malik, S. Bilal, M. Bibi and U. Ali, Logarithmic and parabolic curve fitting analysis of dual stratified stagnation point MHD mixed convection flow of Eyring-Powell fluid induced by an inclined cylindrical stretching surface, Results in Physics, 7(2017)544-552.

[46] P.S. Gupta and A.S. Gupta, Heat and mass transfer on a stretching sheet with suction or blowing, Canadian Journal of Chemical Engineering, 55(1977)744-746.

[47] T.C. Chiam, Heat transfer in a fluid with variable thermal conductivity over a linearly stretching sheet, Acta Mechanica, 129(1998)63-72.

[48] M.S. Abel, P.S. Datti and N. Mahesha, Flow and heat transfer in a power-law fluid over a stretching sheet with variable thermal conductivity and non-uniform heat source, International Journal of Heat and Mass Transfer, 52(2009)2902-2913.

[49] N. Ahmad, Z.U. Siddiqui and M.K. Mishra, Boundary layer flow and heat transfer past a stretching plate with variable thermal conductivity, International Journal of Non-Linear Mechanics, 45(2010)306-309.
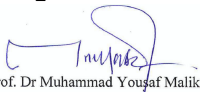
[50] M. Mishra, N. Ahmad and Z.U. Siddiqui, Unsteady Boundary Layer Flow past a Stretching Plate and Heat Transfer with Variable Thermal Conductivity, World Journal of Mechanics,2(2012)35-41.

[51] R.R. Rangi and N. Ahmad, Boundary layer flow past over the stretching cylinder and heat transfer with variable thermal conductivity, Applied Mathematics, 3(2012)205-209.

[52] L. Miao, W.T. Wua, N. Aubry and M. Massoudi, Heat transfer and flow of a slag-type non-linear fluid: Effects of variable thermal conductivity, Applied Mathematics and Computation, 227(2014)77-91.

[53] S. Manjunatha and B.J. Gireesha, Effects of variable viscosity and thermal conductivity on MHD flow and heat transfer of a dusty fluid, Ain Shams Engineering Journal, 7(2016)505-515.

[54] X. Si, X. Zhu, L. Zheng, X. Zhang and P. Lin, Laminar film condensation of pseudo-plastic non-Newtonian fluid with variable thermal conductivity on an isothermal vertical plate, International Journal of Heat and Mass Transfer, 92(2016)979-986.

[55] M.Y. Malik, Arif Hussain, T. Salahuddin, M. Awais, and S. Bilal, Magnetohydrodynamic flow of Sisko fluid over a stretching cylinder with variable thermal conductivity: A numerical study, AIP Advances, 6(2016)025316.

[56] A.J. Chamka, MHD flow of a uniformly stretched vertical permeable surface in the presence of heat generation/absorption and a chemical reaction, International Communications in Heat and Mass Transfer, 30(2003)413-422.

[57] A. Raptis and C. Perdikis, Viscous flow over a non-linearly stretching sheet in the presence of a chemical reaction and magnetic field, International Journal of Non-Linear Mechanics, 41(2006)527-529.

[58] K. Bhattacharyya and G.C. Layek, Chemically reactive solute distribution in MHD boundary layer flow over a permeable stretching sheet with suction or blowing, Chemical Engineering Communications, 197(2010)1527-1540.

[59] F. Mabood, W.A. Khan and A.I.Md. Ismail, MHD stagnation point flow and heat transfer impinging on stretching sheet with chemical reaction and transpiration, Chemical Engineering Journal, 273(2015)430-437.

[60] P.V. Sataya Narayana and D. Harish Babu, Numerical study of MHD heat and mass transfer of a Jeffrey fluid over a stretching sheet with chemical reaction and thermal radiation, Journal of the Taiwan Institute of Chemical Engineers, 59(2016)18-25.

[61] Z. Abbas, M. Sheikh and S.S. Motsa, Numerical solution of binary chemical reaction on stagnation point flow of Casson fluid over a stretching/shrinking sheet with thermal radiation, Energy, 95(2016)12-20.

[62] C. Zhang, L. Zheng, X. Zhang and G. Chen, MHD flow and Radiation heat transfer of nanofluids in porous media with variable surface heat flux and chemical reaction, Applied Mathematical Modelling, 39(2015)165-181.

[63] K.U. Rehman, A.A. Khan, M.Y. Malik, U. Ali and M. Naseer, Numerical analysis subject to double stratification and chemically reactive species on Williamson dual convection fluid flow yield by an inclined stretching cylindrical surface, Chinese Journal of Physics, 55(2017)1637-1652.

[64] A. Afifi, MHD free convective flow and mass transfer over a stretching sheet with chemical reaction, Heat and Mass Transfer, 40(2004)495-500.

[65] A.A. Joneidi, G. Domairry and M. Babaelahi, Analytical treatment of MHD free convective flow and mass transfer over a stretching sheet with chemical reaction, Journal of the Taiwan Institute of Chemical Engineers, 41(2010)35-43.

[66] M.M. Rahman and M. Al-Lawatia, Effects of higher order chemical reaction on micropolar fluid flow on a power law permeable stretched sheet with variable concentration in a porous medium, Canadian Journal of Chemical Engineering, 88(2010)23-32.

[67] M. Ferdows and Q.M. Al-Mdallal, Effects of order of chemical reaction on a boundary layer flow with heat and mass transfer over a linearly stretching sheet, American Journal of Fluid Dynamics, 2(2012)89-94.

[68] S. Palani, B. Rushi Kumar and P.K. Kameswaran, Unsteady MHD flow of an UCM fluid over a stretching surface with higher order chemical reaction, Ain Shams Engineering Journal, 7(2016)399-408.

[69] M.Y. Malik and K.U. Rehman, Effects of second order chemical reaction on MHD free convection dissipative fluid flow past an inclined porous surface by way of heat generation: A Lie group analysis, Information Sciences Letters, 5(2016)35-45.

sources:

1   1% match (student papers from 10-Jul-2015)
    Submitted to National Tsing Hua University on 2015-07-10

2   1% match (publications)
    "Numerical Heat Transfer and Fluid Flow", Springer Science and Business Media LLC, 2019

3   1% match (publications)
    Kolli Vijaya, Gurrampati Venkata Ramana Reddy, Oluwole Daniel Makinde, "Soret Effect on MHD Casson Fluid Flow Past a Moving Vertical Plate in the Presence of Radiation and Chemical Reaction", Diffusion Foundations, 2020

4   1% match (Internet from 06-Jun-2021)
    https://www.hindawi.com/journals/mpe/2021/5162423/tab2/

5   < 1% match (student papers from 14-May-2018)
    Submitted to Higher Education Commission Pakistan on 2018-05-14

6   < 1% match (student papers from 10-Jan-2019)
    Submitted to Higher Education Commission Pakistan on 2019-01-10

7   < 1% match (student papers from 02-Jan-2017)
    Submitted to Higher Education Commission Pakistan on 2017-01-02

8   < 1% match (student papers from 20-Sep-2017)
    Submitted to Higher Education Commission Pakistan on 2017-09-20

9   < 1% match (student papers from 15-Jun-2013)
    Submitted to Higher Education Commission Pakistan on 2013-06-15